Levitated optomechanics with periodically driven fields

Erika B. Aranas

University College London

A dissertation submitted for the degree of

Doctor of Philosophy

August 2018

Declaration

I, Erika B. Aranas, confirm that the work presented in this thesis is my own. Where information has been derived from other sources, I confirm that this has been indicated in the thesis. The work contains nothing which is the outcome of work done in collaboration except where specifically indicated in the text.

Parts of this dissertation have been published, or submitted for publication, as follows.

1. **Chapter 4**: "Nonlinear Dynamics and Strong Cavity Cooling of Levitated Nanoparticles"
   P. Z. G. Fonseca, E. B. Aranas, J. Millen, T. S. Monteiro, and P. F. Barker,
   Phys. Rev. Lett. **117**, 173602 (2016).

2. **Chapter 5**: "Split-sideband spectroscopy in slowly modulated optomechanics"
   E. B. Aranas, P. Z. G. Fonseca, P. F. Barker, and T. S. Monteiro,
   New J. Phys. **18**, 113021 (2016).

3. **Chapter 5**: "Thermometry of levitated nanoparticles in a hybrid electro-optical trap"
   E. B. Aranas, P. Z. G. Fonseca, P. F. Barker, and T. S. Monteiro,
   J. Opt. **19**, 034003 (2017).

4. **Chapter 6**: "Quantum noise spectrum in periodically modulated optomechanics"
   E. B. Aranas, M. Javed Akram, Daniel Malz, and T. S. Monteiro,
   Phys. Rev. A **96**, 063836 (2017).

5. **Chapter 6**: "Stochastic Langevin propagation for classical and quantum optomechanics"
   M. J. Akram, E. B. Aranas, N. P. Bullier, J. E. Lang, and T. S. Monteiro,
   arXiv preprint: arXiv:1801.08700 [quant-ph].

Erika B. Aranas

August 2018

Abstract

Levitated optomechanics offers a route to high-Q, low frequency oscillators by all-optical trapping in high vacuum, although progress has been hampered by particle loss at ~ 1 mbar. Combining an optical cavity with a Paul trap yielded promising results, showing stable trapping and strong cavity cooling of 200 nm silica nanoparticles up to $\sim 10^{-5}-10^{-6}$ mbar, in addition to interesting nonlinear effects. However, the time-periodic fields of the Paul trap gave rise to atypical "split-sideband" spectra which we found to be correlated with the cooling dynamics of the nanoparticle: twin peaks around the mechanical frequency plus a dominant signal at the second harmonic indicated weak cooling, while a complete suppression of one of the split-sidebands showed strong cooling. Presented first in this thesis are the analytical and numerical models used to describe the dynamics of a nanoparticle in a hybrid electro-optical trap. The split-sideband spectra is a result of simultaneous, out-of-phase oscillations in g and ω_{M}, and is, in fact, a generic feature of any optically trapped particle where an auxiliary field causes a harmonic excursion in the equilibrium position. Split-sideband asymmetry and thermometry are further discussed for a generic, doubly-modulated optomechanical system. A suitably normalised cavity output probing a split-displacement spectra still gives the correct steady-state temperature. Analytical formulas are also derived for the complete split-sideband suppression, which may offer additional diagnostic of the quantum regime. Finally, a matrix algorithm to accurately calculate the measured quantum spectra of linear optomechanical systems with arbitrary periodicity is devised to verify the results obtained thus far. In addition, the algorithm allows a systematic calculation of the non-stationary components of the spectra, which are usually averaged out, but are shown to be experimentally accessible via heterodyne detection. In summary, this thesis aims to contribute to the analysis of levitated optomechanics with periodically driven fields, motivated in part by modelling the hybrid electro-optical experiments in UCL.

Impact Statement

Sensors are all around us as they are an essential component of many modern technological devices: not only incorporated in our smartphones, gyroscopes and accelerometers are also used for inertial navigation systems in transportation and defense; acoustic sensors detect ground vibrations for earthquakes or volcanic activity; and, recently, optomechanical force sensors allowed the observation of immense astronomical events through gravitational waves that they produced.

All these sensors, regardless of their applications and internal mechanisms, are limited by noise, mostly thermal in origin. For most commercial and industrial applications, small thermal noises do not pose a problem; however, for gravitational wave astronomy and other tests of fundamental physics, ultra-high sensitivities are required so thermal noises must be eliminated. In this regime, one begins to consider a more fundamental type of noise, called "quantum noise", which are intrinsic to any physical system.

The analytical and numerical models presented in this thesis have been integral to the hybrid trap experiment in UCL, which is part of a larger effort to realise ultra-sensitive optomechanical sensors by levitation in high vacuum. Optomechanical sensors are actually now being used for military applications as well as for seismic detection, although one of the more ambitious goals for developing levitated optomechanical sensors is for fundamental tests of quantum physics. By connecting the internal dynamics with the detected signal, this work was able to provide a full analysis of the levitated nanosphere in a hybrid trap experiment.

Meanwhile, the field of optomechanics still continuous to grow, driven mainly by the experimental progress made in pushing quantum mechanics to higher mass regimes. Nonetheless, despite the multitude of optomechanical set-ups, many experiments still employ linear, continuous measurements to obtain quantum noise spectra. At the same time, modulations within optomechanical systems (like the hybrid trap), as well as during detection may prove to be useful to future optomechanical experiments. By providing a means to accurately calculate the quantum noise spectra for periodically driven optomechanical systems, this work hopes to contribute to the field optomechanics in general.

Acknowledgements

Studying in UCL is one of the biggest privileges of my life. My heartfelt gratitude goes to my supervisor, Prof. Tania Monteiro, for doing so much more than what I could have expected from a PhD supervisor. I thank her for her mentorship, patience, and assistance in many aspects of my PhD. I am also grateful to Schlumberger Foundation for generously funding my studies in the UK, and to my previous supervisor Dr. Raphael Guerrero for his unwavering support throughout my scholarship applications.

I would like to thank the rest of the optomechanics group, Prof. Peter Barker, Giacomo Fonseca, Nathanaël Bullier, Antonio Pontin, Lia Ying, and all the rest for the insightful discussions over coffee. I acknowledge my co-authors Daniel Malz and Javed Akram for their useful feedback during the writing of our manuscript. To all the professors and students I have met in my conferences in Göteborg, Barcelona, Gdańsk, thank you so much for indulging me and my endless questions.

Many thanks to my friends and colleagues in UCL — Luciana Henaut, Naïri Usher, Michela Venturelli, Andrea Loreti, Thomas Meltzer, Jacob Lang, Seto Balian, Duncan Little, Abol Bayat, and many others — for sharing with me their knowledge and time. I am lucky to be surrounded with such smart and interesting people.

To my friends from Lillian Penson: Crystal, Benji, Daniel, Soody, Joseph, among many others, for making my stay in London so much more colorful. My special gracias to David Mariscal for his desk and good vibes which have been crucial throughout the making of this manuscript.

Finally, my warmest gratitude to my siblings: Leika, Nikko, Kyle, and Gaiea, for being my life's bundle of joy. It is a pleasure to see you all grow and mature. I am so blessed.

I dedicate my work to my mother, Digna, who first dreamed big for me.

Contents

List of Figures

5.2 **(a)** For a generic system where both $g(t) = 2\bar{g}\sin\omega_{\rm d}t$ and $\omega_{\rm M}(t) = \overline{\omega}_{\rm M} + 2\omega_2\cos 2\omega_{\rm d}t$ are modulated, the figure illustrates schematically how the spectrum of the cavity field ($S_{yy}(\omega)$), arises from the spectrum of the mechanical motion. Top panel illustrates the $\hat{\rm x}(\omega)$ spectrum: the effect of $\omega_2 > 0$ is to produce additional $\pm 2\omega_{\rm d}$ side-peaks. Middle panel: unlike the typical optomechanical case, the cavity field now follows $\hat{\rm x}(\omega+\omega_{\rm d}) - \hat{\rm x}(\omega-\omega_{\rm d})$ rather than $\hat{\rm x}(\omega)$. The interference of the individual $\hat{\rm x}(\omega\pm\omega_{\rm d})$ components (shown in brown/green) yields constructive enhancement near $\omega \simeq \pm(\omega_{\rm M}-\omega_{\rm d})$, and destructive cancellation near $\omega \simeq \pm(\omega_{\rm M}+\omega_{\rm d})$. Instead of the "twin peak" structure seen in Fig. 5.1 for $\omega_2 = 0$, the resultant cavity output sidebands display a pair of peaks of asymmetric heights (lower panel). For small $\overline{g}$, the ratio between peaks $r \simeq (\omega_2 - 2\omega_{\rm d})^2/(\omega_2+2\omega_{\rm d})^2$ so the $\omega_{\rm M}+\omega_{\rm d}$ peak is strongly suppressed for $\omega_2 \sim 2\omega_{\rm d}$ ($r \approx 0$). This asymmetry is distinct from the usual Stokes/antiStokes sideband asymmetry at $\pm\omega \simeq \omega_{\rm M}$, which is still present. Lower panel shows the Stokes peaks (red). **(b)** In thermal regimes, the ratio r is insensitive to $\Gamma_{\rm M}$; however, as $\Gamma_{\rm M} \to 0$ and the backaction limit is attained, correlations between back-action and incoming noise alters the relative heights of the peaks, mainly since ponderomotive squeezing lowers the height of the $\omega_{\rm M}+\omega_{\rm d}$ peak relative to the imprecision floor. For incoming quantum shot noise, significant changes in r arise only if the oscillator is near the ground state. Inset reproduces part of Fig. 5 of [10] illustrating previously overlooked asymmetries in experimental sidebands which supports our modulated-optomechanics model. Figures and caption adapted from [12]. 83

List of Tables

List of Acronyms

BAE	Backaction evasion
CHO	Classical harmonic oscillator
CSL	Continuous spontaneous localisation
DMPA	Detuned mechanical parametric amplification
IOM	Independent oscillator model
PDH	Pound-Drever Hall
PSD	Power spectral density
QHO	Quantum harmonic oscillator
RWA	Rotating wave approximation
SQL	Standard quantum limit
ZPF	Zero-point fluctuation

1 Introduction

1.1 Cavity optomechanics: measurement and control of mechanical motion

The past couple of years have witnessed two of the most revolutionary experimental observations in physics: the detection of gravitational waves due to black hole [15] and neutron star mergers [16]. Each of the orthogonal arms of the Advanced Laser Interferometric Gravitational Wave Observatory (LIGO) detectors are equipped with 40-kg mirrors, which form optical cavities. A ripple in spacetime causes differential mechanical displacements, which are encoded in the optical phase difference measured via homodyne detection.

With 100 kW of circulating power, the optical cavities of LIGO offer an extremely sensitive readout of mechanical motion up to the order of 10^{-18} m — $10^3 - 10^4$ times less than the radius of a proton [17]. Measurements on such small scales pose not only engineering challenges but also approach fundamental quantum constraints on detection sensitivity. For a mirror oscillator of mass $m = 10$ kg and mechanical frequency $\omega_{\mathrm{M}} = 2\pi \times 100$ Hz, intrinsic quantum fluctuations $x_{\mathrm{zpf}} = \sqrt{\hbar/(2m\omega_{\mathrm{M}})} \sim 10^{-19}$ m are just an order of magnitude smaller than the signal of interest. To follow mechanical motion, one must at least consider sequential position measurements, separated by the time interval Δt, of a free mass. Such measurements will have an uncertainty $\propto x_{\mathrm{zpf}}^2 \Delta t$ [3]. Obviously, a strong, projective measurement of only one position, for which $\Delta t = 0$, is not subject to any limit. On the other hand, the precision of a sequential measurement is degraded by x_{zpf}^2. Further adding optical contributions, quantum noises therefore become a real consideration in gravitational wave detection.

Indeed, the quest for gravitational waves provided an impetus for the field of optomechanics, which is the study of the coherent interaction of light and mechanical objects. Each arm of a LIGO detector forms a canonical optomechanical system: an optical cavity (frequency ω_{c}) with a mechanically compliant end mirror (frequency ω_{M}) (see Fig.1.1a). Theoretical studies of optomechanical interaction in the 1960's already anticipated the effects of quantum noises on force and displacement sensing in the context of interferometric detect-

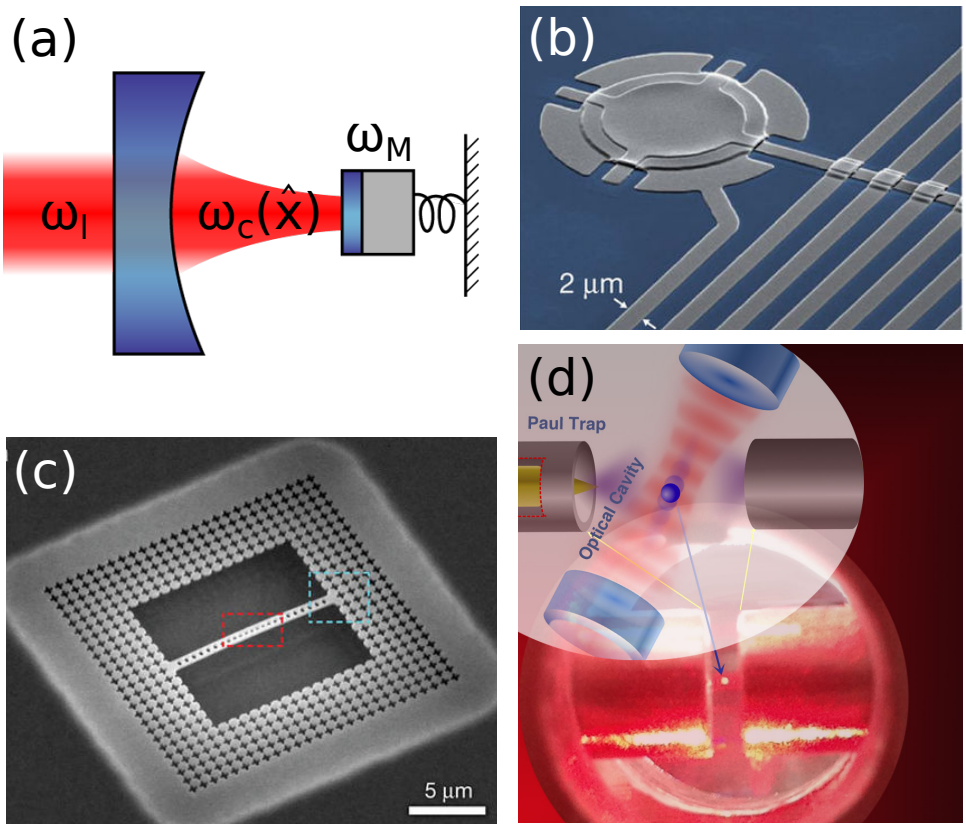

Figure 1.1: Different experimental implementations of cavity optomechanics, which uses the dynamical effect of radiation pressure force for measurement and control of mechanical objects. **(a)** Canonical system consisting of a laser-driven optical cavity with a mechanically compliant mirror. Mechanical oscillations at $\omega_{\rm M}$ change the position $\hat{x}$ and hence the cavity length, resulting in a dispersive interaction $\omega_{\rm c}(\hat{x})$. **(b)** An Al membrane capacitively coupled to a superconducting microwave circuit [1]. **(c)** A patterned Si nanobeam supporting co-localised photonic and phononic modes [2]. **(d)** Levitated silica nanoparticle in a hybrid electro-optical trap comprised of an optical cavity and a Paul trap. Although ground state has been achived for **(b)** and **(c)**, levitated optomechanics offer the route to high-Q mechanical oscillators suitable for fundamental physics experiments and force sensing applications. One of the main bottlenecks, which is particle loss at high vacuum, has been partly overcome by using a Paul trap — a step closer to ground state cooling in kHz oscillators.

ors [18]. Nowadays, advances in micro- and nano- fabrication have led to microcavities, photonic nanobeams, microtoroid resonators, as well as many different optomechanical platforms spanning a broad range of masses and frequencies [19]. Regardless, the canonical optomechanical Hamiltonian still holds: $\hat{H} = \omega_{\rm c}(\hat{x})\hat{a}^\dagger\hat{a} + \omega_{\rm M}\hat{b}^\dagger\hat{b}$, where $\hat{a}, \hat{a}^\dagger$ $(\hat{b}, \hat{b}^\dagger)$ are the ladder operators for the photonic (phononic) mode.

The position-dependent cavity frequency, also called dispersive interaction, $\omega_{\rm c}(\hat{x})$ can be explained by the mechanical effects of radiation pressure: a photon (wavelength λ) at normal incidence to an object will impart a momentum of $2\hbar/\lambda$. The resulting mechanical displacement $\hat{x}$ will cause, to first order, a linear change in ω_c proportional to the optomechanical coupling $g_0 \equiv x_{\rm zpf}\, \partial\omega_{\rm c}/\partial\hat{x}$. Single photon couplings are typically weak so using a high-Q (low loss) cavity is crucial to multiply this effect. With a stronger intracavity power, the light field can then be expressed as a sum of a classical mean value

plus small quantum fluctuations: $\hat{a} \rightarrow \bar{\alpha} + \hat{a}$. Recent efforts are being directed at improving g_0 [20, 21], but most optomechanical experiments to date have been described by the linearised Hamiltonian:

$$\hat{H} = -\hbar\Delta\hat{a}^\dagger\hat{a} + \hbar\omega_{\mathrm{M}}\hat{b}^\dagger\hat{b} - \hbar g(\hat{a} + \hat{a}^\dagger)\hat{x}/x_{\mathrm{zpf}} \tag{1.1}$$

where $g = \bar{\alpha}g_0$ is the light-enhanced optomechanical coupling, and $\Delta = \omega_{\mathrm{l}} - \omega_{\mathrm{c}}$ is the cavity detuning.

For $\Delta = 0$, the cavity phase provides the most sensitive readout (i.e., amplification) of mechanical motion, albeit inevitably with additional noises [22]. Apart from intrinsic mechanical fluctuations, the quantum nature of the cavity probe (i.e., discreteness of photons) leads to an imprecision noise that scales as $1/\bar{n}$, where $\bar{n}$ is the mean number of intracavity photons. Experimentally, this sets the shot noise level of the measurement, which can be easily overcome by measuring with a low noise, high power laser drive to improve the signal-to-noise ratio. However, increasing with $\bar{n}$ is the mechanical disturbance due to backaction noises; such backaction heating was observed for the first time in a macroscopic SiN membrane inside a Fabry-Pérot cavity [23]. A balance between the two competing imprecision and backation noises can be achieved with the optimum optical power, setting the so-called standard quantum limit (SQL) for continuous position measurements. A force sensitivity of 4x above the SQL has been achieved using an ultracold atomic cloud in an optical cavity [24], although typically, most macroscopic sensors operate far from SQL because of high phonon occupation: $\bar{n}_{\mathrm{th}} = kT/\hbar\omega_{\mathrm{M}}$. For a GHz oscillator, $\bar{n}_{\mathrm{th}} < 1$ implies a mK thermal bath attainable by simple cryogenic refrigeration [25]. However, for lower ω_{M}, conditions for ground state cooling become more stringent.

Fortunately, the cavity field provides not only a built-in readout but also quantum control of mechanical motion. With $\Delta = -\omega_{\mathrm{M}}$, optomechanical cooling of macroscopic center-of-mass motion is possible in the sideband-resolved regime [26, 27]: high-Q cavities for which the cavity losses $\kappa \ll \omega_{\mathrm{M}}$ create a retarded backaction that damps mechanical motion. As a result, mean phonon occupations < 1 have been experimentally observed in an Al membrane capacitively coupled to a superconducting LC microwave circuit [1] (Fig. 1.1b), as well as in optically coupled photonic and phononic modes in patterned Si nanobeams [2] (Fig. 1.1c), where observation of sideband asymmetry in the noise spectra provide further evidence of the quantum regime [28, 29].

Experimental breakthroughs in optomechanical ground-state cooling have made possible highly coherent macroscopic mechanical oscillators. Landmark experiments that defined quantum optics following the invention of lasers are now being applied to the realm

of mechanical objects, thus paving the way towards quantum acoustics. Single-phonon control has already been achieved in MHz oscillators: using patterned SiN nanobeams, Hong, et. al. has demonstrated phonon antibunching in single phonon Fock state interference [30], in complete analogy with the Hanbury Brown and Twiss experiment of quantum optics. Squeezed states, which had long been sought after in the quantum optics community, have now been observed in mechanical resonators [31, 32, 33] via reservoir engineering [34]. Using the same technique, steady-state entanglement of two spatially separated MHz micromechanical drum oscillators [35] has also been created.

Arguably, quantum optics in the 1960s meant probing the quantum coherent nature of the optical field only.[1] Today, the measurement and control of mechanical motion afforded by optical cavities have led to experiments showcasing coherent interaction between light and mechanics, such as optomechanically induced transparency [36], ponderomotive squeezing of light [37, 38, 39], and optomechanical entanglement [40] — many of which have analogues in cavity quantum electrodynamics experiments — although in this case, with much bigger mechanical elements.

1.2 Levitated optomechanics: Pushing the boundaries of quantum theory

Indeed, cavity optomechanics has taken quantum theory to unprecedented mass and frequency scales, promising much needed experimental progress on foundational issues in quantum physics. For example, quantum mechanics postulates that the dynamics of a quantum system is governed by the Schrödinger equation until measurement instantaneously collapses the superposition state randomly to any one of the eigenstates of the measurement operator. The incompatibility between the linear, deterministic evolution of the wavefunction and the nonlinear, probabilistic nature of quantum measurements has been in part due to our inability to actually observe the collapse mechanism.

Related to this shortcoming is the difficulty of creating massive objects in superposition, leading to the apparent, but unnecessary boundary separating the quantum from the classical. While environmental decoherence [41] may justify the fragility of macroscopic superposition states, collapse models, such as the well-studied continuous spontaneous localization (CSL) theory, offer a more direct explanation of the collapse mechanism. CSL incorporates a phenomenological nonlinear term in the Schrödinger equation [42] — parameterised by a certain characteristic coherence length r_c and mass-proportional collapse rate λ of a superposition state — in a way that is consistent with standard quantum the-

[1] As remarked by Prof. Fritz Haake in the Quantum Optics IX conference in Gdánsk, Poland

ory but also models the rapid suppression of coherence in macroscopic objects. Indeed, a lot of questions on the nature of quantum gravity and quantum measurement still remain unanswered because of experimentally challenging regimes required for such fundamental tests. Clamped set-ups (Fig. 1.1) pose a hindrance to attaining the necessary high-mass, low-frequency regime, as the quality factor $Q_{\mathrm{M}} \equiv \omega_{\mathrm{M}}/\Gamma_{\mathrm{M}}$ is limited by the intrinsic mechanical damping rate Γ_{M}.

To avoid environmental decoherence due to mechanical supports, simultaneaous proposals for levitated optomechanical systems were then made [43, 44, 45]. Ultra-high $Q_{\mathrm{M}} \sim 10^{12}$ can be theoretically attained by pumping the pressure down to $10^{-7}-10^{-8}$ mbar. Actually, optical gradient traps have been around since the 1970's when Ashkin first demonstrated levitation of a dielectric particle in high vacuum ($\approx 10^{-6}$ mbar) [46]. However, only with the advent of low-loss microcavities have such particles been cooled to the ground state via resolved-sideband cooling [26, 27].

For the purpose of testing CSL and other collapse models, a protocol for preparing macroscopic superposition states using a nanosphere levitated in an optical cavity has been proposed in [47]. The continuous x^2 measurement afforded by the quadratic potential of the optical cavity acts like a double-slit that creates a conditional superposition state [48]. The quadratic coupling strength, as well as the mass, frequency, and Q_{M} of the mechanical oscillator determine the attributes of the superposition state. To ensure fringe visibility and a coherent superposition (as opposed to a statistical mixture), low-ω_{M} and high-Q_{M} are necessary.

The same conditions are crucial for non-interferometric tests of CSL, where the temperature of the mechanical oscillator is monitored via the integral of the noise spectrum, as is commonly done in optomechanical experiments. An experimental signature of the CSL force is a temperature-independent violation of the equipartition theorem: $\Delta T_{\mathrm{CSL}} = \hbar^2 \eta Q_{\mathrm{M}}/(2k_{\mathrm{B}} m \omega_{\mathrm{M}})$ [49]. Since ΔT_{CSL} has to compete with other sources of decoherence, a high Q_{M} and low ω_{M} are crucial to increase ΔT_{CSL}. Similarly, levitated nanospheres are ideal set-ups for general force sensing applications because the minimum detectable force $F_{\mathrm{min}} \propto \sqrt{Q.f}$. Experiments on detecting short-range non-Newtonian forces [50], Casimir forces and high-frequency gravitational waves are a few possible applications [51].

Figure 1.2 shows the different groups working on levitated setups. They satisfy the high Q_{M}, low-ω_{M} regime for applications described above, and are expected to surpass current records in $Q.f$ factors as soon as the ground state is reached. Initial advances were made in active feedback cooling of levitated, dielectric nanoparticles although all of them attained only mK temperatures. In [52], a 10 kHz SiO_2 nanoparticle oscillator in a dual

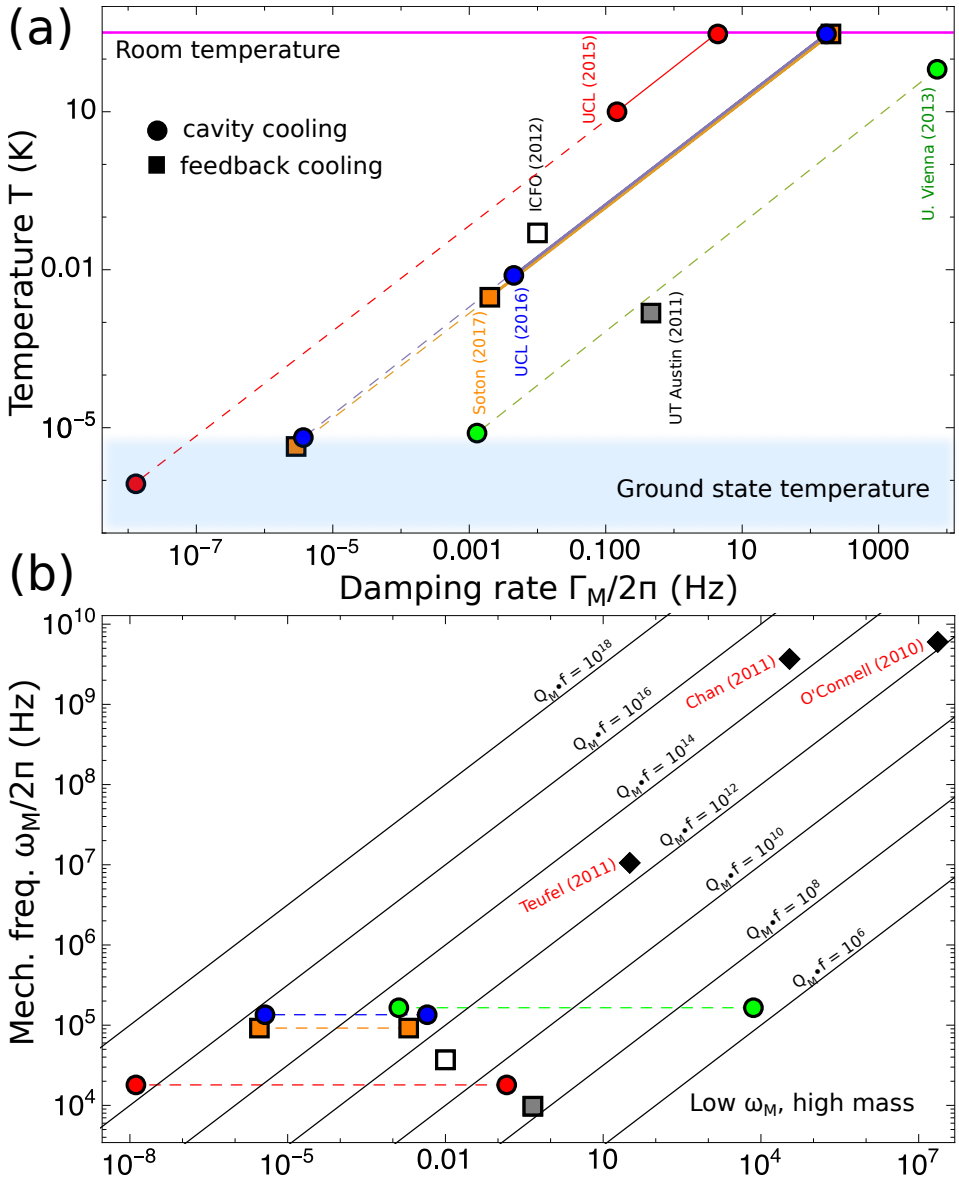

Figure 1.2: A survey of levitated optomechanical set-ups. (**a**) Temperature vs. damping rate of cavity (circle) and feedback (square) cooling experiments. Solid lines indicate cooling from room temperature (300 K) to the lowest temperature attained. Most of the set-ups achieve cooling by lowering the gas pressure (proportional to $\Gamma_{\rm M}$), keeping the cooling rate constant. The formula $T = 300K\Gamma_{\rm M}/\Gamma_{\rm opt}$ allows calculation of the cooling rate far from the ground state. Mechanical frequencies range from $\omega_{\rm M} \approx 9.7 - 165$ kHz, corresponding to ground state temperatures $T_{\rm ground} < \hbar\omega_{\rm M}/k$ of $\approx 0.47 - 7.9\,\mu$K indicated by the blue region. Dotted lines represent cooling to the ground state as the pressure is lowered, assuming the cooling rate is held constant. A higher cooling rate means $T_{\rm ground}$ is achieved at a much higher pressure, where problems of particle instability could be avoided. Note, however, that radiation pressure noise causes additional heating near the ground state, but are not considered here in the meantime. (**b**) Mechanical frequency vs. damping rate of levitated and clamped systems (solid diamonds) for which ground state has already been achieved. Constant $Q \cdot f = \omega_{\rm M}^2/(2\pi\Gamma_{\rm M})$ factors are shown in diagonal lines. A couple of levitated set-ups have $Q \cdot f$ factors comparable to clamped systems, and will attain even higher $Q \cdot f \simeq 10^{14} - 10^{16}$ upon ground state cooling. The promise of a high $Q \cdot f$, low-$\omega_{\rm M}$ make levitated set-ups a suitable testbed for quantum gravity and quantum measurement experiments, as well as high-precision force sensing.

beam trap was cooled in x, y, z dimensions via active feedback. Residual coupling among three orthogonal laser beams has limited the final temperature to 1.5 mK. A parametric

feedback scheme [53] is employed to reduce the trapping and cooling field into a single laser beam, thereby eliminating potential source of recoil heating and feedback noise due to beam misalignment, although random phase errors cap the final temperature also to mK range. Feedback cooling of a laser-trapped particle to 450 μK has allowed a direct observation of photon recoil heating for the first time in macroscopic objects [54]. Parametric feedback using parabolic mirror trap has also led to mK final temperature [55].

Feedback studies recognise the need for an additional cavity cooling as the final route to the ground state. Experiments with cavity-trapped silica [11] obtained high optical damping rates of $2\pi \times 49$ kHz, which could have led to the ground state at a relatively high pressure $\sim 10^{-7}$ mbar, although it was impeded by particle loss at ~ 1 mbar. Cooling at a high vacuum environment (10^{-8} mbar) was also observed but with freely-propagating silicon nanoparticles [56].

Auxiliary fields — for example, a second cavity mode [57], an optical tweezer, or a Paul trap [58] — had been used to aid trapping at high vacuum for cavity cooling from room temperature. With a cavity finesse of ~ 50000, stable trapping up to 10^{-6} mbar and strong cavity cooling of a charged, silica nanosphere was reported through the use a quadrupole Paul trap. Its time-dependent parabolic potential not only provides a stable potential for indefinite trapping at high vacuum, but is also indispensable for cavity cooling.

Meanwhile, a number of optomechanical set-ups have involved periodically driven fields, motivated in part by the quest to overcome the Standard Quantum Limit (SQL) by measuring a single quadrature of the mechanical oscillator [59]. To date, two different ways to do single-quadrature detection have been proposed: one considered modulations of the optomechanical coupling g to perform back-action evasion (BAE) measurements [59, 60], while the other considered modulation of ω_{M} to perform detuned mechanical parametric amplification (DMPA) [61, 62]. Closely related schemes to generate mechanical squeezing are also of much interest. Modulation of the cavity field at $2\omega_{\mathrm{M}}$ results in amplification of one quadrature and to squeezing of the conjugate quadrature [63, 64]. The above studies all considered modulation either at or close to ω_{M} (resonant or near-resonant); or modulation at a multiple (usually twice) of ω_{M} [63, 65]. In addition, they considered modulation of *either* $g(t)$ [63, 65] or of the spring constant [61, 62]. In such modulated set-ups, the quantum noise spectrum does not conform anymore to closed-form solutions for the standard, unmodulated case; hence, the need for an accurate way of solving the measured power spectral densities.

1.3 Thesis outline

This thesis presents an analysis of levitated optomechanics with periodically driven fields, motivated by, but not limited to, the hybrid electro-optical trap experiment in UCL. In Chapter 2, a review of the standard optomechanical theory is given starting from the quantum harmonic oscillator and its interaction with a thermal bath, followed by its coupling with cavity fields for measurement and control. Analytical formulas for the final mechanical occupation and optomechanical cooling rate are derived. In Chapter 3, an overview of the hybrid electro-optical trap dynamics is presented, by first looking into the gradient forces in the cavity, and then the time-dependent quadrupole potential of the Paul trap. The cooling rate for the modulated system is derived, which depends on the trapping optical well. In Chapter 4, three key experimental results from [10] are reviewed: (1) strong cavity cooling up to 10^{-6} mbar for a high N catch; (2) quadratic coupling for a low N catch; and (3) transient dynamics showing both linear and quadratic cooling. In Chapter 5, two analytical models for the appearance of split-sidebands are given, in the context of a generic doubly modulated optomechanical system. The analysis is applied to perform split sideband thermometry which is crucial to the hybrid trap experiment. Finally, in Chapter 6, a matrix algorithm is devised for accurately calculating the spectrum for optomechanical systems with arbitrary periodicity in the both the coherent and dissipative couplings. The measured quantity is typically the stationary part of the output spectrum, although nonstationary components can also be accessed through proper heterodyning.

2 | Standard Optomechanics

Sidney Coleman, a theoretical physicist, once said: "The career of a young theoretical physicist consists of treating the harmonic oscillator in ever-increasing levels of abstraction." Because cavity optomechanics is formally the study of two coupled quantum harmonic oscillators, the first section of this chapter is devoted to the review of such a ubiquitous model in physics. The dynamics of a mechanical oscillator in a thermal bath is discussed in Sec. 2.2, where the temperature and the linear response under the action of a thermal force are also derived. In Sec. 2.3, the optomechanical Hamiltonian is presented, and the optical cavity is seen as an optical force that changes the effective linear response of the mechanical oscillator. This leads to optomechanical cooling, discussed in Sec. 2.4, as well as phase sensitive detection, discussed in Sec. 2.5, where the standard quantum limit (SQL) to optical measurements of mechanical motion is derived. Finally, a few ideas on sensing beyond SQL is briefly presented in Sec. 2.6.

2.1 Quantum harmonic oscillator

First, let us start with a classical harmonic oscillator (CHO). The state of a CHO at any time t is completely specified by a point $X(t)+\mathrm{i}P(t)$ in (complex) phase space, where $X(t)$ and $P(t)$ are the dimensionless position and momentum quadratures (see Fig. 2.1a). The dynamics can be derived from the classical (dimensionless) Hamiltonian:

$$H = \frac{1}{2}(X^2 + P^2) \tag{2.1}$$

Alternatively, a CHO can be modelled as a rotating phasor $b\mathrm{e}^{\mathrm{i}\omega_\mathrm{M}t}$, where b is the complex amplitude and $\omega_\mathrm{M}t$ is the phase. Following the motion of this state, we see that the position traces out a familiar sine wave with amplitude b, and energy $\propto |b|^2$. The following relationship holds:

$$X = (b + b^*)/\sqrt{2} \tag{2.2}$$

$$P = -\mathrm{i}(b - b^*)/\sqrt{2} \tag{2.3}$$

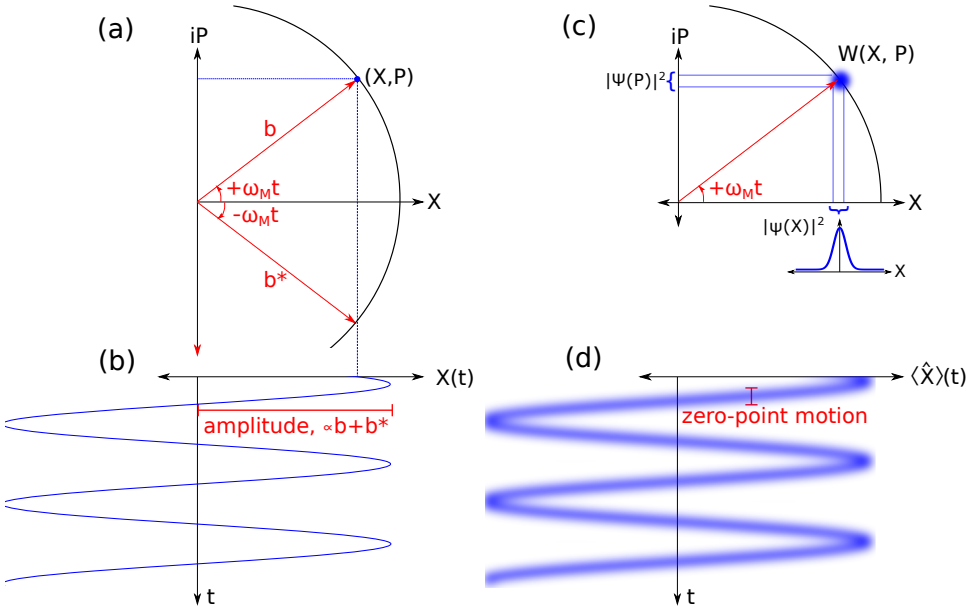

Figure 2.1: **(a)** Classical harmonic oscillator depicted as a point $X+\mathrm{i}P$ in complex phase space, or as a phasor $b = |b|\mathrm{e}^{\mathrm{i}\omega_\mathrm{M} t}$. **(b)** The position $X(t)$ traces out a familiar sine wave with amplitude $b+b^*$. **(c)** The state of a quantum harmonic oscillator is modelled by a Gaussian Wigner function $W(X,P)$ whose marginal $\int_{-\infty}^{+\infty} W(X,P)\mathrm{d}P = |\psi(X)|^2$. The phasor's tip can be anywhere within the fuzzy region. **(d)** The measured position of the QHO may fluctuate around the mean of $|\psi(X)|^2$ with a variance (in real units) given by the zero-point motion $x_\mathrm{zpf} = \sqrt{\hbar/(2m\omega_\mathrm{M})}$.

It is easy to see from Fig. 2.1a that for a given state, the position X uniquely determines P, and vice-versa. The same is not true for a quantum harmonic oscillator (QHO). Instead of a point, the state of a QHO is specified by Wigner function $W(X,P)$, represented by a fuzzy area in Fig. 2.1b. For our purpose, $W(X,P)$ is a Gaussian — meaning, its *representation* in say the X coordinate is given by $\psi(X)$ which is a Gaussian. The position of the QHO is then, in a sense, "everywhere at the same time" — very much like a wave — but different positions are assigned with different probabilities determined by $|\psi(X)|^2$.

It is important to make the distinction between a specific representation (like $\psi(X)$ or $\psi(P)$, which in general can be different expressions) versus the represented entity $|\psi\rangle$, which is a vector in an abstract vector space, because quantum mechanics formalism is expressed through the latter. Quantum theory *postulates* that the position and momentum are not anymore coordinates in phase space, but instead are linear transformations (specifically, Hermitian operators) $\hat{X}$ and $\hat{P}$ acting on the vector $|\psi\rangle$. The quantum analogue of Eq. 2.1 is:

$$\hat{H} = \frac{1}{2}\hbar\omega_\mathrm{M}\left(\hat{X}^2 + \hat{P}^2\right), \tag{2.4}$$

with

$$\begin{aligned}\hat{X} &= \left(\hat{b}+\hat{b}^{\dagger}\right)/\sqrt{2} \\ \hat{P} &= -\mathrm{i}\left(\hat{b}-\hat{b}^{\dagger}\right)/\sqrt{2}.\end{aligned} \tag{2.5}$$

$\hat{X}$ and $\hat{P}$ are commonly referred to as quadratures, while $\hat{b}$ and $\hat{b}^{\dagger}$ are the creation and annihilation operators, which are just the quantisation of the complex phasor amplitudes in Fig. 2.1.

Substituting Eq. 2.5 into Eq. 2.4:

$$\hat{H} = \hbar\omega_{\mathrm{M}}\left(\hat{b}^{\dagger}\hat{b}+\frac{1}{2}\right). \tag{2.6}$$

whose energy eigenstate $|n\rangle$ correspond to states with the energy $E_n = \hbar\omega_{\mathrm{M}}(n+1/2)$.

At the ground state $|0\rangle$ the zero-point energy $\hbar\omega_{\mathrm{M}}/2$ of the QHO is distributed equally to the quadratures, which in real units read:

$$\begin{aligned}\hat{x} &= \sqrt{2}x_{\mathrm{zpf}}\hat{X} \\ \hat{p} &= \sqrt{2}p_{\mathrm{zpf}}\hat{P},\end{aligned} \tag{2.7}$$

where $x_{\mathrm{zpf}}^2 \equiv \langle 0|\hat{x}^2|0\rangle = \hbar/(2m\omega_{\mathrm{M}})$ and $p_{\mathrm{zpf}}^2 \equiv \langle 0|\hat{p}^2|0\rangle = (\hbar m\omega_{\mathrm{M}})/2$ are the zero-point fluctuations of the mechanical oscillator.

Specifically, the position operator $\hat{X}$ has an associated set of continuous eigenvectors $|X_j\rangle$ corresponding to real eigenvalues X_j. The standard, Copenhagen interpretation of a measurement is that $\hat{X}$ projects or "collapses" $|\psi\rangle$ into one of the eigenstates $|X_j\rangle$ corresponding to the position X_j. This result is random but measurements on an ensemble of identical states $|\psi\rangle$ will follow $\psi(X)$.

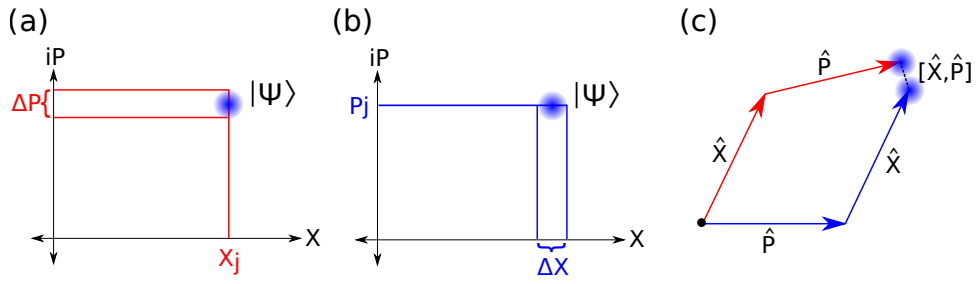

Figure 2.2: Pictorial explanation for the CCR $\left[\hat{X},\hat{P}\right]=1$: **(a)** Applying $\hat{X}$ collapses ψ to a state with position X_j, which corresponds to momentum states with a value within ΔP. **(b)** On the other hand, measuring with $\hat{P}$ first measures some P_j with full certainty, although this corresponds to many position states within ΔX. **(c)** The orders by which $\hat{X}$ and $\hat{P}$ are applied are depicted by red ($\hat{P}\hat{X}$) and blue ($\hat{X}\hat{P}$) arrows. The final states can be anywhere within the fuzzy region, an on average will not overlap by an amount proportional to $\left[\hat{X},\hat{P}\right]$.

Whereas before $xp = px$, linear transformations are not, in general, commutative: $\hat{X}\hat{P} \neq \hat{P}\hat{X}$. Indeed, as we will show in the following sections, the canonical commutation relation:

$$\left[\hat{X}, \hat{P}\right] \equiv \hat{X}\hat{P} - \hat{P}\hat{X} = 1 \tag{2.8}$$

underpins all the quantum effects that will be discussed in the following sections, e.g., sideband asymmetry, standard quantum limit, etc. Given its importance, let us try to build intuition as to why Eq. 2.8 might be true.

There are two sets of sequential operations involved to build the commutator: 1) $\hat{X}$ then $\hat{P}$, and 2) $\hat{P}$ then $\hat{X}$. Applying $\hat{X}$ first collapses the state to some position, X_j which may correspond to any of the momentum states within the range ΔP (Fig. 2.2a). Conversely, applying $\hat{P}$ first collapses the state to some momentum P_j, which may correspond to any of the position states within the range ΔX (Fig. 2.2b). The order therefore matters: applying one first before the other *on average* yields different states, as schematically depicted in Fig. 2.2c.

2.2 Mechanical oscillator in a thermal bath

The dynamics of a mechanical oscillator coupled to a thermal environment can be described by a stochastic differential equation: $m\ddot{\hat{x}}(t) = -k\hat{x}(t) + \hat{F}(t)$, where $\hat{F}(t)$ is the random bath force. The objective of this section is two-fold: 1) to determine the temperature of the mechanical mode in terms of the statistical properties of $\hat{F}(t)$; and 2) to derive the mechanical susceptibility describing the linear response of the system to $\hat{F}(t)$.

2.2.1 Independent oscillator model

The dynamics of a quantum harmonic oscillator (mass m, spring constant k) interacting with a thermal bath can be described by the so-called independent oscillator model [66], where an ensemble of independent harmonic oscillators (mass m_j, spring constant k_j) is coupled to the position of the system (see Fig. 2.3):

$$\begin{aligned} \hat{H} &= \hat{H}_{\mathrm{sys}} + \hat{H}_{\mathrm{bath}} \\ &= \frac{\hat{p}^2}{2m} + \frac{k\hat{x}}{2} + \sum_j \left[\frac{\hat{p}_j^2}{2m_j} + \frac{k_j}{2}(\hat{x}_j^2 - \hat{x})^2\right], \end{aligned} \tag{2.9}$$

where $\hat{x}$ and $\hat{p}$ is the position and momentum (in real units) of the center-of-mass coordinate of a mechanical oscillator, with $[\hat{x}, \hat{p}] = \mathrm{i}\hbar$.

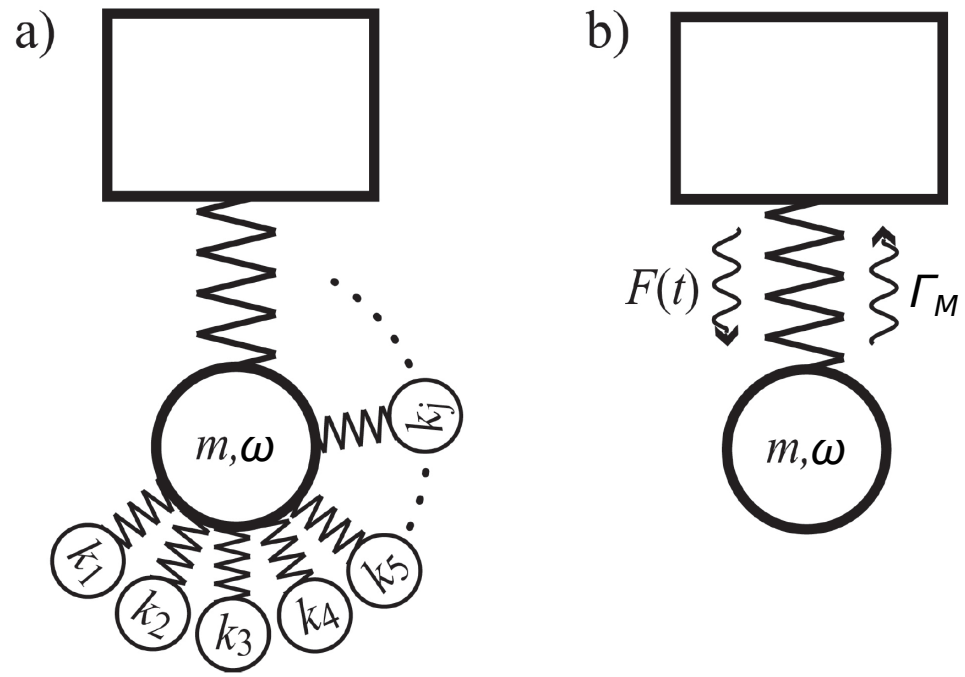

Figure 2.3: **(a)** Independent oscillator model. The mechanical oscillator (mass m, frequency ω) is coupled to an infinite number of bath modes (spring constant k_j for the jth bath oscillator, $m \gg m_j$), whose collective effect on the system is to introduce **(b)** a fluctuating force $F(t)$ and a damping force characterised by the damping rate Γ_{M}. Figure adapted from [3].

The interaction term has the form $H_{\mathrm{int}} = \hat{F}\hat{x}$, with the bath force

$$\hat{F}(t) = -\sum k_j \hat{x}_j(t), \tag{2.10}$$

which appears as an additional term in the second-order ordinary differential equation (ODE) for the system:

$$m\ddot{\hat{x}}(t) = -k\hat{x}(t) + \hat{F}(t). \tag{2.11}$$

2.2.2 Temperature of the mechanical oscillator

A thermal force such as Eq. 2.10 drives both upward and downward transitions between eigenstates $|n\rangle$ of the mechanical oscillator. In thermal equilibrium, these transition rates γ obey the so-called principle of "detailed balance":

$$p(n)\gamma_{n\to n+1} = p(n+1)\gamma_{n+1\to n}, \tag{2.12}$$

which is a quantum-theoretic way of saying that the energy gained by the system due to bath collisions should be dissipated back, by the same mechanism, into the environment. Of course, in the quantum case, the system is prepared in a superposition state $|\psi\rangle = \sum_n p_n |n\rangle$, where the probability $p(n)$ of having a phonon occupation n and energy $E_n =$

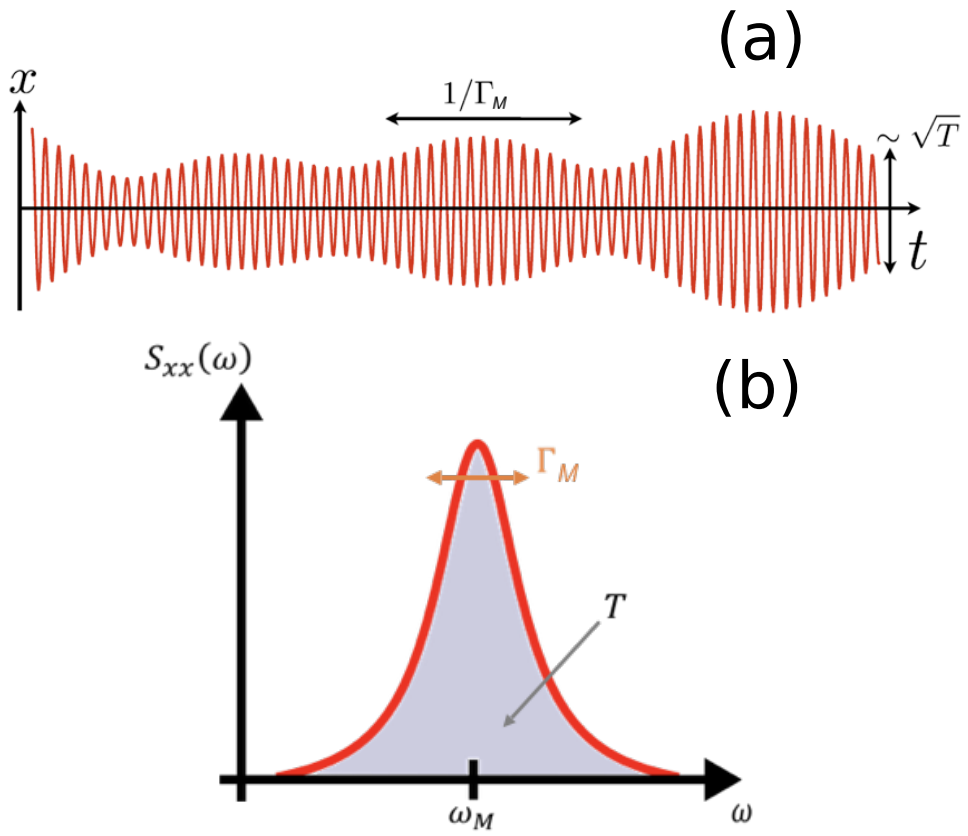

Figure 2.4: **(a)** Schematic diagram of the fluctuations in the phase and amplitude of the mechanical oscillator due to coupling with the bath modes. The fluctuations happen at a time scale $1/\Gamma_{\mathrm{M}}$ set by the damping rate. The variance in the mechanical displacements is proportional to $\sim \sqrt{T}$. **(b)** Power spectral density (PSD) $S_{xx}(\omega)$ of the mechanical displacements obtained by taking the square of the Fourier transform of the time-series **(a)**. The temperature is the area under the mechanical sideband. Optomechanical experiments usually take a continuous measurement of some quadrature and perform the analysis in frequency space through PSD's. Figures courtesy of Dr. James Millen.

$n\hbar\omega$ is given by the Bose-Einstein distribution:

$$p(n) = \exp\left(\frac{-\hbar\omega n}{k_{\mathrm{B}}T}\right)\left[1 - \exp\left(\frac{-\hbar\omega}{k_{\mathrm{B}}T}\right)\right]. \tag{2.13}$$

Substituting Eq. 2.13 in Eq. 2.12, the temperature of the mechanical oscillator in thermal equilibrium is:

$$T = \frac{\hbar\omega}{k_{\mathrm{B}}}\left[\ln\left(\frac{\gamma_{n\to n+1}}{\gamma_{n+1\to n}}\right)\right]^{-1}, \tag{2.14}$$

which shows that $T \to 0$ when the downward rate dominates, and $T \to \pm\infty$ as $\gamma_{n\to n+1} - \gamma_{n+1\to n} \to 0^{\pm}$. The thermal force causes fluctuations in the amplitude and phase of a harmonic oscillator at the time scale set by Γ_{M}, as shown in Fig. 2.4a. In optomechanical experiments, the temperature of the oscillator is given by the area under the power spectral density $S_{xx}(\omega)$ of the mechanical displacements (Fig. 2.4b). The power spectral density (PSD) is defined in Appendix A.6.

While Eq. 2.14 is a sensible analytical result, it does not connect very well with

experiments where transition rates are hardly ever measured directly. Instead, we want to relate the temperature with experimentally relevant quantities such as the force power spectral density $S_{\rm FF}(\omega)$. The Wiener-Khinchin theorem states that the PSD is equal to the Fourier transform of the autocorrelation function (see Appendix A for proof):

$$S_{FF}(\omega) = \int_{-\infty}^{\infty} \mathrm{e}^{\mathrm{i}\omega t} \left\langle \hat{F}(t)\hat{F}^{\dagger}(0) \right\rangle, \tag{2.15}$$

provided that noises are stationary: $\left\langle \hat{F}(t)\hat{F}^{\dagger}(0) \right\rangle = \left\langle \hat{F}(0)\hat{F}^{\dagger}(-t) \right\rangle$. It is easy to see then that under this condition, the negative spectrum:

$$\begin{aligned} S_{FF}(-\omega) &= \int_{-\infty}^{\infty} \mathrm{d}t \mathrm{e}^{-\mathrm{i}\omega t} \left\langle \hat{F}(t)\hat{F}^{\dagger}(0) \right\rangle \\ &= \int_{-\infty}^{\infty} \mathrm{d}t \mathrm{e}^{\mathrm{i}\omega t} \left\langle \hat{F}(-t)\hat{F}^{\dagger}(0) \right\rangle \\ &= \int_{-\infty}^{\infty} \mathrm{d}t \mathrm{e}^{\mathrm{i}\omega t} \left\langle \hat{F}(0)\hat{F}^{\dagger}(t) \right\rangle \neq S_{FF}(\omega) \end{aligned} \tag{2.16}$$

because quantum forces do not commute at different times. This sideband asymmetry is one of the hallmarks of the quantum regime and was experimentally observed in [28].

Let us now derive the transition probability as a function of $S_{FF}(\omega)$, closely following [3]. We assume that the state of the combined system remains separable as it evolves from its intial state $|\psi_{\rm sys}\rangle \bigotimes |\psi_{\rm bath}\rangle = |n\rangle \bigotimes |j\rangle \equiv |n, j\rangle$ to the final state $|n+1, k\rangle$. If the bath force (Eq. 2.10) is weak enough, we can treat $\hat{H}_{\rm int}$ as a perturbation to the bare oscillator Hamiltonians. Time-dependent perturbation theory gives:

$$\begin{aligned} A_{i\to f} &= -\frac{\mathrm{i}}{\hbar} \int_0^t \mathrm{d}t_1 \mathrm{e}^{\mathrm{i}\omega t_1} \langle n+1, k|\hat{F}(t_1)\hat{x}|n, j\rangle \\ &= -\frac{\mathrm{i}}{\hbar} \int_0^t \mathrm{d}t_1 \mathrm{e}^{\mathrm{i}\omega t_1} \langle n+1|\hat{x}|n\rangle \ \langle k|\hat{F}(t_1)|j\rangle \\ &= -\frac{\mathrm{i}x_{\rm zpf}\sqrt{n+1}}{\hbar} \int_0^t \mathrm{d}t_1 \mathrm{e}^{\mathrm{i}\omega t_1} \langle k|\hat{F}(t_1)|j\rangle \,. \end{aligned} \tag{2.17}$$

Summing over the bath modes, the upward transition probability is:

$$\begin{aligned} P_{n\to n+1} &\equiv \sum_k |A_{i\to f}|^2 \\ &= \frac{x_{\rm zpf}^2(n+1)}{\hbar^2} \int_0^t \mathrm{d}t_2 \int_0^t \mathrm{d}t_1 \mathrm{e}^{\mathrm{i}\omega(t_1-t_2)} \sum_k \langle j|\hat{F}(t_2)|k\rangle \ \langle k|\hat{F}(t_1)|j\rangle \\ &= \frac{x_{\rm zpf}^2(n+1)}{\hbar^2} \int_0^t \mathrm{d}t_2 \int_0^t \mathrm{d}t_1 \mathrm{e}^{\mathrm{i}\omega(t_1-t_2)} \left\langle \hat{F}(t_2)\hat{F}(t_1) \right\rangle, \end{aligned} \tag{2.18}$$

where we have assumed the completeness and orthonormality of the bath modes: $\sum_k |k\rangle\langle k| = 1$. A quick look at Eq. 2.15 tells us that the inner integral could be written as a PSD

(power spectral density). Setting $t_1 = \tau + t'$ and $t_2 = t'$ and approximating the limit of integration with $\pm\infty$, we obtain

$$\begin{aligned} P_{n\to n+1} &\equiv \sum_k |A_{i\to f}|^2 \\ &= \frac{x_{\rm zpf}^2(n+1)}{\hbar^2}\int_0^t \mathrm{d}t' \int_{-\infty}^{\infty} \mathrm{d}\tau \mathrm{e}^{\mathrm{i}\omega\tau}\left\langle \hat{F}(t')\hat{F}(\tau+t')\right\rangle \\ &= \frac{x_{\rm zpf}^2(n+1)}{\hbar^2} t S_{FF}(-\omega) \end{aligned} \tag{2.19}$$

Finally, the upward transition rate $\mathrm{d}P_{n\to n+1}/\mathrm{d}t$ is:

$$\gamma_{n\to n+1} = \frac{x_{\rm zpf}^2(n+1)}{\hbar^2} S_{FF}(-\omega) \tag{2.20}$$

The downward transition rate is the time-reversal of $\gamma_{n\to n+1}$ which, in frequency space, amounts to a parity inversion:

$$\gamma_{n+1\to n} = \frac{x_{\rm zpf}^2(n+1)}{\hbar^2} S_{FF}(\omega) \tag{2.21}$$

Using Eqs. 2.20 and 2.21 in Eq. 2.14, the damping rate is then:

$$\Gamma_{\rm M} = \frac{x_{\rm zpf}^2(n+1)}{\hbar^2}[S_{FF}(\omega) - S_{FF}(-\omega)] \tag{2.22}$$

Substituting Eqs. 2.20 and 2.21 in Eq. 2.14, the temperature of the mechanical oscillator in terms of the bath force PSD is:

$$T = \frac{\hbar\omega}{k_{\rm B}}\left[\ln\left(\frac{S_{FF}(\omega)}{S_{FF}(-\omega)}\right)\right]^{-1}, \tag{2.23}$$

In terms of the mean phonon occupation $\bar{n} = kT/\hbar\omega$,

$$\bar{n} = \frac{S_{FF}(-\omega)}{S_{FF}(\omega) - S_{FF}(-\omega)}. \tag{2.24}$$

In the classical limit of a symmetric spectrum, $\bar{n} \to \infty$.

2.2.3 Mechanical susceptibility

Let us now derive the mechanical susceptibility describing the linear response of the mechanical oscillator to the random bath force $\hat{F}(t)$. Going back to Eq. 2.9, one can obtain a

second-order ODE for the bath mode:

$$m\ddot{\hat{x}}_j(t) = -\sum_j k_j \left[\hat{x}_j(t) - \hat{x}(t)\right] \tag{2.25}$$

Without specifying a microscopic model for the bath, Langevin proposed that the bath force $\hat{F}(t) = \bar{F} + \hat{\mathcal{F}}(t)$ be decomposed as a sum of a mean and a fluctuating force to capture, respectively, the damping and heating processes observed in Brownian motion. Indeed, these mean and fluctuating components correspond to the homogeneous and particular solutions of Eq. 2.25:

$$\hat{x}_j(t) = \hat{x}_j^h(t) - \Gamma_{\mathrm{M}}\dot{\hat{x}}, \tag{2.26}$$

where the random fluctuating force $\hat{\mathcal{F}}(t) = m\hat{x}_j^h(t)$, and the mean is identified with the damping force $\bar{F} = -\Gamma_{\mathrm{M}}\dot{\hat{x}}$ in the Markovian limit. Substituting Eq. 2.26 in Eq. 2.11, we obtain:

$$\ddot{\hat{x}}(t) + \omega_{\mathrm{M}}^2\hat{x}(t) + \Gamma_{\mathrm{M}}\dot{\hat{x}} = \frac{\hat{\mathcal{F}}(t)}{m}, \tag{2.27}$$

which in Fourier space becomes:

$$\hat{x}(\omega) = \mu(\omega)\hat{\mathcal{F}}(\omega). \tag{2.28}$$

We will specify the statistical properties of $\hat{\mathcal{F}}$ later in Sec. 2.3.2. For now, it suffices to say that the response $\hat{x}(\omega)$ of the oscillator to an external random force $\hat{\mathcal{F}}(\omega)$ is local in frequency space, and is described by the mechanical susceptibility:

$$\mu(\omega) \equiv \left[m\left(\omega_{\mathrm{M}}^2 - \omega^2 - \mathrm{i}\omega\Gamma_{\mathrm{M}}\right)\right]^{-1} \tag{2.29}$$

The real and imaginary parts of Eq. 2.29 are called the reactive and dissipative response, which capture the frequency shift and damping experienced by the system due to a fluctuating force from the environment. As we have seen from Eq. 2.26, both effects have the same origin, and so are naturally connected. In particular, the fluctuation-dissipation theorem connects the fluctuation of the system with the imaginary part of its linear response function:

$$S_{xx}(\omega) = (\bar{n} + 1)\,\mathrm{Im}[\mu(\omega)], \tag{2.30}$$

which is just another manifestation of the previous result relating $S_{FF}(\omega)$ with the damping rate. In the same way that the upward and downward transitions are different, we have:

$$S_{xx}(-\omega) = \bar{n}\,\mathrm{Im}[\mu(\omega)]. \tag{2.31}$$

Figure 2.5 illustrates sideband asymmetry in the displacement spectrum of a mechanical oscillator near ground state.

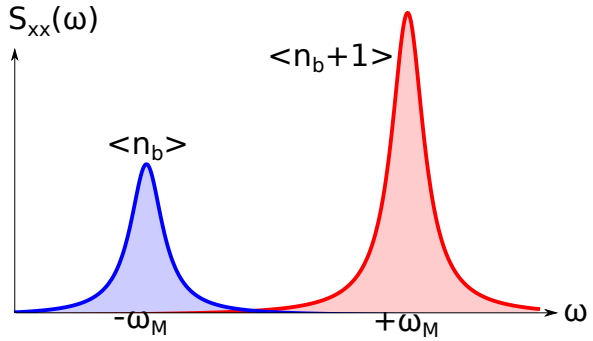

Figure 2.5: Positive and negative frequency displacement spectrum representing the number of quanta absorbed and emitted by a mechanical oscillator in the quantum ground state. Sideband asymmetry in $S_{xx}(\omega)$ is one of the hallmarks of the quantum regime, and has been experimentally observed in [4]. The non-commmutation of $\hat{x}$ and $\hat{p}$ causes an imaginary autocorrelation function, leading to an asymmetric spectrum. The area under each of the mechanical sidebands is proportional to $\bar{n}_{\rm b}$ and $\bar{n}_{\rm b}+1$; in the ground state $\bar{n}_{\rm b}=0$, so the quantum oscillator can only absorb vacuum energy, leading to zero-point fluctuations. However, in the classical limit $\bar{n}_{\rm b}\approx\bar{n}_{\rm b}+1$, so no asymmetry is observed.

Equations 2.23 and 2.28 are the main results of this discussion, where we have so far assumed a thermal bath force. In the following sections, we consider how one could engineer the temperature and the susceptibility of a mechanical oscillator through optical forces.

2.3 Canonical optomechanical system

Numerous experiments in optomechanics have been realized both in the optical and microwave domains, spanning many orders of mechanical frequencies and masses (for a comprehensive review, see [19]). Nonetheless, the dynamics are well-described by the canonical optomechanical system comprised of a Fabry-Pérot cavity with one harmonically-bound mirror — such a system is described by a two harmonic oscillator Hamiltonian characterized by a mechanical frequency $\omega_{\rm M}$ and a parametrically coupled cavity resonance frequency $\omega_{\rm c}(\hat{x})$, where $\hat{x}$ is the mirror's position (Fig. 2.6):

$$\hat{H}=\hbar\omega_{\rm c}(\hat{x})\hat{a}^\dagger\hat{a}+\hbar\omega_{\rm M}\hat{b}^\dagger\hat{b}, \tag{2.32}$$

where $\hat{a},\hat{a}^\dagger$ ($\hat{b},\hat{b}^\dagger$) are the ladder operators for the cavity (mechanical) mode.

This so-called "dispersive coupling" can be understood as follows: the position $\hat{x}$ of the compliant mirror changes the cavity length, which in turn modifies $\omega_{\rm c}$ and, consequently, the intracavity photon number $\hat{a}^\dagger\hat{a}$. The mirror's position shifts in response to the change in the radiation pressure force, thus creating an optomechanical feedback loop (see Fig. 2.8).

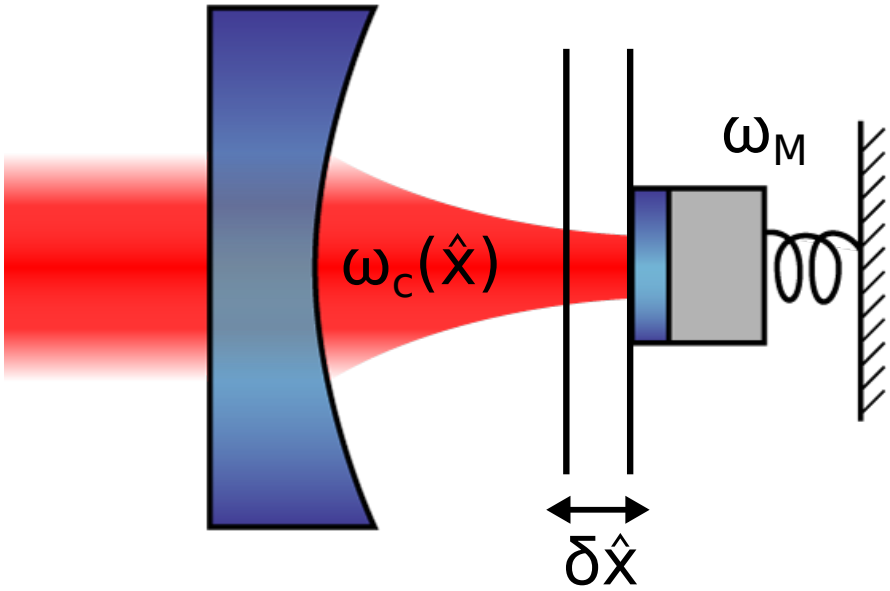

Figure 2.6: Canonical optomechanical system. Using a high-Q optical cavity amplifies the radiation pressure force which causes mechanical oscillations (frequency, ω_{M}). Mechanical motion changes the cavity length, leading to a dispersive interaction $\omega_{\mathrm{c}}(\hat{x})$. Depending on the detuning $\Delta = \omega_{\mathrm{l}} - \omega_{\mathrm{c}}$, the cavity can be used for measurement and control of mechanical motion.

We Taylor expand $\omega_{\mathrm{c}}(\hat{x})$, and define the optomechanical coupling

$$G = -\,\partial\omega_{\mathrm{c}}(\hat{x})/\partial\hat{x}\ , \tag{2.33}$$

where the negative sign convention is chosen to show ω_{c} decreases with longer cavity length. Moving into a reference frame rotating with the laser frequency ω_{l}, Eq. 2.32 becomes:

$$\hat{H} = -\hbar\Delta\hat{a}^{\dagger}\hat{a} + \hbar\omega_{\mathrm{M}}\hat{b}^{\dagger}\hat{b} - \hbar G\hat{a}^{\dagger}\hat{a}\hat{x} \tag{2.34}$$

where the cavity detuning $\Delta = \omega_{\mathrm{l}} - \omega_{\mathrm{c}}$. In terms of the ladder operators, the interaction Hamiltonian:

$$\hat{H}_{\mathrm{int}} = -\hbar g_0\hat{a}^{\dagger}\hat{a}(\hat{b} + \hat{b}^{\dagger}), \tag{2.35}$$

where we define $g_0 = Gx_{\mathrm{zpf}}$ as the single photon optomechanical coupling strength. The three-wave mixing interaction term gives rise to a host of nonlinear effects [67, 68, 69] and suitably describes single photon dynamics [70]. However, current g_0 are notoriously weak given that x_{zpf} are small, so most experimental advances in optomechanical cooling [1, 2], squeezing and entanglement [37, 40], and phase-senstive detection near the standard quantum limit (SQL) have been made in the regime of large intracavity photon numbers. In this thesis, we are mainly interested in the linearised form of Eq. 2.34.

2.3.1 Linearised Hamiltonian

For large intracavity photon numbers, we can identify the operator as the sum of a large classical mean value and a small quantum fluctuation: $\hat{a} \to \bar{\alpha} + \hat{a}$ (we do the same for the position: $\hat{x} \to x_0 + \hat{x}$). Placing the origin at $x_0 = 0$, the interaction term then becomes: $G\left[|\bar{\alpha}|^2\hat{x} + (\bar{\alpha}^*\hat{a} + \bar{\alpha}\hat{a}^\dagger)\hat{x} + \hat{a}^\dagger\hat{a}\hat{x}\right]$. The first term can be omitted from the dynamics by an appropriate shift of the origin, while the last term are negligible fluctuations. We keep only the middle term, where we assume without loss of generality $\bar{\alpha} = \bar{\alpha}^*$. Equation 2.34 then becomes a Hamiltonian quadratic in the operators:

$$\hat{H} = -\hbar\Delta\hat{a}^\dagger\hat{a} + \hbar\omega_{\mathrm{M}}\hat{b}^\dagger\hat{b} + \hbar g(\hat{a} + \hat{a}^\dagger)(\hat{b} + \hat{b}^\dagger), \tag{2.36}$$

resulting in equations of motion that are linear. One can then see that having many intracavity photons enhances the optomechanical coupling: $g = |\bar{\alpha}|g_0$, allowing for coherent optomechanical effects.

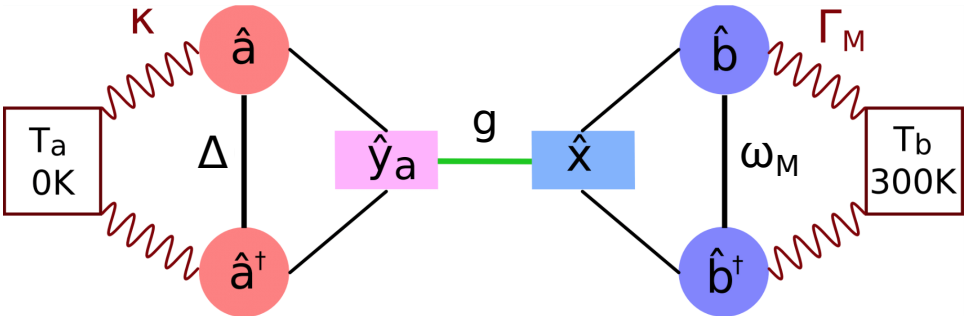

Figure 2.7: Schematic diagram of the linearised optomechanical interaction, described by a two-mode oscillator Hamiltonian. Δ, ω_{M} are the cavity and mechanical frequencies, g is the (light-enhanced) optomechanical coupling, which connects the position quadrature $\hat{X} = (\hat{b} + \hat{b}^\dagger)/\sqrt{2}$ with the optical amplitude quadrature $\hat{Y}_{\mathrm{a}} = (\hat{a} + \hat{a}^\dagger)/\sqrt{2}$. The dissipative dynamics is characterised by the cavity and mechanical damping rates κ and Γ_{M}. Typically the cavity mode is in the ground state, although laser and electronic noises may prevent the system from being shot noise limited. Meanwhile, the mechanical oscillator may be precooled cryogenically, although in levitated schemes, the system is initially thermalised to room temperature.

The Heisenberg's equation of motion can be straightforwardly obtained: $\dot{\hat{c}} = -\frac{\mathrm{i}}{\hbar}[\hat{c}, \hat{H}]$ to describe the closed system dynamics. However, for a complete and realistic model, one must account for dissipative process, e.g. due to photon scattering or clamping losses using the Langevin equations.

2.3.2 Langevin equations

Langevin equations are stochastic differential equations which can model the Brownian motion of a particle in a heat bath. They are the starting point of most analysis in optomechanics so considerable attention is given to their derivation with and without

rotating wave approximation.

Independent from any microscopic model of the bath, the Langevin equation — by virtue of being a continuous Markov process — has to obey a rather strict mathematical form (see Appendix B.2.1 for a discussion):

$$\dot{\hat{c}}(t) = -\frac{\mathrm{i}}{\hbar}[\hat{c}, \hat{H}] - \frac{\gamma}{2}\hat{c}(t) + \sqrt{\gamma}\hat{c}_{\mathrm{in}}(t), \tag{2.37}$$

where γ is a damping rate, and $\hat{c}_{\mathrm{in}}(t)$ is a Gaussian, delta-correlated input noise. However, we show in Appendix B.1 that starting from the independent oscillator model we obtain instead:

$$\dot{\hat{c}}(t) = -\frac{\mathrm{i}}{\hbar}[\hat{c}, \hat{H}] - \frac{\gamma}{2}\hat{c}(t) + \sqrt{\gamma}\hat{c}_{\mathrm{in}}(t) - \varsigma\mathcal{R}(\hat{c}), \tag{2.38}$$

where $\mathcal{R}(\hat{c}) \equiv \frac{\gamma}{2}\hat{c}^{\dagger} + \sqrt{\gamma}\hat{c}^{\dagger}_{\mathrm{in}}$. The coefficient ς can be either 0 or 1, corresponding to equations derived from the independent oscillator model with or without RWA. The latter case gives Eq. 2.37.

Time-domain Langevin equations without RWA

Given both the cavity and mechanical modes are coupled to their respective baths via the damping rates κ and Γ_{M}, the Langevin equations for the optomechanical system are then:

$$\dot{\hat{a}}(t) = -\frac{\mathrm{i}}{\hbar}[\hat{a}, \hat{H}] - \frac{\kappa}{2}\hat{a}(t) + \sqrt{\kappa}\hat{a}_{\mathrm{in}}(t) - \varsigma\mathcal{R}(\hat{a}) \tag{2.39}$$

$$\dot{\hat{b}}(t) = -\frac{\mathrm{i}}{\hbar}[\hat{b}, \hat{H}] - \frac{\Gamma_{\mathrm{M}}}{2}\hat{b}(t) + \sqrt{\Gamma_{\mathrm{M}}}\hat{b}_{\mathrm{in}}(t) - \varsigma\mathcal{R}(\hat{b}) \tag{2.40}$$

where $\hat{H}$ is the linearised optomechanical Hamiltonian in Eq. 2.36, while $\varsigma = 0$ and $\varsigma = 1$ denotes with and without RWA, respectively. The input noises have the following correlators:

$$\left\langle \hat{a}_{\mathrm{in}}(t)\hat{a}^{\dagger}_{\mathrm{in}}(t') \right\rangle = (\bar{n}_{\mathrm{a}} + 1)\delta(t - t') \tag{2.41}$$

$$\left\langle \hat{a}^{\dagger}_{\mathrm{in}}(t)\hat{a}_{\mathrm{in}}(t') \right\rangle = \bar{n}_{\mathrm{a}}\delta(t - t')$$

$$\left\langle \hat{b}_{\mathrm{in}}(t)\hat{b}^{\dagger}_{\mathrm{in}}(t') \right\rangle = (\bar{n}_{\mathrm{b}} + 1)\delta(t - t') \tag{2.42}$$

$$\left\langle \hat{b}^{\dagger}_{\mathrm{in}}(t)\hat{b}_{\mathrm{in}}(t') \right\rangle = \bar{n}_{\mathrm{b}}\delta(t - t') \tag{2.43}$$

Typically, for photon shot noise, $\bar{n}_{\mathrm{a}} = 0$, while $\bar{n}_{\mathrm{b}} \approx \frac{k_B T}{\hbar\omega_{\mathrm{M}}}$ in the classical limit.

Likewise, the mechanical quadratures follow Eq. 2.37:

$$\dot{\hat{X}}(t) = -\frac{\mathrm{i}}{\hbar}[\hat{X},\hat{H}] - (1+\varsigma)\frac{\Gamma_\mathrm{M}}{2}\hat{X}(t) + \sqrt{(1-\varsigma)\Gamma_\mathrm{M}}\hat{X}_\mathrm{in}(t) \tag{2.44}$$

$$\dot{\hat{P}}(t) = -\frac{\mathrm{i}}{\hbar}[\hat{P},\hat{H}] - (1-\varsigma)\frac{\Gamma_\mathrm{M}}{2}\hat{P}(t) + \sqrt{(1+\varsigma)\Gamma_\mathrm{M}}\hat{P}_\mathrm{in}(t), \tag{2.45}$$

where the quadrature input noises have the following correlators:

$$\left\langle \hat{X}_\mathrm{in}(t)\hat{X}_\mathrm{in}(t')\right\rangle = \left\langle \hat{P}_\mathrm{in}(t)\hat{P}_\mathrm{in}(t')\right\rangle = \left(\bar{n}_\mathrm{b}+\frac{1}{2}\right)\delta(t-t') \tag{2.46}$$

$$\left\langle \hat{X}_\mathrm{in}(t)\hat{P}_\mathrm{in}(t')\right\rangle = -\left\langle \hat{P}_\mathrm{in}(t)\hat{X}_\mathrm{in}(t')\right\rangle = \frac{\mathrm{i}}{2}\delta(t-t') \tag{2.47}$$

Similar equations can be obtained for $\hat{Y}_\mathrm{a}$ and $\hat{Y}_\mathrm{p}$ of the cavity mode. The effect of RWA ($\varsigma = 0$) then is to equally distribute the damping and fluctuations to the quadratures, which would have otherwise been localized in either one of the quadratures.

Frequency-space Langevin equations without RWA

We now turn into Fourier space, where most analysis in optomechanics are done. From Eq. 2.44 and its optical equivalent, the amplitude quadratures are:

$$\hat{Y}_\mathrm{a}(\omega) = \eta(\omega)\left[\sqrt{2\kappa}\hat{Y}_\mathrm{p,in}(\omega) + 2g\hat{X}(\omega)\right] \tag{2.48}$$

$$\hat{X}(\omega) = \mu(\omega)\left[\sqrt{2\Gamma_\mathrm{M}}\hat{P}_\mathrm{in}(\omega) + 2g\hat{Y}_\mathrm{a}(\omega)\right] \tag{2.49}$$

where

$$\eta(\omega) \equiv -\Delta\left[\Delta^2 - \omega^2 - \mathrm{i}\kappa\omega\right]^{-1} \tag{2.50}$$

$$\mu(\omega) \equiv \omega_\mathrm{M}\left[\omega_\mathrm{M}^2 - \omega^2 - \mathrm{i}\Gamma_\mathrm{M}\omega\right]^{-1} \tag{2.51}$$

are the mechanical and optical susceptibilities *without* RWA. Meanwhile, from Eq. 2.45 and its optical equivalent, the phase quadratures $\hat{Y}_\mathrm{p}(\omega)$ and $\hat{P}(\omega)$ are:

$$\hat{Y}_\mathrm{p}(\omega) = \eta'(\omega)\left[\sqrt{2\kappa}\hat{Y}_\mathrm{p,in}(\omega) + 2g\hat{X}(\omega)\right] \tag{2.52}$$

$$\hat{P}(\omega) = \mu'(\omega)\left[\sqrt{2\Gamma_\mathrm{M}}\hat{P}_\mathrm{in}(\omega) + 2g\hat{Y}_\mathrm{a}(\omega)\right] \tag{2.53}$$

where

$$\eta'(\omega) \equiv (\kappa - \mathrm{i}\omega)\left[\Delta^2 - \omega^2 - \mathrm{i}\kappa\omega\right]^{-1} \tag{2.54}$$

$$\mu'(\omega) \equiv (\Gamma_\mathrm{M} - \mathrm{i}\omega)\left[\omega_\mathrm{M}^2 - \omega^2 - \mathrm{i}\Gamma_\mathrm{M}\omega\right]^{-1} \tag{2.55}$$

Frequency-space Langevin equations with RWA

Let us now investigate the Langevin equations in RWA. Equation 2.39 and 2.40 in Fourier space becomes:

$$\hat{a}(\omega) = \chi_{\rm C}(\omega)\left[\sqrt{\kappa}\hat{a}_{\rm in}(t) + {\rm i}\sqrt{2}g\hat{X}\right] \tag{2.56}$$

$$\hat{b}(\omega) = \chi_{\rm M}(\omega)\left[\sqrt{\Gamma_{\rm M}}\hat{b}_{\rm in}(t) + {\rm i}\sqrt{2}g\hat{Y}_{\rm a}\right], \tag{2.57}$$

where

$$\chi_{\rm C}(\omega) \equiv \left[-{\rm i}(\omega+\Delta) + \frac{\kappa}{2}\right]^{-1} \tag{2.58}$$

$$\chi_{\rm M}(\omega) \equiv \left[-{\rm i}(\omega-\omega_{\rm M}) + \frac{\Gamma_{\rm M}}{2}\right]^{-1}. \tag{2.59}$$

are the cavity and mechanical susceptibilities in RWA.

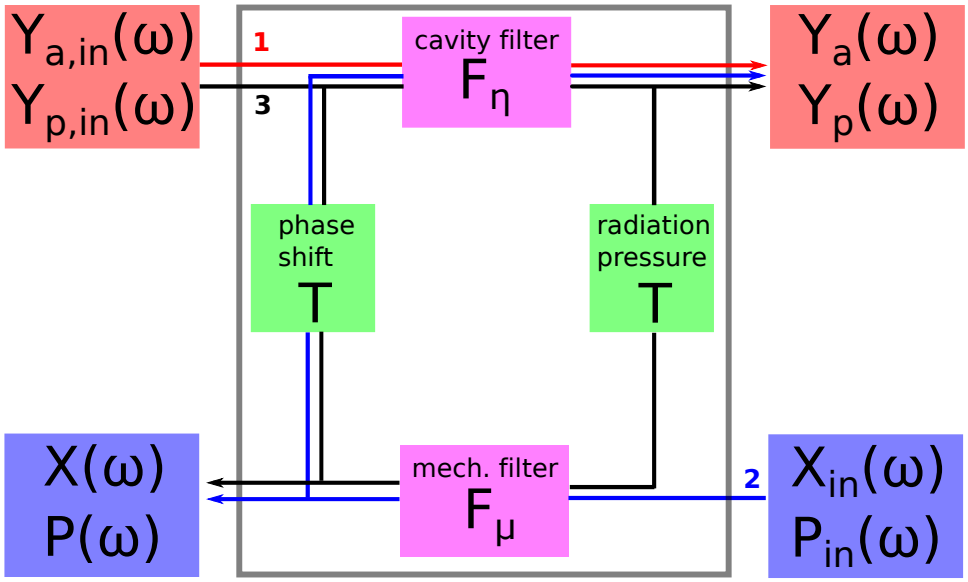

Figure 2.8: Linear optomechanical amplifier model of cavity optomechanics [5]. The optomechanical system (enclosed in a box) is a two-port amplifier which amplifies input noises $\hat{X}_{\rm in}, \hat{P}_{\rm in}$ and $\hat{Y}_{\rm a,in}, \hat{Y}_{\rm p,in}$ from mechanical and cavity baths, via a series of filters F and transducers T in order to obtain the optical and mechanical quadrature. The amplifier model makes it easier to visualise the quadratures in terms of the sum input noises, which is useful in computing the PSD, as the input noises have known correlation properties. For example, the optical quadratures $\hat{Y}_{\rm a}, \hat{Y}_{\rm p}$ have three noise contributions: 1) the imprecision noise, which is just the cavity-filtered optical noise (red), 2) the thermal noise from the mechanical bath which is transduced as optical phase shifts (blue), and 3) the backaction noise, which is measurement-induced disturbance to mechanical motion due to radiation pressure force (black).

Let us focus on the cavity dynamics first. From Eq. 2.56,

$$\hat{Y}_{\rm a}(\omega) = \eta^{\rm RWA}(\omega)\left[\sqrt{\kappa}\hat{Y}_{\rm p,in}(\omega) + 2g\hat{X}(\omega)\right] + \eta'^{\rm RWA}(\omega)\sqrt{\kappa}\hat{Y}_{\rm a,in}(\omega) \tag{2.60}$$

$$\hat{Y}_{\rm p}(\omega) = \eta'^{\rm RWA}(\omega)\left[\sqrt{\kappa}\hat{Y}_{\rm p,in}(\omega) + 2g\hat{X}(\omega)\right] + \eta^{\rm RWA}(\omega)\sqrt{\kappa}\hat{Y}_{\rm a,in}(\omega) \tag{2.61}$$

where

$$\eta^{\mathrm{RWA}}(\omega) = \frac{\mathrm{i}}{2}[\chi_{\mathrm{C}}(\omega) - \chi_{\mathrm{C}}^{*}(-\omega)] \tag{2.62}$$

$$\eta'^{\mathrm{RWA}}(\omega) = \frac{1}{2}[\chi_{\mathrm{C}}(\omega) + \chi_{\mathrm{C}}^{*}(-\omega)]. \tag{2.63}$$

Comparing with Eq. 2.52, we see two differences. First, the input phase noise has been partly converted into amplitude noise filtered with a different susceptiblity. These changes are consistent with the earlier observation that the RWA distributes damping and fluctuations equally between the quadratures. Second, the cavity susceptibility has changed; though one can easily show that $\eta^{\mathrm{RWA}}(\omega) \to \eta(\omega)$ by applying RWA.

In addition, comparing Eq. 2.52 with Eq. 2.60, we find that at $\Delta = 0$, the noises completely vanish when RWA is *not* applied; otherwise, we obtain $\hat{Y}_{\mathrm{a}}(\omega) = \eta'^{\mathrm{RWA}}(\omega)\sqrt{\kappa}\hat{Y}_{\mathrm{a,in}}(\omega)$ (as will be discussed in Sec. 2.5, this constitutes the backaction noise in the phase noise spectrum). It is common in optomechanics literature to assume RWA in the optical field.

Analogous equations can be easily obtained for the mechanical mode:

$$\hat{X}(\omega) = \mu^{\mathrm{RWA}}(\omega)\left[\sqrt{\Gamma_{\mathrm{M}}}\hat{P}_{\mathrm{in}}(\omega) + 2g\hat{Y}_{\mathrm{a}}(\omega)\right] + \mu'^{\mathrm{RWA}}(\omega)\sqrt{\Gamma_{\mathrm{M}}}\hat{X}_{\mathrm{in}}(\omega) \tag{2.64}$$

$$\hat{P}(\omega) = \mu'^{\mathrm{RWA}}(\omega)\left[\sqrt{\Gamma_{\mathrm{M}}}\hat{P}_{\mathrm{in}}(\omega) + 2g\hat{Y}_{\mathrm{a}}(\omega)\right] + \mu^{\mathrm{RWA}}(\omega)\sqrt{\Gamma_{\mathrm{M}}}\hat{X}_{\mathrm{in}}(\omega) \tag{2.65}$$

where

$$\mu^{\mathrm{RWA}}(\omega) = \frac{\mathrm{i}}{2}[\chi_{\mathrm{M}}(\omega) - \chi_{\mathrm{M}}^{*}(-\omega)] \tag{2.66}$$

$$\mu'^{\mathrm{RWA}}(\omega) = \frac{1}{2}[\chi_{\mathrm{M}}(\omega) + \chi_{\mathrm{M}}^{*}(-\omega)]. \tag{2.67}$$

In summary, it is possible to write the Langevin equations in matrix form:

$$\begin{pmatrix} \hat{Y}_{\mathrm{a}} \\ \hat{Y}_{\mathrm{p}} \end{pmatrix} = \mathbf{F}_{\eta}\left[\mathbf{T}\begin{pmatrix} \hat{X} \\ \hat{P} \end{pmatrix} + \sqrt{\kappa}\begin{pmatrix} \hat{Y}_{\mathrm{a,in}} \\ \hat{Y}_{\mathrm{p,in}} \end{pmatrix}\right] \tag{2.68}$$

$$\begin{pmatrix} \hat{X} \\ \hat{P} \end{pmatrix} = \mathbf{F}_{\mu}\left[\mathbf{T}\begin{pmatrix} \hat{Y}_{\mathrm{a}} \\ \hat{Y}_{\mathrm{p}} \end{pmatrix} + \sqrt{\Gamma_{\mathrm{M}}}\begin{pmatrix} \hat{X}_{\mathrm{in}} \\ \hat{P}_{\mathrm{in}} \end{pmatrix}\right] \tag{2.69}$$

where the filters and transduction matrices are given by:

$$\mathbf{F}_\eta = \begin{pmatrix} \eta'^{\mathrm{RWA}} & \eta^{\mathrm{RWA}} \\ \eta^{\mathrm{RWA}} & \eta'^{\mathrm{RWA}} \end{pmatrix} \tag{2.70}$$

$$\mathbf{F}_\mu = \begin{pmatrix} \mu'^{\mathrm{RWA}} & \mu^{\mathrm{RWA}} \\ \mu^{\mathrm{RWA}} & \mu'^{\mathrm{RWA}} \end{pmatrix} \tag{2.71}$$

$$\mathbf{T} = \begin{pmatrix} 0 & 0 \\ 2g & 0 \end{pmatrix} \tag{2.72}$$

Figure 2.8 shows the linear amplifier model of optomechanics, which illustrates Eqs. 2.68 and 2.69.

2.3.3 Cavity field as an effective bath

In the following discussion, we will implicitly assume RWA in the cavity dynamics so will drop the label. Solving Eqs. 2.44 and 2.45 simultaneously, we obtain the second-order ODE:

$$\ddot{\hat{X}}(t) + \omega_{\mathrm{M}}^2 \hat{X}(t) + \Gamma_{\mathrm{M}} \dot{\hat{X}}(t) = \sqrt{2\Gamma_{\mathrm{M}}}\omega_{\mathrm{M}} \hat{P}_{\mathrm{in}}(t) + 2g\omega_{\mathrm{M}} \hat{Y}_{\mathrm{a}}(t), \tag{2.73}$$

which follows the form of Eq. 2.27. In the same way that we identified the thermal force in Sec. 2.2, the interaction term in Eq. 2.34 compels us to identify the cavity force $\hat{F}_{\mathrm{c}} = -\hbar G \hat{a}^\dagger \hat{a}$. Its linearised form (in dimensionless units) appears next to the thermal force in the RHS of Eq. 2.73, which suggests treating the cavity field as an effective bath for the mechanical oscillator. In the following, we derive the effective mechanical susceptibility due to the additional cavity force $\hat{F}_{\mathrm{c}}$.

Solving Eqs. 2.60 and 2.53 simultaneously, we obtain:

$$\hat{X}(\omega) = \mu(\omega, \Delta)\Big[\sqrt{2\Gamma_{\mathrm{M}}}\hat{P}_{\mathrm{in}}(\omega) + 2g\eta(\omega)\sqrt{\kappa}\hat{Y}_{\mathrm{p,in}}(\omega) + 2g\eta'(\omega)\sqrt{\kappa}\hat{Y}_{\mathrm{a,in}}(\omega)\Big], \tag{2.74}$$

where we identify the effective mechanical susceptibility:

$$\mu^{-1}(\omega, \Delta) = \mu^{-1}(\omega) - 4g\eta(\omega). \tag{2.75}$$

Note that we have used RWA for the cavity mode so $\eta(\omega)$ and $\eta'(\omega)$ are given by Eqs. 2.62 and 2.63.

We then see that the effect of $\hat{F}_{\mathrm{c}}$ is to modify the mechanical susceptibility, whose real and imaginary parts correspond to changes in spring constant and damping rate of the

mechanical oscillator:

$$\delta\omega_{\rm M}(\omega) \equiv {\rm Re}\{4g\eta(\omega)\} = 2g^2\left[\frac{\Delta+\omega}{(\Delta+\omega)^2+\frac{\kappa^2}{4}}+\frac{\Delta-\omega}{(\Delta-\omega)^2+\frac{\kappa^2}{4}}\right] \tag{2.76}$$

$$\Gamma_{\rm opt}(\omega) \equiv {\rm Im}\{4g\eta(\omega)\} = -g^2\kappa\left[\frac{1}{(\Delta+\omega)^2+\frac{\kappa^2}{4}}-\frac{1}{(\Delta-\omega)^2+\frac{\kappa^2}{4}}\right] \tag{2.77}$$

2.4 Optomechanical cooling

The results of the previous section immediately lend itself to the analysis of cavity cooling. The cavity field acts as an effective bath force $\hat{F}_{\rm c} = \hbar x_{\rm zpf} g \hat{Y}_{\rm a}$ that changes the damping rate of the mechanical oscillator, depending on the detuning. From Fig. 2.9, $\Gamma_{\rm opt}$ is the highest when $\Delta = -\omega_{\rm M}$. However, an additional requirement for optomechanical cooling is being in the resolved-sideband regime, where $\kappa \ll \omega_{\rm M}$.

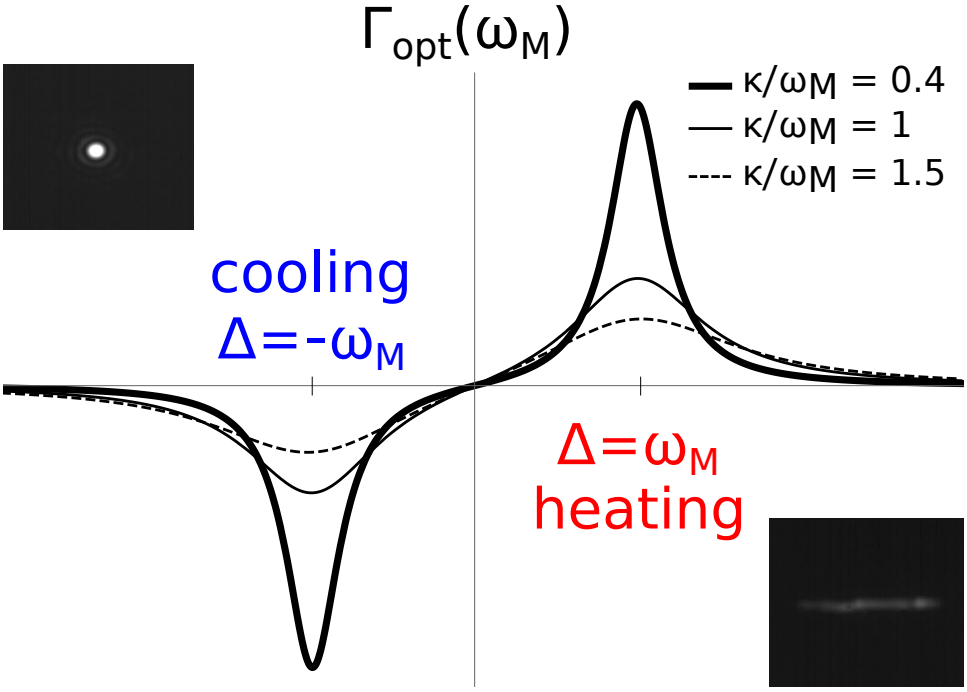

Figure 2.9: Plot of the optical damping $\Gamma_{\rm opt}(\omega = \omega_{\rm M})$ as a function of detuning Δ for different sideband resolutions: $\kappa/\omega_{\rm M} = 0.4$ (thick); $\kappa/\omega_{\rm M} = 1$ (thin); $\kappa/\omega_{\rm M} = 1.5$ (dotted). Positive damping is highest at $\Delta = \omega_{\rm M}$ which causes mechanical amplification, as shown in the scattered light image of a cavity-levitated nanoparticle. On the other hand, maximum negative optical damping, which causes cooling of the mechanical motion, is achieved in the sideband-resolved regime $\kappa \ll \omega_{\rm M}$, when $\Delta = -\omega_{\rm M}$. Insets are photographs of a captured nanoparticle inside the cavity (from [6]).

Let us derive the mean number of phonons due to the optical damping. The optical force PSD $S_{FF}^{\rm OPT}(-\omega) = \hbar^2 x_{\rm zpf}^2 g^2 S_{\hat{Y}_{\rm a}\hat{Y}_{\rm a}}(\omega)$. Neglecting mechanical interaction so that $g = 0$, from Eq. 2.60, we have:

$$S_{\hat{Y}_{\rm a}\hat{Y}_{\rm a}}(\omega) = \frac{\hbar^2}{x_{\rm zpf}^2}\frac{\kappa}{(\omega+\Delta)^2+\left(\frac{\kappa}{2}\right)^2} \tag{2.78}$$

where we have used the noise correlators in Eq. 2.46 and assumed RWA for the cavity mode. Substituting Eq. 2.78 in Eq. 2.24, we obtain:

$$\bar{n}^{\rm opt} = \frac{(\Delta - \omega_{\rm M})^2 + \kappa^2/4}{4\omega_{\rm M}\Delta} \tag{2.79}$$

From Eq. 2.24 and Eq. 2.77, and noting that the total force comes from the thermal bath and the cavity, we have:

$$\bar{n} = \frac{\bar{n}^{\rm th}\Gamma_{\rm M} + \bar{n}^{\rm opt}\Gamma_{\rm opt}}{\Gamma_{\rm M} + \Gamma_{\rm opt}}. \tag{2.80}$$

Far from the ground state, the effective final temperature is given by the formula:

$$T = T_i \frac{\Gamma_{\rm M}}{\Gamma_{\rm M} + \Gamma_{\rm opt}} \tag{2.81}$$

where $T_{\rm i}$ is the initial bath temperature. Initial optomechanical cooling experiments on microtoroids [25] and SiN nanobeams [2] involve cryogenic precooling, but for levitated experiments $T_{\rm i} = 300K$, and the cooling proceeds by pumping the pressure down.

For preparing a macroscopic quantum state, the temperature of the mechanical mode needs to be brought down to the ground state. This can be achieved optomechanically by setting $\Delta = -\omega_{\rm M}$. In the rotating wave approximation (RWA), we obtain: $\hat{H}_{\rm int} \approx g(\hat{a}\hat{b}^\dagger + \hat{a}^\dagger\hat{b})$, while neglecting the other off-resonant terms. Such a beam-splitter Hamiltonian facilitates a state transfer, where the destruction of one quanta in the mechanical oscillator leads to the creation of another in the cavity mode.

The cavity field changes the mechanical response function. Figure 2.10 emphasises the need to be in the resolved sideband regime $\kappa < \omega_{\rm M}$ to ensure that non-resonant scattering processes that lead to heating are much more suppressed [26, 27].

Analytically, sideband asymmetry can be seen by calculating the optical power spectrum:

$$\begin{aligned}
S_{Y_{\rm a}Y_{\rm a}}(\omega) &= \left\langle \hat{Y}_{\rm a}^\dagger(\omega)\hat{Y}_{\rm a}(-\omega)\right\rangle \\
&= \kappa\left[|\chi_{\rm C}(-\omega)|^2\left\langle \hat{a}_{\rm in}^\dagger(\omega)\hat{a}_{\rm in}(-\omega)\right\rangle + |\chi_{\rm O}(\omega)|^2\left\langle \hat{a}_{\rm in}(\omega)\hat{a}_{\rm in}^\dagger(-\omega)\right\rangle\right] \\
&+ \Gamma_{\rm M}\left[|\chi_{\rm M}(-\omega)|^2\left\langle \hat{b}_{\rm in}^\dagger(\omega)\hat{b}_{\rm in}(-\omega)\right\rangle + |\chi_{\rm M}(\omega)|^2\left\langle \hat{b}_{\rm in}(\omega)\hat{b}_{\rm in}^\dagger(-\omega)\right\rangle\right] \\
&= \kappa\left[|\chi_{\rm O}(-\omega)|^2\bar{n}_{\rm a} + |\chi_{\rm O}(\omega)|^2(\bar{n}_{\rm a}+1)\right] \\
&+ \Gamma_{\rm M}\left[|\chi_{\rm M}(-\omega)|^2\bar{n}_{\rm b} + |\chi_{\rm M}(\omega)|^2(\bar{n}_{\rm b}+1)\right]
\end{aligned} \tag{2.82}$$

where we have substituted Eqs. 2.60, 2.41, 2.42 to arrive at the last equality consisting of four terms multiplied by the occupation numbers. $S_{Y_{\rm a}Y_{\rm a}}(\omega)$ will have, in general, Lorentzian

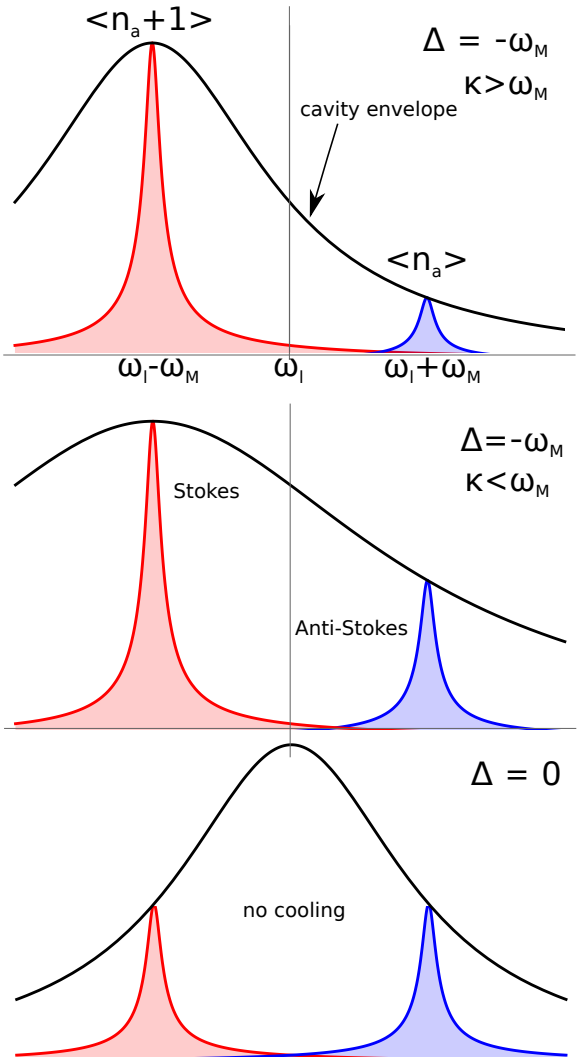

Figure 2.10: The cavity susceptibility function shapes the mechanical spectra. **(a)** Sideband asymmetry, which is a signature of ground state cooling is achieved in the sideband resolved regime $\kappa > \omega_{\mathrm{M}}$, when $\Delta = -\omega_{\mathrm{M}}$. **(b)** $\kappa < \omega_{\mathrm{M}}$ impairs the optomechanical cooling process although cooling has been shown to be possible in dissipatively coupled systems where $\kappa(\hat{x})$ [7] **(c)** $\Delta = 0$ yields a symmetric spectum for which there is no cooling.

peaks at $\pm\omega$ due to the prefactors $|\chi_{\mathrm{O}}(\mp\omega)|^2$. These peaks will be asymmetric, but for $\bar{n}_{\mathrm{a}} = 0$ (which is attainable for laser fields), one of them will be suppressed. Likewise, a pair of peaks will be found at $\pm\omega_{\mathrm{M}}$ due to $|\chi_{\mathrm{M}}(\mp\omega)|^2$. However, in the thermal regime, $\bar{n}_{\mathrm{b}} \gg \bar{n}_{\mathrm{a}} \gg 1$ so the last two terms will be dominant and result in a symmetric spectrum. As a final remark, the interpretation of sideband asymmetry is actually more nuanced: classical noise can lead to sideband asymmetry [71, 38], and depending on the detector model, the sideband asymmetry in the readout spectrum may be due to the position noise spectrum or optical interference terms [72].

2.5 Phase-sensitive optical detection of mechanical motion

The case $\Delta = 0$ in Eq. 2.75 is interesting as it leads to no change in the mechanical susceptibility even though the cavity is coupled to the mechanical mode. Nonetheless, the cavity provides a sensitive readout of the mechanical motion through its phase quadrature. The non-commutation of both the system and detector quadratures, however, follow the Heisenberg's uncertainty principle which sets a lower bound to measurement sensitivity. The objectives of this section are to derive the so-called standard quantum limit (SQL) first, for a free mass, and then for a continuous position measurement using a general linear response theory approach. Finally, we consider specifically displacement and force measurements in optomechanical systems.

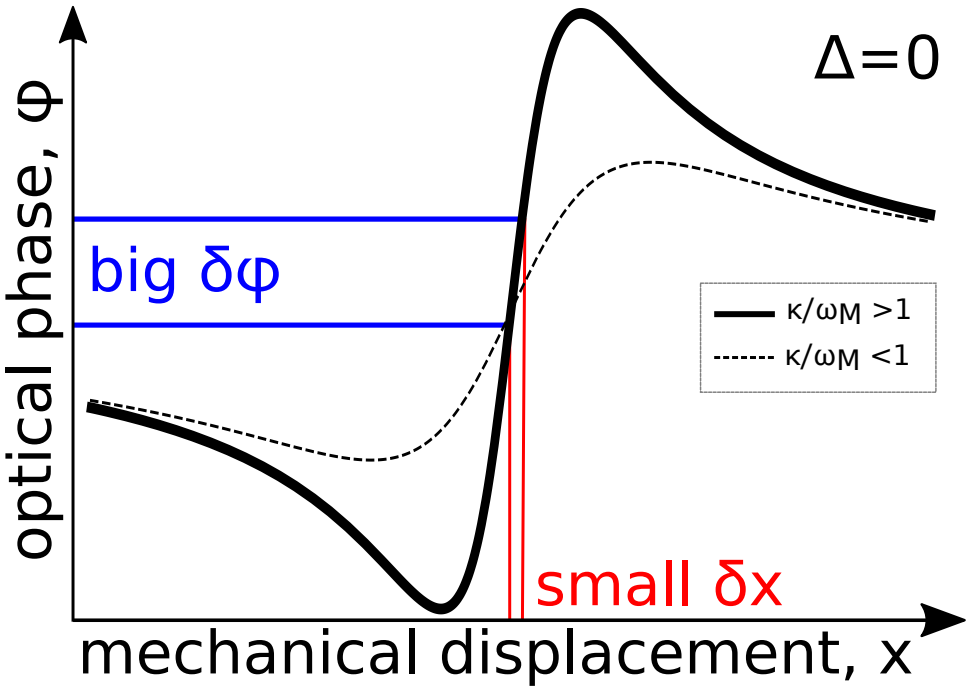

Figure 2.11: Imaginary part of the cavity susceptibility function (Eq. 2.63) describing the linear response of the cavity field phase quadrature to changes in mechanical position. At $\Delta = 0$, the cavity offers a built-in mechanical motion readout by transducing and amplifying displacements into phase shifts of the cavity output field, which can then be measured via homodyne detection. Small displacements around the equilibrium position yield bigger phase shifts as sideband resolution increases.

2.5.1 Free-mass limit

Even before considering the cavity detector mode, we already encounter a limit to sensitivity that is intrinsic to the quantum system being measured. A complete knowledge of the state of a free mass (mass, m) requires both its position and momentum. Being non-commuting variables, the Heisenberg's uncertainty principle sets a lower bound to the

product of their variances:

$$\sigma(\hat{x})\sigma(\hat{p}) \leq \frac{\hbar^2}{4}. \tag{2.83}$$

The lower bound is of the order 10^{-34} and is indeed very small. In the classical regime, it will easily be masked by thermal fluctuations, so will not be a significant effect; however, progress in optomechanical cooling has allowed such quantum noises to be observed in mechanical systems [19].

Note that a single-shot, projective measurement of the position can be made as arbitrarily precise as possible — it is *not* subject to Eq. 2.83. When consecutive position measurements are executed, however, the resulting momentum uncertainty from the first will contaminate the subsequent position measurement. To show this backaction effect, consider two measurements of $\hat{x}$ at $t = 0$ then at $t = \tau$ [3]:

$$\hat{x}(\tau) = \hat{x}(0) + \frac{\tau}{m}\hat{p}(0), \tag{2.84}$$

Taking the variances of both sides,

$$\begin{aligned} \sigma^2[\hat{x}(\tau)] &= \sigma^2\left[\hat{x}(0) + \frac{\tau}{m}\hat{p}(0)\right] \\ &= \sigma^2[\hat{x}(0)] + \left(\frac{\tau}{m}\right)^2\sigma^2[\hat{p}(0)] \\ &= \sigma^2[\hat{x}(0)] + \left(\frac{\hbar\tau}{2m}\right)^2\frac{1}{\sigma^2[\hat{x}(0)]} \end{aligned} \tag{2.85}$$

where we used Eq. 2.83 and made a crucial assumption that $\hat{x}(0)$ and $\hat{p}(0)$ do not become correlated after the first measurement. Note that $\sigma^2[\hat{x}(\tau)]$ depends on two competing contributions: the imprecision noise which depends linearly on $\sigma^2[\hat{x}(0)]$; and the backaction noise, which depends inversely on $\sigma^2[\hat{x}(0)]$. Finding the optimal balance between these noises results in the standard quantum limit (SQL) of position measurement. Differentiating the left-hand side with respect to $\sigma[\hat{x}(0)]$, we obtain:

$$\sigma^2_{\mathrm{SQL}}[\hat{x}(\tau)] = \frac{\hbar\tau}{m} \tag{2.86}$$

The SQL can be improved by choosing a bigger mass or a faster time interval between measurements.

2.5.2 Continuous position measurements

Let us generalise the results of Sec. 2.5.1 to the continuous case by considering many subsequent position measurements in the limit of $\tau \to 0$. We also consider the added noise of a quantum detector due to its non-commuting quadratures: $\left[\hat{I}, \hat{F}\right] = 1$ (we consider a

general detector; for an optical cavity, $\hat{I}$ and $\hat{F}$ are the amplitude and phase quadratures). Here, we follow the derivation in [22]. Given the signal $\hat{X}$ is coupled to the detector via $\hat{H}_{\rm int} = g\hat{X}\hat{F}$, linear response theory gives:

$$\left\langle \hat{I}(t) \right\rangle = \left\langle \hat{I}(0) \right\rangle + g \int_{-\infty}^{\infty} \mathrm{d}t' \, \chi_{IF}(t-t')\hat{X}(t') \tag{2.87}$$

where

$$\chi_{IF}(t) = -\frac{\mathrm{i}}{\hbar}\theta(t) \left\langle \left[\hat{I}(t), \hat{F}(0) \right] \right\rangle \tag{2.88}$$

is the susceptibility and $\theta(t)$ is the step function. For this reason, $\hat{F}$ and $\hat{I}$ are called the input and output ports of the detector, and can be identified with the amplitude and phase of the cavity, respectively. It will be useful for later derivations to consider the reverse process:

$$\left\langle \hat{F}(t) \right\rangle = \left\langle \hat{F}(0) \right\rangle + g \int_{-\infty}^{\infty} \mathrm{d}t' \, \chi_{FI}(t-t')\hat{X}(t') \tag{2.89}$$

where

$$\chi_{FI}(t) = -\frac{\mathrm{i}}{\hbar}\theta(t) \left\langle \left[\hat{F}(t), \hat{I}(0) \right] \right\rangle \tag{2.90}$$

is the reverse susceptibility. From Eq. 2.88 we see immediately that signal detection inevitably comes with quantum noise, as both results from the non-commutation of $\hat{I}$ and $\hat{F}$.

Interestingly, the SQL can easily be shown from the Cauchy-Schwarz inequality:

$$\begin{aligned} \left\langle \hat{I}, \hat{I} \right\rangle \left\langle \hat{F}, \hat{F} \right\rangle &\geq \left| \left\langle \hat{I}, \hat{F} \right\rangle \right|^2 \\ &\geq \left| \frac{1}{2} \left\{ \hat{I}, \hat{F} \right\} + \frac{1}{2} \left[\hat{I}, \hat{F} \right] \right|^2 \end{aligned} \tag{2.91}$$

from which the Heisenberg's uncertainty principle immediately follows. Usually $\left\{ \hat{I}, \hat{F} \right\}$ vanishes with the appropriate choice of eigenvectors (see [73]), leading to a more familiar form of the Heisenberg's uncertainty principle. The inner product $\langle \cdot, \cdot \rangle$ is defined over operators, and $\left\{ \hat{I}, \hat{F} \right\} \equiv \left\langle \hat{I}, \hat{F} \right\rangle + \left\langle \hat{F}, \hat{I} \right\rangle$ and $\left[\hat{I}, \hat{F} \right] \equiv \left\langle \hat{I}, \hat{F} \right\rangle - \left\langle \hat{F}, \hat{I} \right\rangle$. By choosing the symmetrised noise spectral density as the inner product:

$$\left\langle \hat{I}, \hat{F} \right\rangle \equiv \bar{S}_{IF}(\omega) = \frac{1}{2} \int_{-\infty}^{\infty} \mathrm{d}t \, \mathrm{e}^{\mathrm{i}\omega t} \left\{ \hat{I}(t), \hat{F}(0) \right\}, \tag{2.92}$$

Eq. 2.91 becomes

$$\bar{S}_{II}(\omega)\bar{S}_{FF}(\omega) \geq \frac{1}{4} \left| \bar{S}_{IF}(\omega) - \bar{S}_{FI}(\omega) \right|^2. \tag{2.93}$$

Our task now is to simplify the RHS of the inequality Eq. 2.93 using Eq. 2.92:

$$\begin{aligned}\bar{S}_{IF}(\omega) - \bar{S}_{FI}(\omega) &= \frac{1}{2}\int_{-\infty}^{\infty} \mathrm{d}t\, \mathrm{e}^{\mathrm{i}\omega t} \left\langle \left\{\hat{I}(t), \hat{F}(0)\right\} - \left\{\hat{F}(t), \hat{I}(0)\right\} \right\rangle \\ &= \frac{1}{2}[S_{IF}(\omega) - S_{IF}(-\omega)] + \frac{1}{2}[S_{FI}(\omega) - S_{FI}(-\omega)] \end{aligned} \tag{2.94}$$

We further note that by Eqs. 2.88 and 2.90:

$$\begin{aligned}\frac{1}{2}[S_{IF}(\omega) - S_{IF}(-\omega)] &= \mathrm{i}\hbar\chi_{IF}(\omega) \\ \frac{1}{2}[S_{FI}(\omega) - S_{FI}(-\omega)] &= -\mathrm{i}\hbar\chi_{FI}(\omega)^*, \end{aligned} \tag{2.95}$$

where we have used the property $\chi_{FI}(-\omega) = -\chi_{FI}(\omega)^*$. Finally, substituting Eq. 2.95 in Eq. 2.93, we obtain:

$$\bar{S}_{II}(\omega)\bar{S}_{FF}(\omega) \geq \frac{|\chi_{IF}(\omega) - \chi_{FI}(\omega)^*|^2}{4}. \tag{2.96}$$

Let us now examine more closely the importance of the reverse susceptibility. From Eq. 2.96, a detector with $\chi_{IF}(\omega) = \chi_{FI}(\omega)^*$ does not add any noise to the measurement. While this might seem ideal at first, such a detector in thermal equilibrium does not amplify the quantum signal, and so will be quite useless as a readout. The ideal detector is in fact, when $\chi_{FI}(\omega) = 0$, in which case, Eq. 2.96 simplifies to:

$$\bar{S}_{II}(\omega)\bar{S}_{FF}(\omega) \geq \frac{|\chi_{IF}(\omega)|^2}{4}. \tag{2.97}$$

For a more thorough discussion of quantum noise measurement and amplification, see [22].

2.5.3 Standard quantum limit

Let us now go back to the specific case of displacement detection in an optomechanical system. As mentioned earlier, $\Delta = 0$ allows the mechanical motion to be imprinted in the cavity phase. Using the input-output relation: $\hat{Y}_{\mathrm{p,out}} = \hat{Y}_{\mathrm{p,in}} - \sqrt{\kappa}\hat{Y}_{\mathrm{p}}$, and noting that $\eta(\omega) = 0$ in Eq. 2.61[1], the detected signal is:

$$\hat{Y}_{\mathrm{p,out}}(\omega) = \left[1 - \kappa\eta'(\omega)\right]\hat{Y}_{\mathrm{p,in}}(\omega) + \sqrt{\kappa}\eta'(\omega)2g\hat{X}(\omega). \tag{2.98}$$

Before we proceed to calculate the PSD, we first introduce an often quoted optomechanical parameter called the cooperativity $C \equiv 4g^2/(\kappa\Gamma_{\mathrm{M}})$, and define the effective cooperativity:

$$C_{\mathrm{eff}}(\omega) \equiv \frac{C}{(1 - 2\mathrm{i}\omega/\kappa)^2}. \tag{2.99}$$

[1] We have dropped the label "RWA".

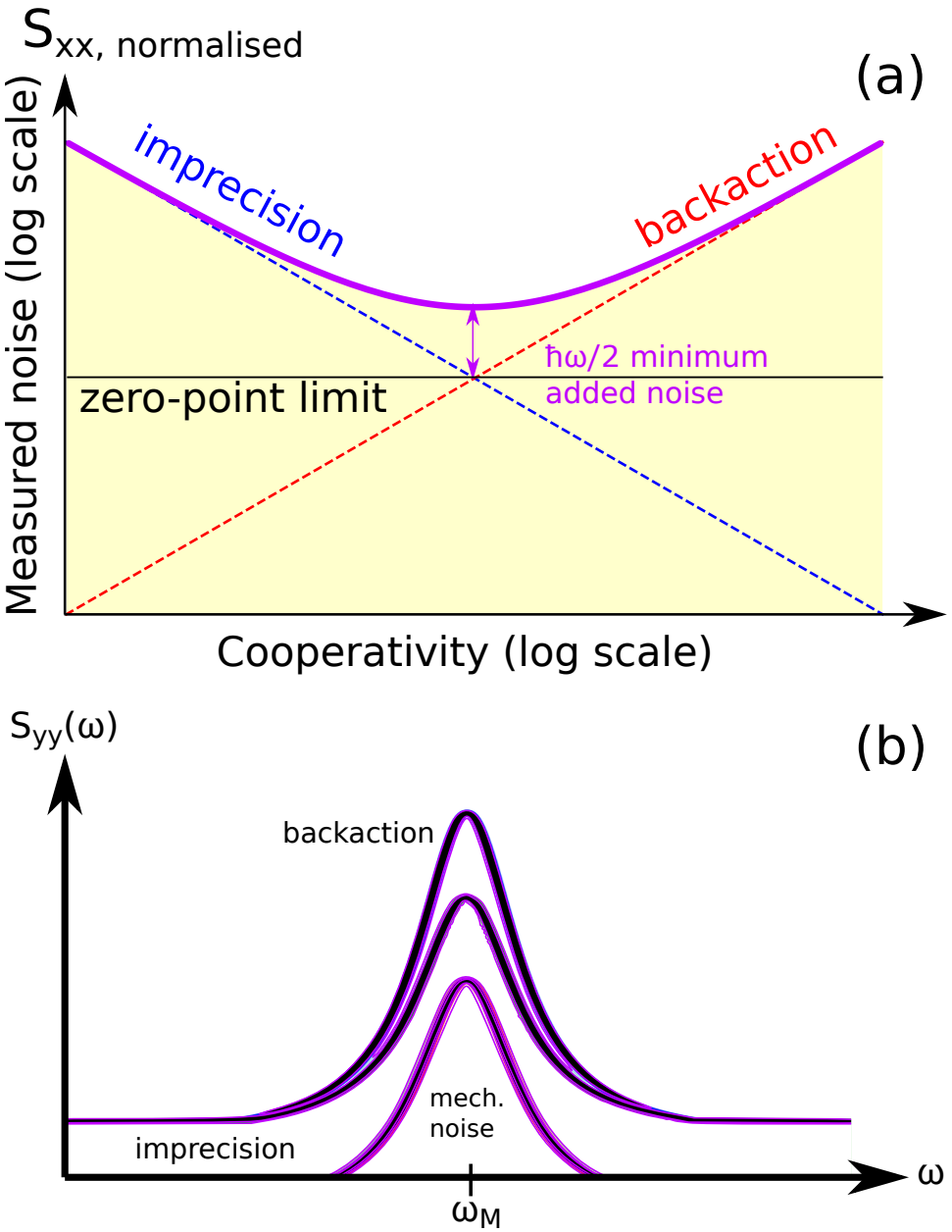

Figure 2.12: (**a**) Standard quantum limit (SQL) of displacement detection. On top of the intrinsic zero-point flucutations, the measured noise in $S_{xx}(\omega_{\rm M})$ also includes imprecision (blue) and backaction (red) contributions which have opposite dependence on cooperativity $C = 4g/(\kappa\Gamma_{\rm M})$. The sum of these optical noises (purple) adds a minimum of $\hbar\omega_{\rm M}/2$ at the optimal cooperativity (i.e., optimal input power), setting the so-called SQL. (**b**) The optical spectrum showing constributions from intrinsic mechanical noise, as well as the imprecision and backaction noises. The imprecision noise dominates at off-resonant frequencies while the backaction noise is strongest at $\omega_{\rm M}$ because of the mechanical susceptibility prefactor.

Experimentally, it is related to how strong the input laser power is with respect to the damping rates. While frequency-dependent, $C_{\rm eff}(\omega_{\rm M}) = C$ when $\kappa \ll \omega_{\rm M}$, i.e., when the cavity is sideband-resolved. We encountered this important regime in Sec. 2.4.

Going back to Eq. 2.98, the cavity output PSD is:

$$S_{Y_{\rm p}}^{\rm out}(\omega) = S_{Y_{\rm p,in}Y_{\rm p,in}}(\omega) + 4\Gamma_{\rm M}C_{\rm eff}S_{XX}(\omega), \tag{2.100}$$

where we have expressed the coefficient of $S_{XX}(\omega)$ in terms of the effective cooperativity[2]. Interestingly, $|1-\kappa\eta'(\omega)|^2 = 1$, and $S_{Y_{\mathrm{p,in}}Y_{\mathrm{p,in}}}(\omega) = \frac{1}{2}$ since $\bar{n}_{\mathrm{a}} = 0$ is typical for optical laser frequencies. $S_{XX}(\omega)$ then sits on top of a constant noise floor at half a quanta, which we identify as the imprecision noise (Fig. 2.12b).

From Eq. 2.100, it might seem that one just needs to increase $C_{\mathrm{eff}}(\omega)$ to improve the signal-to-noise ratio. However, a closer inspection of $\hat{X}(\omega)$ shows this is not the case. Noting that $\mu(\omega,\Delta) = \mu(\omega)$ at $\Delta = 0$, the mechanical noise PSD is:

$$S_{XX}(\omega) = S_{\mathrm{th}}(\omega) + 16\Gamma_{\mathrm{M}}C_{\mathrm{eff}}|\mu(\omega)|^2 S_{Y_{\mathrm{a,in}}Y_{\mathrm{a,in}}}(\omega). \tag{2.101}$$

The first term $S_{\mathrm{th}}(\omega) = 4\Gamma_{\mathrm{M}}|\mu(\omega)|^2(\bar{n}_{\mathrm{b}} + 1/2)$ is the mechanical noise, which is the signal that we want to measure. The second term is the optical backaction noise, which is the measurement-induced disturbance to the mechanical motion. Notice that it is also proportional to $C_{\mathrm{eff}}(\omega)$. Therefore, while increasing $C_{\mathrm{eff}}(\omega)$ amplifies the signal, it also inevitably comes with a noise penalty. Rewriting Eq. 2.100 in units of mechanical position, we obtain:

$$\frac{S^{\mathrm{out}}_{Y_{\mathrm{p}}}(\omega)}{4\Gamma_{\mathrm{M}}C_{\mathrm{eff}}}(\omega) = \frac{S_{Y_{\mathrm{p,in}}Y_{\mathrm{p,in}}}(\omega)}{4\Gamma_{\mathrm{M}}C_{\mathrm{eff}}}(\omega) + S_{\mathrm{th}}(\omega) + 4\Gamma_{\mathrm{M}}C_{\mathrm{eff}}(\omega)|\mu(\omega)|^2 S_{Y_{\mathrm{a,in}}Y_{\mathrm{a,in}}}(\omega). \tag{2.102}$$

In complete analogy with Secs. 2.5.1 and 2.5.2, we can identify two competing noise contributions to the detected signal, one that is inversely proportional to $C_{\mathrm{eff}}(\omega)$, which is the imprecision noise $S_{II}(\omega)$, and another that is linear in $C_{\mathrm{eff}}(\omega)$, which is the backaction noise $S_{FF}(\omega)$. Taking their products, we obtain:

$$S_{II}(\omega)S_{FF}(\omega) = \frac{|\mu(\omega)|^2}{4} \tag{2.103}$$

in complete agreement with Eq. 2.97. Again, we emphasise that such a limit exists because of the non-commutation of the cavity amplitude and phase bath noises. The experimental implication is that one needs to choose an optimal input power to optimise $C_{\mathrm{eff}}(\omega)$. Being frequency-dependent, one also needs to consider the frequencies and bandwidth the sensor is designed for. For on-resonance sensing, it can be shown that the minimum added noise is $\frac{1}{2}\hbar\omega_{\mathrm{M}}$, on top of the intrinsic zero-point and thermal motion of the mechanical oscillator (see Fig. 2.12).

[2]It is easy to show that $4\Gamma C_{\mathrm{eff}} = 4g^2\kappa|\eta'(\omega)|^2$ at $\Delta = 0$.

2.6 Beyond the standard quantum limit

In summary, the origin of the SQL is in the non-commutation of the observable with the Hamiltonian. For example, measuring the position $\hat{X}$ via the cavity phase shift $\hat{Y}_{\mathrm{p}}$ given Eq. 2.36 leads to at least a quantum of noise in the output cavity phase PSD. The consequence is that the observable does not commute with itself at different times, leading to constraints Eqs. 2.83 and 2.97.

Circumventing the SQL then means choosing the interaction Hamiltonian wisely so the observable $\hat{O}$ satisfies: $\left[\hat{O}(t_1), \hat{O}(t_2)\right] = 0$ for any times t_1, t_2. Measurements of such $\hat{O}$ are called quantum non-demolition (QND) measurements [74], and in this section, we will briefly discuss two QND observables which are constants of motion with respect to the optomechanical Hamiltonian: namely, $\hat{X}^2$ and one of the rotating-frame quadratures of $\hat{X}$. The latter is commonly referred to as back-action evasion.

Finally, we also discuss optomechanically mediated squeezing (otherwise known as ponderomotive squeezing) to bring down the noise in the optical detector mode to below the imprecision noise floor for a certain bandwidth around resonance, thus improving the sensitivity beyond the SQL.

2.6.1 Quadratic coupling

The Hamiltonian of the mechanical oscillator can be cast in terms of the number operator: $\hat{H} = \hbar\omega_{\mathrm{M}}\left(\hat{N} + \frac{1}{2}\right)$. An interaction of the form $\hat{X}^2\hat{F}$ constitutes a QND measurement because $\hat{X}^2 = \left(\hat{b}^\dagger + \hat{b}\right)^2 \approx \hat{N}$ under RWA. This is valid for high Q cavities, where the slow decay rate allows off-resonant terms $\hat{b}\hat{b}$ and $\hat{b}^\dagger\hat{b}^\dagger$ to average out throughout many oscillation periods.

Quadratic coupling allows a QND detection of the mechanical oscillator energy. One could then in principle observe mechanical Fock states and show quantum jumps in the oscillator energy. Quadratic potentials also act as an effective double-slit for interferometry of macroscopic superposition states [48]. In Chapter 3, we show evidence of quadratic coupling in our hybrid electro-optical trap set-up.

2.6.2 Back-action evasion

Let us write the mechanical motion in terms of rotating frame quadratures: $\hat{X}(t) = \hat{X}_1(t)\cos\omega_{\mathrm{M}}t + \hat{X}_2(t)\sin\omega_{\mathrm{M}}t$. The problem with having $\hat{H} = g\hat{X}\hat{F}$ is we are measuring both quadratures $\hat{X}_1$ and $\hat{X}_2$ at the same time, thereby introducing backaction noise to $\hat{X}$ at a later time.

One way to realise single-quadrature detection is to have a modulated optomechanical coupling so that $\hat{H}_{\rm int} = g\cos\omega_{\rm M}t\hat{X}\hat{F} = g\Big[\hat{X}_1(t)(1+\cos 2\omega_{\rm M}) + \hat{X}_2\sin\omega_{\rm M}t\Big]$. Choosing a measurement period $\tau \gg (2\omega_{\rm M})^{-1}$ averages out the time-dependent terms leaving us with a measurement of $\hat{X}_1$. For more details on back-action evasion measurements, see [60]. In this thesis, we will consider modulations not only in g but also in $\omega_{\rm M}$, and show backaction noise can be evaded, at least for a narrowband of frequencies around mechanical resonance.

2.6.3 Ponderomotive squeezing

Optical squeezed states has been one of the cornerstones of quantum optics, where one quadrature achieves an uncertainty below the minimum required by the Heisenberg's uncertainty principle, at the expense of gaining more noise in the conjugate quadrature. Experimentally, optical squeezing can be achieved through a Kerr nonlinearity described by an interaction term $\propto \left(\hat{a}^\dagger\hat{a}\right)$.

The coherent interaction between light and mechanics allows for the phonon field to be an effective Kerr nonlinear medium, leading to optomechanical squeezing. Note that here we consider only single-mode optical squeezed states at $\Delta = 0$, which is quite different from the two-mode squeezing/optomechanical entanglement regime at $\Delta = +\omega_{\rm M}$. The latter causes instabilities while the former is compatible with optomechanical cooling.

Because mechanical modes are typically high-Q, ponderomotive squeezing happens only at a narrow band of frequencies centered at $\omega_{\rm M}$. However, squeezed regions can be observed for $-\omega_{\rm M} < \omega < \omega_{\rm M}$ through homodyne detection of the cavity output. Homodyne detection combines the signal with a strong reference beam, called the local oscillator (LO), to achieve a phase-sensitive detection (see Appendix C for a discussion of linear detection methods).

In frequency space the homodyne signal:

$$\begin{aligned} S^{\rm hom}(\omega) &= \left|\hat{Y}_{\rm a,out}(\omega)\right|^2\cos^2\theta + \left|\hat{Y}_{\rm p,out}(\omega)\right|^2\sin^2\theta \\ &+ 2\cos\theta\sin\theta\left(\hat{Y}_{\rm a,out}(\omega)\hat{Y}_{\rm p,out}(\omega) + \hat{Y}_{\rm p,out}(\omega)\hat{Y}_{\rm a,out}(\omega)\right), \end{aligned} \tag{2.104}$$

where θ is the LO phase, and $\hat{Y}_{\rm a,out}(\hat{Y}_{\rm p,out})$ is the amplitude (phase) of the cavity output field. As we have seen from Eq. 2.104, at $\Delta = 0$, $\left|\hat{Y}_{\rm a,out}(\omega)\right|^2$ results in an imprecision noise floor, while $\left|\hat{Y}_{\rm p,out}(\omega)\right|^2$ results in backaction and thermal peaks at $\pm\omega_{\rm M}$, which tends to the noise floor at far off-resonance. Hence, squeezing must come from the cross-correlation term.

In terms of the ladder operators:

$$\mathrm{i}\left(\hat{Y}_{\rm a,out}(\omega)\hat{Y}_{\rm p,out}(\omega) + \hat{Y}_{\rm a,out}(\omega)\hat{Y}_{\rm p,out}(\omega)\right) = 2\left(\hat{a}^\dagger_{\rm out}\hat{a}^\dagger_{\rm out} + \hat{a}_{\rm out}\hat{a}_{\rm out}\right). \tag{2.105}$$

The terms have opposite phases, and together with the correct θ, will result in a negative value that will bring the noise below the imprecision floor. However, at $\omega = \pm\omega_{\mathrm{M}}$, the cross-spectra is zero regardless of θ, resulting in large backaction noises on resonance. Introducing modulations in the system, or changing the detection method can reveal squeezing on-resonance [75, 9].

3 | Hybrid trap model

This chapter analyses the classical dynamics of a levitated nanoparticle inside an optical cavity combined with a Paul trap. In Sec. 3.1, the origin of optomechanical coupling in levitated systems is explained through the gradient forces that trap the nanoparticle at one of the antinodes of the cavity standing wave. The mechanical frequency as a function of the mean intracavity intensity is also derived. In Sec. 3.2, the conditions for trapping in the quadrupole field of a Paul trap are discussed, and the characteristic secular frequencies as a function of the stability parameters are calculated. Finally, in Section 3.3, an analytical model is developed describing the particle dynamics in the combined cavity and Paul trap fields. Specifically, the optomechanical cooling rate is calculated, as well as the mechanical and secular frequency shifts that result from the two-way interaction between the optical cavity and the Paul trap.

3.1 Gradient forces in an optical cavity

A hybrid electro-optical trap consists of an optical cavity and a Paul trap mounted inside a vacuum chamber. The TEM_{00} mode of a laser (wavelength λ) drives the optical cavity (frequency ω_c) to create a standing wave potential across the axial direction x. To reduce losses due to misalignment, the cavity mirrors were chosen to have plano-concave geometry defined by two parameters: the radius of curvature $r_\mathrm{c} \approx 25$ mm and the cavity length $L \approx 13$ mm. So long as $r_\mathrm{c} > L$, the beam focuses at the cavity center with a waist $w^2 = \frac{\omega_\mathrm{l}}{2\pi}\sqrt{L(2r_\mathrm{c} - L)}$. Given the experimental parameters in Table 4.1 (found at the end of Chapter 2), this gives $w \approx 60\mu$m. We assume magnetic forces have negligible effect on the dynamics and the cavity frequency ω_c is much higher than any other frequencies in the system, so RWA may be applied [76]. The electric field intensity inside the cavity is then:

$$|E(x,y,z)|^2 = \frac{\hbar\omega_\mathrm{c}}{\epsilon_0 V_\mathrm{c}}|a|^2\cos^2(kx)\mathcal{F}(y,z) \tag{3.1}$$

where $|a|^2$ is the intracavity photon number, $V_\mathrm{c} = \pi w^2 L$ is the mode volume, and the intensity profile in the transverse directions is Gaussian: $\mathcal{F}(y,z) = \exp\left[-2(y^2+z^2)/w^2\right]$.

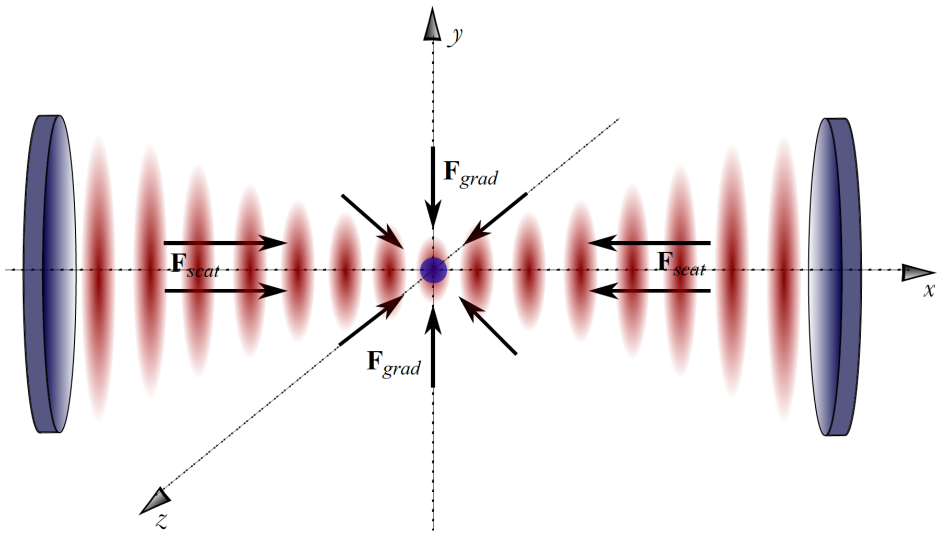

Figure 3.1: Gradient and scattering forces inside an optical cavity. The opposing F_{scat} due to the mirrors' configuration, and the F_{grad} allow three-dimensional trapping of the dielectric nanoparticle at one of the optical wells of the standing wave potential. Image adapted from [6].

200-nm silica particles (radius $r \ll \lambda$, density ρ, relative permittivity ϵ_{r}) are caught in one of the optical wells in the cavity standing wave potential. A master equation approach [77] can be used to calculate accurately the polarisation response that underpins optomechanical interaction for arbitrary dielectrics. However, the subwavelength dimension allows us to model the particle as a point dipole with a polarisation $P(\mathbf{r})$. In an inhomogeneous electric field such as Eq. 3.1, a point dipole experiences a radiation pressure force towards the highest intensity gradient. This allows three-dimensional trapping of the particle around the beam waist, at the antinode of the cavity standing wave. The potential energy of such a system is given by

$$V_{\mathrm{opt}} = -\frac{1}{2}\int_{V_{\mathrm{s}}} \mathrm{d}^3\mathbf{r}\, P(\mathbf{r})E(\mathbf{r}), \tag{3.2}$$

where the integration is made over the volume V_{s} of the sphere.

To linear order, the polarisation for a homogeneous dielectric is:

$$P(\mathbf{r}) = \alpha E(\mathbf{r}), \tag{3.3}$$

such that the electric field intensity $|E(\mathbf{r})|^2$ is scaled by the polarisability α: $\alpha|E(\mathbf{r})|^2$. The effective change in both the amplitude and phase of the intracavity field $E(\mathbf{r})$ due to the polarisation response $P(\mathbf{r})$ is the key to understanding the origin of optomechanical coupling in levitated set-ups. For the canonical system discussed in Sec. 2.3, the definition of the optomechanical coupling G as $\partial\omega_{\mathrm{c}}/\partial x$ is easy to visualise because the change in length δL resulting from the oscillations of the end-mirror directly translates to a shift

in the cavity resonance $\delta\omega_c$, as $\omega_c(L)$. In levitated systems, however, the cavity length is fixed, so connecting the particle's motion to $\delta\omega_c$ may not be obvious. However, the particle's polarisation causes a phase and amplitude change in $E(\mathbf{r})$ which can be seen as shifting the nodes of standing wave either towards or away from resonance, thus creating a (dispersive) optomechanical coupling.

Substituting the Clausius-Mossotti relation $\alpha = 3\epsilon_0 \frac{\epsilon_r - 1}{\epsilon_r - 2}$ in Eq. 3.3, and using Eq. 3.1, Eq. 3.2 simplifies to

$$V_{\text{opt}} = -\hbar A |a|^2 \cos^2(kx)\mathcal{F}(y,z), \tag{3.4}$$

where the coupling strength

$$A = \frac{3V_s}{2V_c}\frac{\epsilon_r - 1}{\epsilon_r - 2}\omega_c. \tag{3.5}$$

Fluctuations in x will cause fluctuations in $a \to |\bar{\alpha}| + a$, with $|\bar{\alpha}|$ being the mean intracavity photon number. This provides a harmonic potential for the particle which oscillates with a mechanical frequency:

$$\overline{\omega}_M^2 = \frac{2\hbar k^2 A |\bar{\alpha}|^2}{m}, \tag{3.6}$$

for oscillations about the antinode $x_0 = 0$. Indeed, one of the key features of optically levitated systems is the laser-tuneable $\overline{\omega}_M$.

3.2 Stability parameters of a Paul trap

A Paul trap is a device that can trap and manipulate ions by virtue of its oscillating electric field, and has found a wide application in ion mass spectrometry. In our experiment, we employ specifically a quadrupole ion trap (as opposed to linear traps) for trapping silica spheres (charge Q, mass m) at high vacuum. Quadrupole fields are produced by applying a voltage ϕ_0 to the ring (radius r_0) and endcap electrodes. The result is a parabolic potential energy well in the x, y, and z directions that tend to restore the particle to the trap center:

$$V_{\text{ion}}(x,y,z) = \frac{Q\phi_0}{r_0^2}(c_x x^2 + c_y y^2 + c_z z^2). \tag{3.7}$$

Imposing the Laplace equation $\nabla^2 V_{\text{ion}} = 0$, the coefficients must satisfy: $c_x = c_y = 1$ and $c_z = -2$. Clearly, this implies that the particle will be unstable in one direction. The key idea that won Wolfgang Paul the Nobel Prize in 1989 is to consider a time-dependent potential: $\phi_0 = U_0 + V_0 \sin\omega_d t$, where $U_0(V_0)$ is the DC(AC) voltage applied to

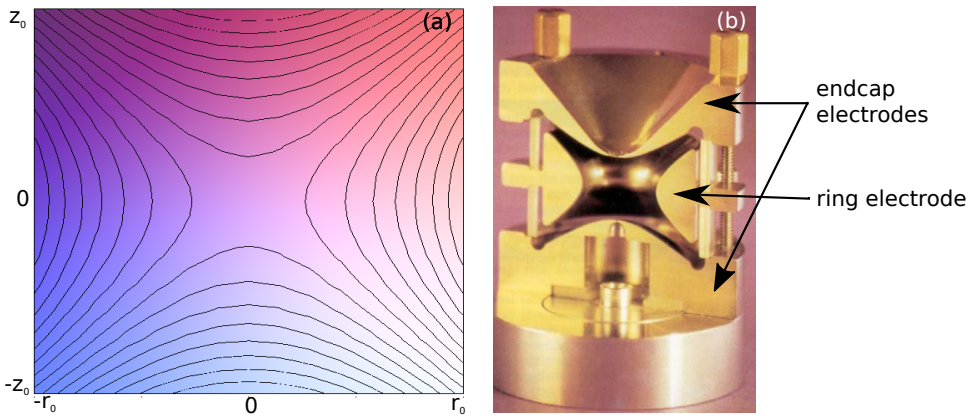

Figure 3.2: **(a)** Equipotential lines in the plane spanned by the radial (r) and transverse (z) directions, arising from the quadrupole fields of the Paul trap. The particle is trapped at (0,0) which becomes a stable region upon modulation of driving field. **(b)** Photograph of a quadrupole ion trap consisting of two endcap hyperbolic electrodes and ring electrode where an AC voltage is applied. Figure **(b)** adapted from [8].

the electrodes and $\omega_{\rm d}$ is the drive frequency. Assuming $U_0 = 0$, Eq. 3.7 becomes:

$$V_{\rm ion}(x, y, z, t) = \frac{QV_0}{r_0^2}(x^2 + y^2 - 2z^2)\sin\omega_{\rm d}t. \tag{3.8}$$

The force $F_u = \partial V_{\rm ion}/\partial u$ yields the equation of motion for each degree of freedom $u \in x, y, z$:

$$\ddot{u} = \frac{\omega_{\rm d}}{4}\left[a_u - 2q_u \sin\omega_{\rm d}t\right] u \tag{3.9}$$

which has the form of a Mathieu equation. Stable trajectories follow a Lissajous curve, and the value of the charge Q, trap radius r_0, and AC (DC) voltage V_0 (U_0) are constrained by the stability parameters a_u and q_u:

$$a_{x,y} = 8QU_0/(m\omega_{\rm d}^2 r_0^2), \text{ with } a_z = -a_x \tag{3.10}$$

$$q_{x,y} = 4QV_0/(m\omega_{\rm d}^2 r_0^2), \text{ with } q_z = -2q_x \tag{3.11}$$

The entire stability region can be mapped out in the $q - a$ parameter space by solving the Mathieu equations and is shown in Fig. 3.3b.

Assuming $U_0 = 0$, instability happens for $q_u \gtrsim 0.91$. Conversely, for $q_u \lesssim 0.2$ the motion is not only stable but also adiabatically separable into a fast micromotion at the drive frequency $\omega_{\rm d}$ and a slow secular frequency:

$$\omega_{\rm s}^u \simeq \frac{\omega_{\rm d}}{2\sqrt{2}} q_u. \tag{3.12}$$

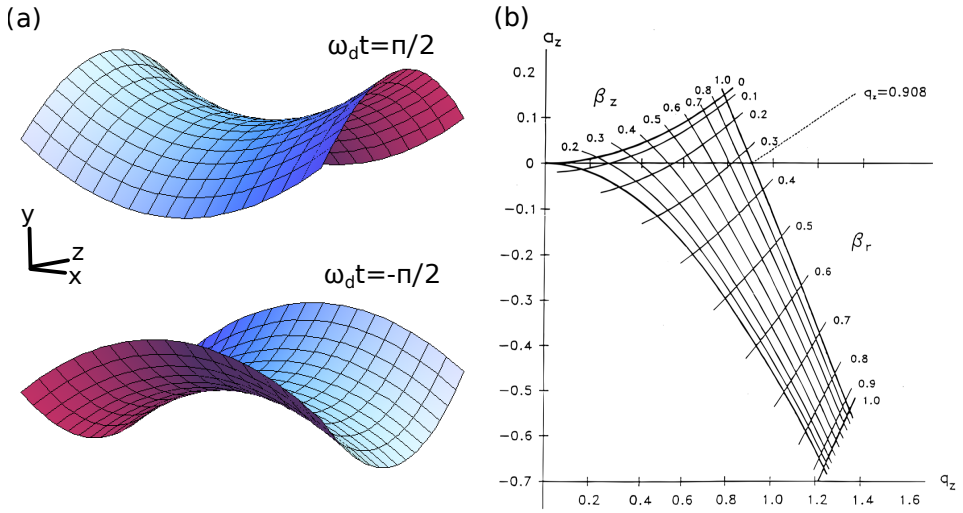

Figure 3.3: **(a)** Saddle-like potential of the Paul trap periodically changes orientation to create a stable region at the center of the trap. **(b)** The stability region is mapped out by the parameters a and q which, for fixed material and trap specifications, depends on the DC and AC voltages applied on the electrodes. Figure **(b)** adapted from [8].

3.3 Hybrid trap dynamics

Gradient forces trap a dielectric particle in one of the optical wells N of the cavity standing wave potential (see Fig. 3.4), where it oscillates about the antinode with a mechanical frequency given by Eq. 3.6. The time-harmonic quadrupole field of a Paul trap periodically pulls the particle away from the antinode at a rate $\omega_{\mathrm{d}} \ll \overline{\omega}_{\mathrm{M}}$. Therefore, on top of fast mechanical oscillations, the equilibrium position of the particle also does a slow excursion across a fraction of the optical well, with an amplitude that depends on N, as illustrated in Figure 3.4.

In the following, we derive the modifications to the optomechanical parameters $\Delta(x_0)$, $g(x_0)$, and $\omega_{\mathrm{M}}(x_0)$ as a result of $x_0(N,t)$. We also calculate the time-averaged optomechanical cooling rate to model the N-dependent cooling dynamics observed in the hybrid trap experiment (Chapter 4). Finally, we derive the mechanical and secular frequency shifts, showing the hybrid interaction between the cavity and the Paul trap.

3.3.1 Modifications to optomechanical parameters

We begin with the combined interaction potential of a particle in a hybrid electro-optical trap given by the sum of Eqs. 3.4 and 3.8:

$$V_{\mathrm{int}}(x,y,z,t) = -\hbar A|a|^2\cos^2(kx)\mathcal{F}(y,z) + \frac{1}{2}m\omega_{\mathrm{T}}^2(x^2+y^2-2z^2)\sin\omega_{\mathrm{d}}t, \tag{3.13}$$

where we have defined the ion trap frequency $\omega_{\mathrm{T}}^2 \equiv \frac{2QV_0}{mr_0^2}$. The full Hamitonian includes the bare cavity terms (in rotating frame): $\Delta|a|^2$, where Δ is the detuning, as well as the

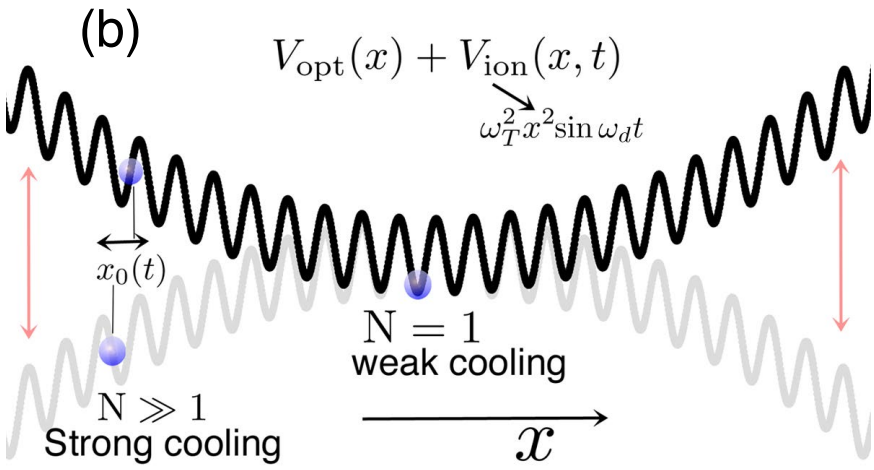

Figure 3.4: **(a)** Axial dynamics: a nanoparticle trapped in a single optical well of the optical potential of the cavity oscillates with a frequency $\omega_{\rm M}$ about an equilibrium point x_0. However, because of the oscillating ion trap field, the position of the equilibrium point itself oscillates slowly with time $x_0 \equiv x_0(t) = X_{\rm d}\sin\omega_{\rm d}t$. Linearised analysis is still possible since $\omega_{\rm d} \ll \omega_{\rm M}$, so these motions are separable. The dynamics depend on which well N the particle is captured, since the amplitude of the oscillation in the equlibrium point, $X_{\rm d} \propto N$, depends on N. Small $N \simeq 1$ corresponds to a negligible effect on x_0 and weak cooling. In contrast, higher N corresponds to a larger amplitude oscillation in x_0 and strong cooling. Another effect of the $x_0(t)$ oscillation is to slightly modulate the mechanical frequency $\omega_{\rm M}(t) \simeq \bar{\omega}_{\rm M} + 2\omega_2\cos 2\omega_{\rm d}t$, as well as the optomechanical coupling $g(t) = 2\bar{g}\sin\omega_{\rm d}t$. As a result, the intracavity spectrum $S_{\rm yy}(\omega)$ has a very different shape from the mechanical displacement spectrum $S_{\rm xx}(\omega)$. In the present work we investigate the N-dependence of the mechanical frequency and the optomechanical cooling. A key motivation is to examine the usual assumptions which underline optomechanical thermometry, and whether the temperature of a particle in this hybrid trap may be accurately inferred from the sidebands of the cavity output spectrum. Figure and caption adapted from [9].

kinetic energies of the particle in x, y, z.

As the cooling dynamics occur primarily in the axial direction, we assume $\mathcal{F}(y,z) \sim 1$ and solve the equation of motion for x:

$$\ddot{x} = -\frac{\hbar k A}{m}|a(t)|^2\sin(2kx) - \omega_{\rm T}^2 x\sin\omega_{\rm d}t \tag{3.14}$$

We linearise about the mean values: $a \to |\bar{\alpha}| + a$ and $x \to x_0 + x$, then shift the origin to the antinode of the optical well: $x_0 \to x_N + x_0$ where $x_N = N\lambda/2 = N\pi/k$ (see Fig. 3.4). Note the abuse of notation: from this point onwards, a and x denote the (small) fluctuating part of the complex field. To zeroth-order, $\ddot{x}_0 = 0$ gives:

$$\sin 2kx_0(N,t) = 2kX_{\rm d}\sin\omega_{\rm d}t, \text{ with } 2kX_{\rm d} = -\frac{\omega_{\rm T}^2}{\bar{\omega}_{\rm M}^2}2\pi N, \tag{3.15}$$

For small $x_0(t)$, the excursion in the equilibrium position is time-harmonic.

Using the small-angle aproximation: $\sin(2kx) \approx \sin(2kx_0)(1 + 4k^2x^2) + 2kx\cos(2kx_0)$,

we obtain, to first-order of Eq. 3.14:

$$\ddot{x} = \overline{\omega}_{\mathrm{M}}^2 \cos(2kx_0)x - \frac{\hbar|\bar{\alpha}|}{m}(a + a^*)(G_1 + G_2 x) \tag{3.16}$$

where the mechanical frequency, linear coupling, and quadratic coupling are given by:

$$\omega_{\mathrm{M}} = \overline{\omega}_{\mathrm{M}} \cos(2kx_0) \tag{3.17}$$

$$G_1 = kA \sin(2kx_0) \tag{3.18}$$

$$G_2 = k^2 A \cos(2kx_0). \tag{3.19}$$

Apart from this, the cavity acquires an effective detuning:

$$\Delta(x_0) = \Delta + A \cos^2(kx_0). \tag{3.20}$$

Let us pause for a moment to make sense of Eqs. 3.17 - 3.20. At $x_0 = 0$ where the potential is quadratic, ω_{M} is maximum, and decreases as the particle samples the linear part of the well. Having $R \ll \lambda$, the particle sees the intensity variation within the optical well and polarises accordingly, leading to an effective change in ω_{c} as explained in Sec. 3.1. Hence, the detuning shifts according to Eq. 3.20, and the particle experiences simultaneous linear and quadratic optomechanical coupling, with relative strengths depending on x_0. Unlike G_2, G_1 heavily depends on the Paul trap bringing the particle to the linear part of the well where $\sin(2kx_0)$ is large. Even without the Paul trap, gradient forces will cause the particle to settle at the antinode where G_2 is largest.

3.3.2 N-dependent cooling rate

While quadratic cooling is possible [78], single-photon quadratic couplings are notoriously weak due to the x_{zpf}^2 scaling factor. Hence, we rely on the linear coupling $g = x_{\mathrm{zpf}}\bar{\alpha}G_1$ for cooling. Substitution of Eq. 3.15 in Eq. 3.18 gives a time-dependent optomechanical coupling:

$$g(N, t) = 2\bar{g}(N) \sin \omega_{\mathrm{d}} t, \tag{3.21}$$

which fluctuates around an N-dependent mean:

$$\bar{g}(N) = \frac{\omega_{\mathrm{T}}^2}{\overline{\omega}_{\mathrm{M}}(0)^2} \pi k A x_{\mathrm{zpf}} |\bar{\alpha}| N. \tag{3.22}$$

Meanwhile, we square Eq. 3.15 and Eq. 3.17, add them, and then solve for $\omega_{\mathrm{M}}(t)$:

$$\omega_{\mathrm{M}}(t) = \overline{\omega}_{\mathrm{M}}(0)\left(1 - (2kX_{\mathrm{d}})^2 \sin^2 \omega_{\mathrm{d}} t\right)^{1/4}. \tag{3.23}$$

Expanding up to second order in ζ, we obtain:

$$\omega_{\mathrm{M}}(N,t) \approx \overline{\omega}_{\mathrm{M}}(N) + 2\omega_2(N)\cos 2\omega_{\mathrm{d}} t, \tag{3.24}$$

where

$$\overline{\omega}_{\mathrm{M}}(N) \approx \left(1 - \zeta N^2 - \frac{9}{4}\zeta^2 N^4\right)\overline{\omega}_{\mathrm{M}}(0) \tag{3.25}$$

$$\omega_2(N) \approx \frac{1}{2}\left(\zeta N^2 + 3\zeta^2 N^4\right)\overline{\omega}_{\mathrm{M}}(0), \text{ with } \zeta = \frac{\pi^2}{2}\frac{\omega_{\mathrm{T}}^4}{\overline{\omega}_{\mathrm{M}}^4(0)}. \tag{3.26}$$

Recall from Eq. 2.77 that the cooling rate depends on κ, as well as $\omega_{\mathrm{M}}(x_0)$, $g(x_0)$, and $\Delta(x_0)$. With $x_0 = x_0(N,t)$, we then expect a time-dependent (linear) cooling rate that varies cyclically, reaching a maximum when the bead is at the linear region of the optical well. Knowing that g, ω_{M}, and Δ have N-dependent average values, we use Eq. 3.22, Eq. 3.25, and $\bar{\Delta} = \Delta(x_0 = 0)$ to get the time-averaged optomechanical cooling rate:

$$\Gamma_{\mathrm{opt}}(N) = 4\bar{g}^2\kappa[S(\overline{\omega}_{\mathrm{M}}) - S(-\overline{\omega}_{\mathrm{M}})], \tag{3.27}$$

with $S(\omega) \equiv \left[(\bar{\Delta} + \omega)^2 + \frac{\kappa^2}{4}\right]^{-1}$. An effective temperature can then be obtained (see Eq. 2.81):

$$T \simeq 300K\,\frac{\Gamma_{\mathrm{M}}}{\Gamma_{\mathrm{opt}}(N) + \Gamma_{\mathrm{M}}}. \tag{3.28}$$

3.3.3 Cavity-shifted secular frequencies

In the previous sections, we derived the mechanical frequency that the particle oscillates with at the antinode. We also derived the secular frequency that characterises motion in a Paul trap as a function of the stability parameters. The hybrid nature of the electro-optical trap manifests in the cavity-shifted secular frequencies that result from the interaction of the cavity with the Paul trap.

Comparing Eq. 3.14 with Eq. 3.9, we obtain an effective a-stability parameter due to the presence of the cavity field: $a_x = 16\hbar A|\alpha|^2/(mw^2\omega_{\mathrm{d}}^2)$. Hence, the mean intracavity photons acts as an effective DC field which shifts the secular frequency:

$$\omega_{\mathrm{s}}^u \simeq \frac{\omega_{\mathrm{d}}}{2}\sqrt{a_u + q_u^2/2}, \tag{3.29}$$

This and Eq. 3.24 underline the non-trivial, two-way interaction between the cavity and the Paul trap: the mechanical frequency is shifted and modulated by the Paul trap, while the secular frequencies of the Paul trap acquire a "cavity-shift" from the optical field. The cavity-shifted secular frequencies will prove to be useful in inferring experimental parameters, as will be shown in the next chapter.

4 | Experimental results

Presented in this chapter are the main experimental results of the hybrid trap experiment as published in [10]. The laser detection system and the hybrid trap apparatus are described in Secs. 4.1 and 4.2. In Sec. 4.3, three data sets are presented which show quadratic coupling, transient cooling, and strong cavity cooling in the hybrid trap experiment. Only the details relevant to modelling and simulation of the system are covered in this chapter; for a more thorough discussion of the experiment, see [6].

4.1 Laser detection system

Figure 4.1 is a schematic diagram of the laser set-up used for the hybrid trap experiment. Light from 1064 nm Nd:YAG laser is directed via an isolator to a 90:10 beam-splitter (BS) to create two beams for cooling and cavity locking.[1]

The weak beam, fixed at 0.2mW, is phase-modulated at 26.6 ± 0.2 MHz via an electro-optic modulator (EOM). The amplitude-modulated beam reflected from the cavity is measured at PD_1 and enters the Pound-Drever Hall (PDH) system[2], which outputs a DC error signal that is fed to the PID controller for laser frequency stabilisation.

Meanwhile, the strong cooling beam passes through two cascaded acousto-optic modulators (AOM) to control its detuning from 0 to -200 kHz with respect to cavity resonance. The choice of AOM drivers (2 output function generator) has been crucial to ensuring frequency stability of the cooling beam to avoid particle loss [6]. To adjust the power within the range of a few μW to $\approx$ 500mW, a combination of a half-waveplate ($\lambda/2$) and a polarising beam splitter (PBS_2) is used. The series of lenses leading to the cavity ports are designed to control the diameter and phase front curvature of the TEM_{00} (Gaussian) mode for optimal mode-matching. The transmitted cooling beam is orthogonally polarised and is separated at PBS_1 to avoid interference with the reflected weak locking beam. The

[1] Fluctuations in the cavity length due to absorption heating, acoustic vibrations, mechanical stress, electronic noise, etc. can drive the laser in and out of resonance. It is important that the laser remains on-resonant/locked with the cavity to avoid trapping instability and measurement noise.

[2] The PDH is a laser frequency stabilisation technique which uses phase-modulated light to measure the intensity response of the reflected light from the cavity. The magnitude of the resulting intensity fluctuation indicates how far the laser is from resonance, and can then be used for feedback control [79].

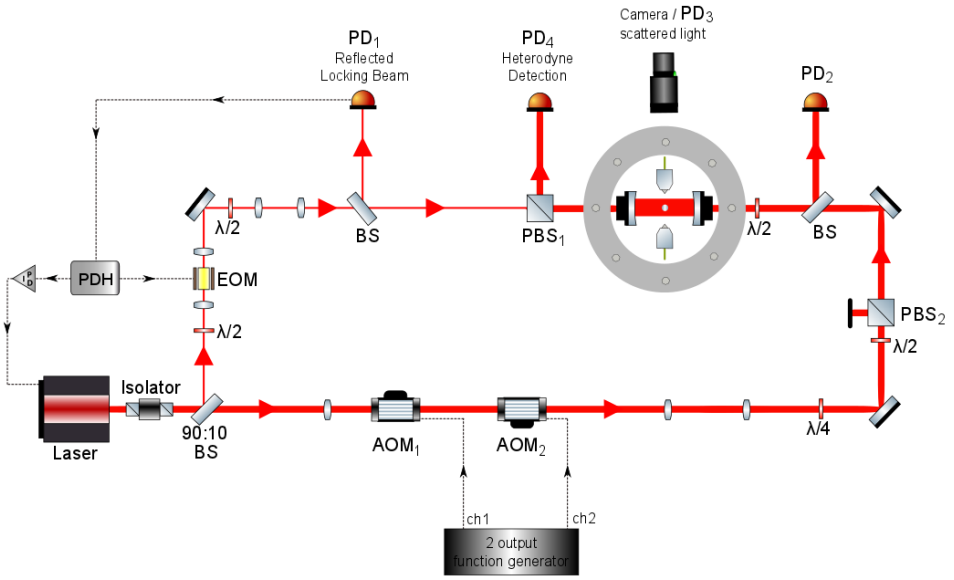

Figure 4.1: Laser detection set-up used in the heterodyne measurement of the levitated nanoparticle in a hybrid trap experiment. The laser beam is split 90:10 for cooling and locking modes. The detuned strong cooling beam is beat with the weak beam for heterodyne signal at PD_4; the phase of the heterodyne beam is not controlled. Reflected and scattered signals are also captured at PD_3 and PD_2. The weak beam is used for the Pound-Drever-Hall locking of the cavity.

particle's motion is continuously monitored through the reflected cavity output, scattered light, and heterodyne signal at PD_2, PD_3, and PD_4, respectively.

4.2 Hybrid trap apparatus

The Paul trap is mounted on a remote controllable xyz translation stage that allows fine control over its alignment with the cavity. Misalignment and gravity result in an offset from the beam waist which weaken the coupling, or worse, cause particle loss.

Instead of the conventional hyperbolic geometry, we use for our Paul trap a pair of metallic needle structures with tapered ends. As Fig. 4.2a shows, this has the advantage of easier integration with the cavity and readout probes compared to the bulkier hyperbolic electrodes (see Fig. 3.2b). The distance between the tips and taper angles determines the electric field, which deviates from a perfect quadrupolar field (compare with Fig. 3.2a) for distances other than small excursions around the antinode. We account for this reduction in trap confinement by introducing a trap efficiency parameter $\epsilon < 1$ to Eq. 3.12:

$$\omega_{\mathrm{s}}^{u} \propto \frac{Q_{\epsilon} V_0}{m \omega_{\mathrm{d}} r_0^2}, \tag{4.1}$$

where we define the effective charge $Q_{\epsilon} = \epsilon Q$. Experimentally, this means a higher voltage

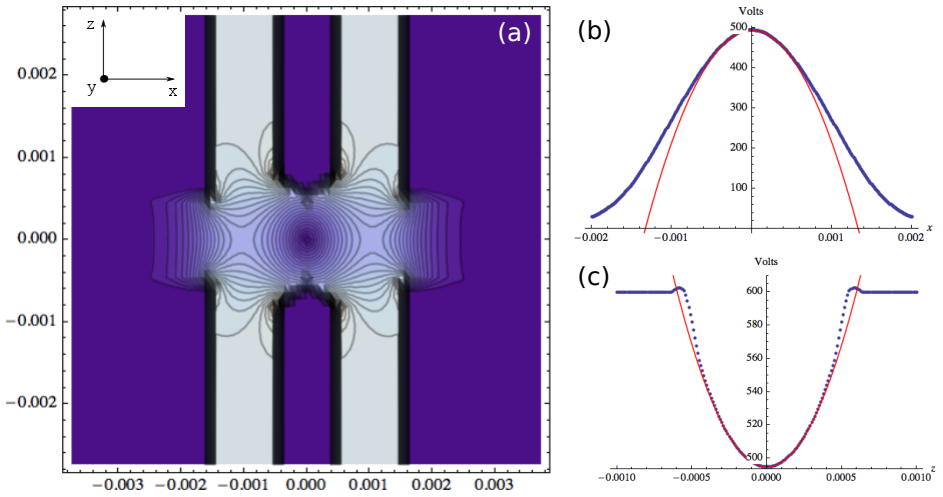

Figure 4.2: **(a)** Imperfect quadrupole field arising from the needle trap geometry used in the hybrid trap experiment. In contrast with the conventional hyperbolic electrodes of the Paul trap (Fig. 3.2b), the open geometry of the needle trap facilitates better integration with the cavity and other components of the hybrid trap. The width of the electrodes, as well as the taper angles at the tips, influence the resulting field, which is a slight modification to the perfect Paul trap potential shown in Fig. 3.2a **(b)** Comparison of the needle trap potential with the ideal case in the x and z directions. For small excursions, both are approximately parabolic. Both images are adapted from [6].

needs to be applied to achieve the desired secular frequency, relative to the ideal Paul trap. Paschen's law limits the applied voltage as a function of the distance between the electrodes, as well as the pressure in the vacuum chamber. When loading the particle around $0.1 - 1$ mbar, we must choose $V_0 \lesssim 300$ V to avoid electric discharge [6].

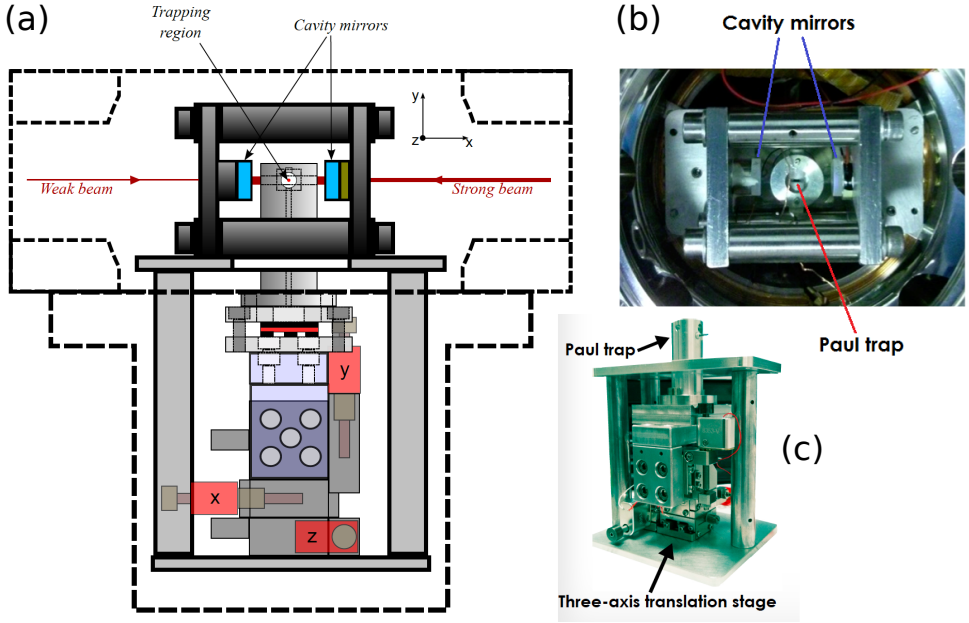

Figure 4.3: **(a)** Detailed illustration of the hybrid electro-optical trap, as well as the xyz translation stage used to align the Paul trap with the cavity, and to center the particle in the cavity waist for better trapping and cooling. The cavity mirrors are ≈ 1 mm in length, and the Paul trap needles are separated by 1 mm. **(b)** Actual photographs of the experimental apparatus. Images are adapted from [6].

The cavity mirrors have a nominal reflectivity $R = 99.9984\%$ which theoretically results in a finesse $\mathcal{F} = \pi\sqrt{R}/(1-R) \approx 200,000$. Measurements of the cavity linewidth κ obtained by the scanning technique [6], however, give $\mathcal{F} = \pi c/(\kappa L) \approx 50,000$, which is remarkably lower from the theoretical value due to the dirt acquired by the mirrors during assembly. Actually, while a high $\mathcal{F}$ is desirable for cooling, it presents a significant challenge in terms of cavity locking.

4.3 Results

In this section, we summarise three key experimental results published in [10] that demonstrated both quadratic coupling and strong cavity cooling of levitated particles in a hybrid trap. Significant improvement in the cooling rate over previous hybrid trap experiment [58] was achieved through a high-finesse cavity ($\mathcal{F} = 50,000$).

4.3.1 Determining effective charge and photon number

We have little control in the well number N that the particle gets caught in, nor do we have the means to directly measure N in the experiment. However, we can infer N by comparing experimental traces with a stochastic simulation of the full nonlinear dynamics for different N.

The Langevin equations are derived from the combined potential $V_{\text{tot}} = V_{\text{opt}} + V_{\text{ion}}$ (Eqs. 3.4 and 3.8), with additional delta-correlated, Gaussian noise terms to model bath couplings, as well as an offset term in the y-direction to account for misalignment and gravity. A complete simulation of the nonlinear dynamics requires knowledge of certain experimental quantities: (i) damping rates — as mentioned, κ is measured directly via a scanning technique [6], while kinetic theory gives $\Gamma_{\text{M}} = 16P/(\pi\bar{v}\rho R)$, where P is pressure (in bar), $\bar{v}$ is the mean velocity of air at 300 K, R is the particle radius, and ρ is its density [80]; (ii) coupling strength A given in Eq. 3.5; (iii) intracavity photon number $\left|\bar{\alpha}^2\right|$; and (iv) the effective charge Q_ϵ. (i) and (ii) can be completely determined from the experimental parameters listed in Table 4.1.

The laser power P_{in} can be directly measured in experiments — for a critically-coupled cavity, the intracavity photon number $|\bar{\alpha}|^2 = \frac{P_{\text{in}}}{\hbar\omega_{\text{l}}}\frac{\kappa/2}{\kappa^2/4+\Delta^2}$. However, despite attempts at mode-matching, a significant amount of power still ends up reflected away from the cavity. Hence, $\left|\bar{\alpha}^2\right|$ as well as Q_ϵ remain unknown.

Fig. 4.4 plots the ω_{M} and ω_{S} obtained from three data sets to be discusssed in the following sections. Equation 3.29 provides a useful technique to simultaneously determine the effective charge and the intracavity photon number from secular and mechanical fre-

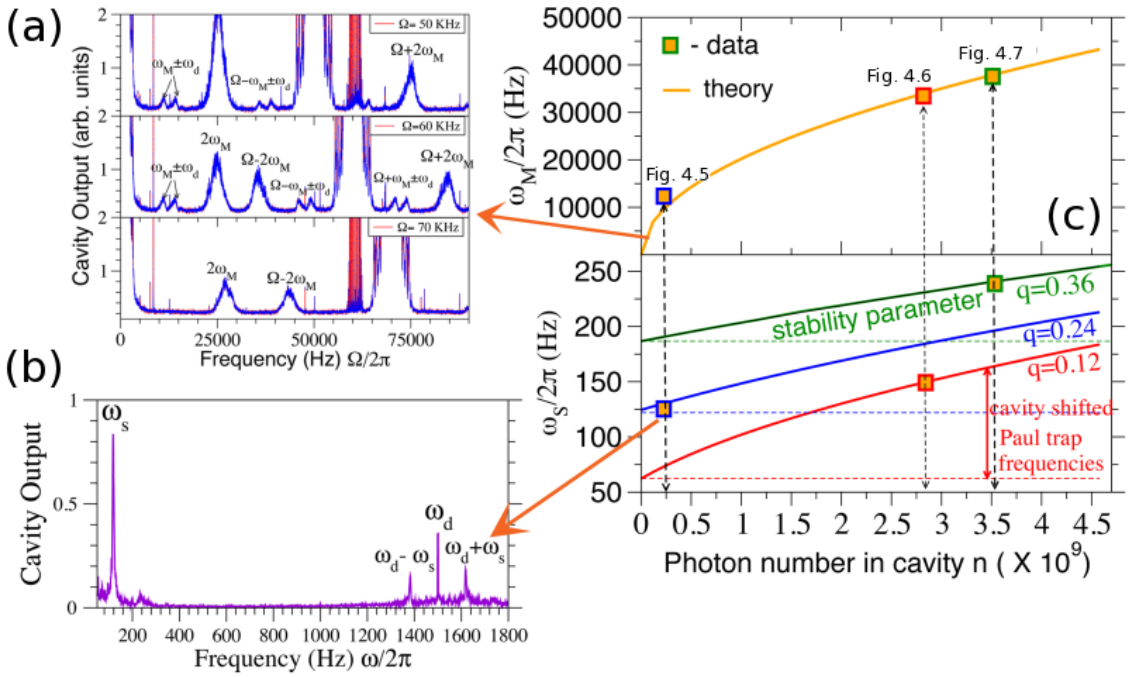

Figure 4.4: A new effect of the stronger light-matter coupling is a newly identified "cavity shift" of the Paul trap secular frequencies. This can be used to measure on the nanosphere and the photon number in the cavity. **(a)** Shows three sets of data (middle panel is discussed in the main text). Red spikes represent instrumental noise, of no physical significance. Note the lowest panel shows data capture for N = 0 hence only the quadratic coupling peak at $2\omega_M$ can be seen. **(b)** Shows low frequency data, used to obtain the secular frequencies. **(c)** The Paul trap secular frequencies experience a significant shift due to their interaction with the cavity field. Since both ω_S and ω_M must correspond to the same photon number n this allows read-out of the stability parameter $q \equiv q_{x,y}$ and hence the charge on the nanosphere Q and of n: as shown in the graph, both frequencies must lie on the same vertical line. As the optomechanical cooling rates $\Gamma_{\text{opt}} \propto \text{nN}^2 q^2$ for small oscillations, these are important parameters in our simulation. For a Paul trap of efficiency $\epsilon = 1$, $q = 0.12$ corresponds to $Q_\epsilon \equiv Q = 1$ in the experiment. Figures and captions adapted from [10].

quency readings. This is important because $\Gamma_{\text{opt}} = \Gamma_{\text{opt}}(Q_\epsilon, |\bar{\alpha}|^2)$ for the hybrid trap. As was shown in Eq. 3.27, the standard formula for the cooling rate is modified due to the effect of the Paul trap on Δ, ω_{M}, and g.

4.3.2 Quadratic coupling

In Fig. 4.5, we present the $\text{PSD}^{1/2}$ of the heterodyne signal, as well as various simulated heterodyne spectra for different trapping well number N. $\text{PSD}^{1/2}$ is used to enhance the otherwise small $G2 : G1$ ratio. At $N = 5$, we observe a pair of small peaks at $\omega_{\text{M}} \pm \omega_{\text{d}}$ as well as a dominant peak at $2\omega_{\text{M}}$; these features also appear as sidebands of the heterodyne frequency Ω. Being a low well catch, we expect the particle to oscillate at the bottom well where the quadratic coupling dominates. However, $k^2 \sim 10^{12}$ dependence notwithstanding, G_2 are notoriously weak because fluctuations in x^2 are weaker (in the quantum case for

example it will be scaled by $x_{\mathrm{zpf}}^2 \sim 10^{-24}$), thus limiting cooling via quadratic coupling. Nonetheless, this is the first demonstration of quadratic coupling in levitated systems.

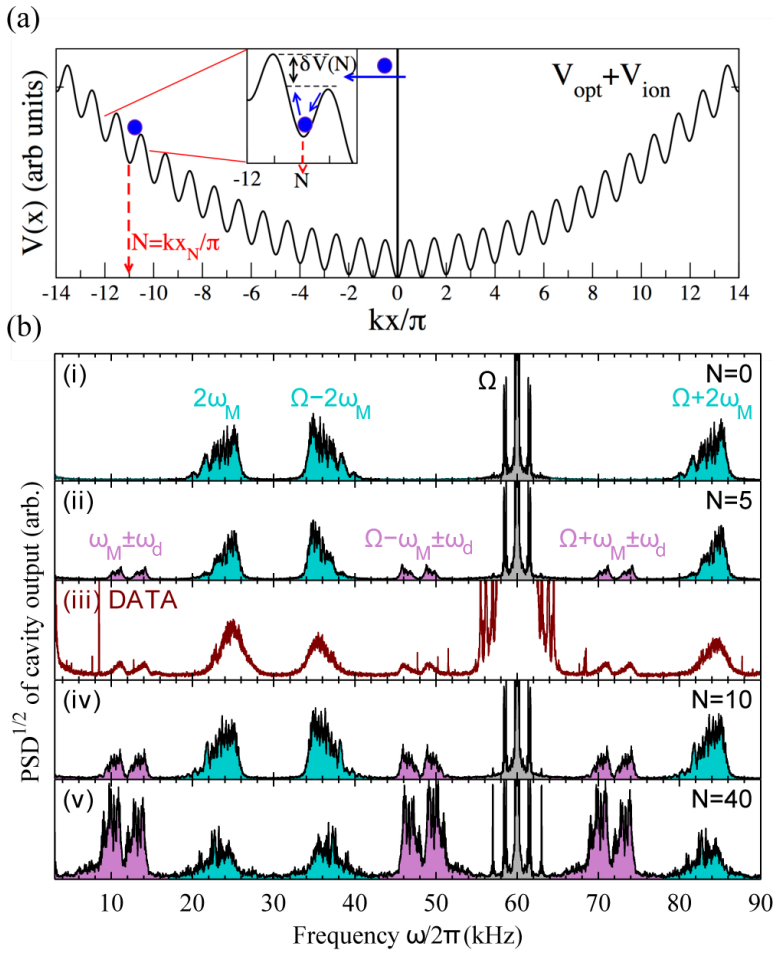

Figure 4.5: **(a)** The hybrid trap potential combines the Paul trap potential with the standing wave potential of the cavity mode. The relative strength of the optomechanical couplings (the $G_1 : G_2$ ratio) depends strongly on N, the optical well the particle becomes trapped in. **(b)** Comparison between simulations of the nonlinear stochastic dynamics(i,ii,iv,vi) and an experimental spectrum, showing the latter corresponds to trapping in low N $\simeq$ 5 (iii). $\sqrt{\mathrm{PSD}}$ of the steady-state heterodyne spectra are shown on a linear scale. All spectra show the strong beat frequency component at $\omega = \Omega/2\pi = 60$ kHz which is the detuning between the on-resonance locking beam and the red detuned cooling beam. The mechanical motion can be observed as sidebands around this peak at $\omega = \Omega \pm \omega_{\mathrm{M}}$ due to G_1 coupling and at $\Omega \pm 2\omega_{\mathrm{M}}$ due to G_2 coupling. There are also peaks at ω_{M} and $2\omega_{\mathrm{M}}$ due to direct modulation in cavity transmission of the particle. $P = 10^{-2}$ mBar, input power $P_{in} = 0.07$ mW and particle charge $Q = 2$. Figures and captions adapted from [10].

4.3.3 Transient dynamics

Figure 4.6 shows the transient dynamics of the particle upon capture, which according to simulations is at $N = 450$. This corresponds to an analytical $\Gamma_{\mathrm{opt}} \simeq 400$ Hz. Each spectra is an average of 2.4 ms, with 0.2 ms interval between each data set. Despite being a high N capture, both linear and quadratic peaks are observed initially, although the latter becomes supressed much faster as the particle settles into equilibrium. The standard expression for

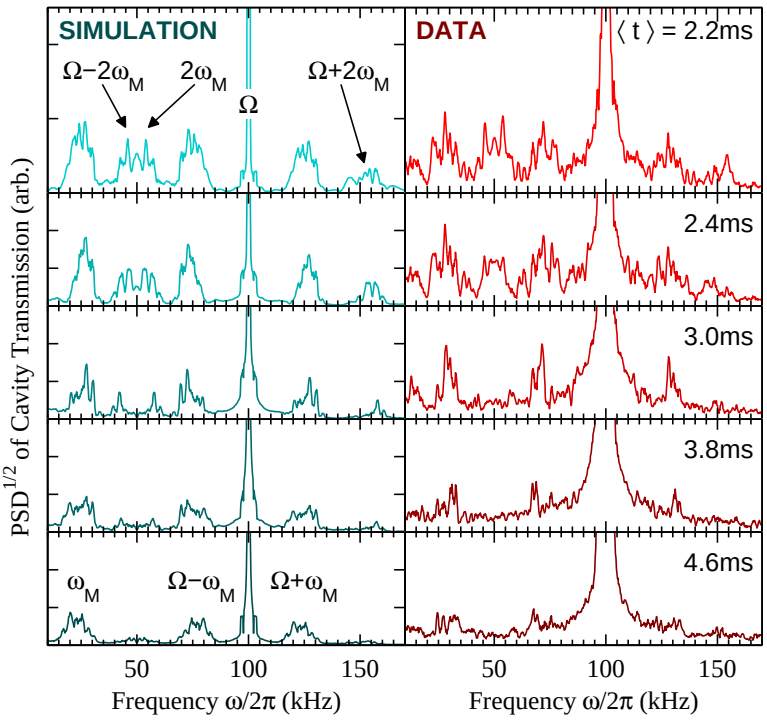

Figure 4.6: Cooling dynamics of a particle which is first captured in a high (N ≈ 450) well. From from steady-state, it is perturbed so its cooling and re-equilibration may be observed. The (expected) much faster damping of the G_2 sidebands at $\omega = 2\omega_M, \Omega \pm \omega_M$ relative to the G_1 sidebands at $\omega_M, \Omega \pm \omega_M$ is clearly seen. Both experimental data and nonlinear stochastic simulations show reductions in G_1 sideband heights which indicate cooling on ms timescales and hence $\Gamma_{\rm opt} \sim 1000\ {\rm s}^{-1}$. $\sqrt{\rm PSD}$ of heterodyne spectra are shown on a linear scale. $P = 3 \times 10^{-4}$ mBar , $P_{in} = 0.5$mW, $Q = 1$ (see Fig.4b). We set $\Omega = -\Delta = 2\pi \times 100\,$kHz. From these values and Eq.3.27 we obtain $\Gamma_{\rm opt} \approx 400{\rm s}^{-1}$, in broad agreement with the observed ms cooling timescales. Figures and captions adapted from [10].

temperature far from the ground state $T \simeq 300{\rm K} \times \Gamma_{\rm M}/(\Gamma_{\rm opt} + \Gamma_{\rm M})$ implies $T \approx 0.3$K at steady state.

4.3.4 Strong cavity cooling

Finally, Fig. 4.7a presents the heterodyne PSD as the pressure is varied from 10^{-1} to 10^{-5} mbar. Each PSD is an average of 15 sets of 1 second duration data and are smoothed over 100 Hz. Apart from the redudant sidebands of Ω, there is only one dominant sideband at $\omega_{\rm M}$. This is consistent with the simulations indicating capture at $N \simeq 300 - 600$. The area under the sideband decreases linearly with pressure, consistent with an analytical cooling rate of $\Gamma_{\rm opt} \approx 2000$ Hz from Eq. 3.27. We have evidence of strong cooling as the particle was actually still observed at 10^{-6} mbar, although the experiment is limited by detection sensitivity which affects our ability to read the area under the sideband.

Subtracting the noise floor from each of the data set at different pressures, we plot the integrated area under the mechanical sideband in Fig. 4.7b and show at least 1000-fold cooling from room temperature. A calibration constant C converts the heterodyne PSD

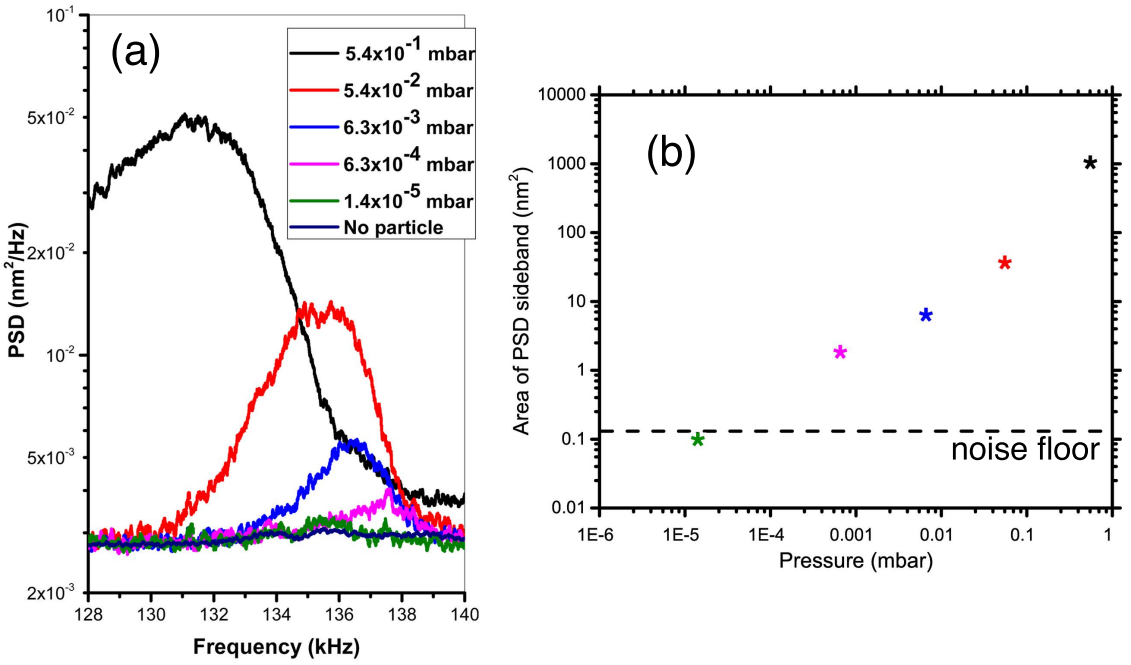

Figure 4.7: **(a)** Shows steady state data of a strongly cooled particle. The calibrated PSD spectra show single dominant peaks, indicating high N ($\simeq 300 - 600$) trapping. Trapping occurred at a pressure $P = 0.5$ mBar ($T \simeq 300$K) which was then gradually reduced to $P = 5 \times 10^{-6}$ mBar, the current limit of our apparatus. PSDs (y-axes) are plotted on a log scale. Also shown is a background PSD taken with no particle trapped. The peak heights and hence T^{-1}, scale approximately with P. For $P \leq 10^{-5}$ mBar it is no longer possible to detect the motional sidebands although it can be observed from the scattered light that the particle is still trapped. $F = 50,000$ and $P_{in} = 0.6$mW; for N $\simeq 300$ Eq.3.27 predicts $\Gamma_{\rm opt} \approx 2000\ s^{-1}$. **(b)** Shows the change in area of the PSD as a function of pressure demonstrating that we can measure a 1000 fold reduction in the area and thus the temperature limited by the noise floor of the measurement. Figures and captions adapted from [10].

in units of $\mathrm{mV}^2/\mathrm{Hz}$ to position PSD in units of m/Hz. The heterodyne PSD is directly proportional to the cavity output PSD: $S_{\rm het}(\omega) = CS_{yy}^{\rm out}$. Despite exhibiting nonstandard sideband structure, we will show in Chapter 5 that $S_{\rm yy}^{\rm out} \approx \bar{G}_1|\eta(\omega)|^2 S_{xx}$, with $\eta(\omega)$ given in Eq. 2.62. Hence, $S_{xx} \approx S_{\rm het}(\omega)/(C\bar{G}_1|\eta(\omega)|^2)$. From Chapter 2, we know that the variance of the mechanical motion equals the area of the PSD sideband, which by equipartition theorem is related to the temperature. Assuming the largest area $A_{\rm max}$ corresponds to $T = 300$ K, then by equipartition theorem: $m\omega_{\rm M}^2 A_{\rm max}/(C\bar{G}_1|\eta(\omega)|^2) \approx 300 k_{\rm B}$, leading to $C \sim 2 \times 10^{11}$ [10].

Table 4.1: Experimental parameters for stochastic Runge-Kutta simulation

	Parameter	Symbol	Value
Cavity	radius of curvature	r_{c}	25 mm
	length	L	13.5 ± 0.2 mm
	decay rate	$\kappa/2$	$2\pi \times 85 - 115$ kHz
	detuning	Δ	up to -200 kHz
	laser frequency	ω_{l}	1064 nm
Paul trap	voltage (peak amplitude)	V	$300 - 900$ V
	distance between electrodes	$2r_0$	1 mm
	drive frequency	ω_d	$2\pi \times 1500$ Hz
Particle	density	ρ	$2198\,\mathrm{kg\,m^3}$
	radius	R	200 nm
	relative permitivity	ϵ_r	3.8
Ambient air	pressure	P	$10^{-1} - 10^{-5}$ mbar
	mean velocity at 300 K	$\bar{v}$	≈ 500 m/s
	temperature	T	300 K

5 | Split-sideband spectroscopy

This chapter presents a quantum-mechanical analysis of the split-sideband spectra characteristic of doubly-modulated optomechanical systems like the particle in a hybrid trap. Unlike in Chapter 3, generic, simultaneous modulations in g and ω_{M} are considered. Section 5.1 presents an iterative solution of the split-sideband spectra from frequency-shifted Langevin equations, while Sec. 5.2 considers a fast-cavity solution, where the optical field is assumed to follow the motion $\propto \cos^2(k\hat{x})$. In both approaches an analytical model for computing the split-sideband ratio, and conditions for the complete suppression of one of the peaks are obtained. Finally, the last section discusses how thermometry changes for a noise power spectrum with split-sidebands that differ from, and coexists with, the usual Stokes/anti-Stokes sidebands of a canonical optomechanical system. Our analytical models are verified using nonlinear, 3D stochastic simulation of the hybrid trap dynamics. A significant part of this chapter has been adapted from [12] and [9].

5.1 Iterative solution

As explained in Chapter 3, the optomechanical parameters ultimately emerge from the polarisation response of the dielectric particle to the cavity field, which can significantly change across the optical well. The particle can have either a dominantly linear or dominantly quadratic coupling depending on the position x_0, although gradient forces alone will drive the particle to the antinode where the cooling is weak. The Paul trap not only assists in trapping at high vacuum, but also proves to be indispensable for cooling by periodically pulling the particle away from the antinode. However, unlike other auxilliary fields typically used, such as an optical tweezer, the quadrupole field of the Paul trap causes a time-dependent excursion in the equilibrium position $x_0(t)$, causing the following time-dependent $g(t)$ and $\omega_{\mathrm{M}}(t)$:

$$g(t) = 2\bar{g}\sin\omega_{\mathrm{d}}t \tag{5.1}$$

$$\omega_{\mathrm{M}}(t) = \overline{\omega}_{\mathrm{M}} + 2\omega_2\cos 2\omega_{\mathrm{d}}t \tag{5.2}$$

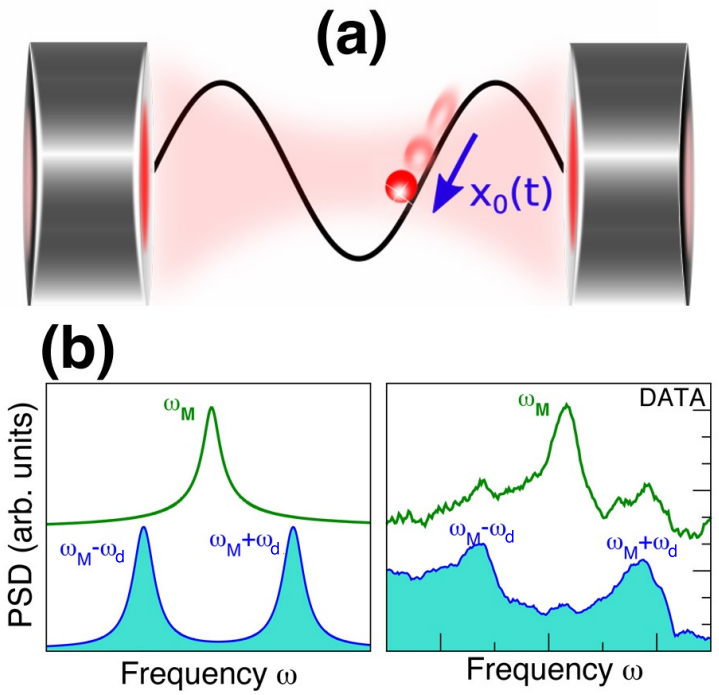

Figure 5.1: **(a)** An example of a modulated optomechanical system: for set-ups where an oscillator is dipole-force trapped by the standing wave of a cavity mode, there is no optomechanical cooling at the antinode $x_0 = 0$ (the potential minimum of an optical well of width $\lambda/2$), since there is no light-matter coupling. Hence, such set-ups [11, 10] require an auxiliary field to pull the centre of the mechanical oscillation away from $x_0 = 0$. In electro-optical traps [10], a slow oscillation is induced such that $x_0(t) = \mathrm{X_d} \sin \omega_\mathrm{d} t$, enabling cooling. For small oscillations, here we find this corresponds to an effective modulation of the optomechanical coupling $g(t) = 2\bar{g} \sin \omega_\mathrm{d} t$ and a simultaneous, out-of-phase, modulation of the mechanical frequency $\omega_\mathrm{M}(t) = \overline{\omega}_\mathrm{M} + 2\omega_2 \cos(2\omega_\mathrm{d} t)$. **(b)** For a small ($\mathrm{X_d} \ll \lambda$) modulation, $\omega_2 \approx 0$ and only g is appreciably modulated. In that case, while the Power Spectral Density (PSD) of the displacement spectrum, $S_{\mathrm{xx}}(\omega) \equiv \langle |\hat{\mathrm{x}}(\omega)|^2 \rangle$, is still peaked at $\pm\omega \simeq \omega_\mathrm{M}$, the cavity spectrum, $(S_{\mathrm{yy}}(\omega))$ exhibits a characteristic structure of "twin peaks" at $\pm\omega = \omega_\mathrm{M} \pm \omega_\mathrm{d}$ (left panel). The measured cavity output spectrum (right panel) detected by a heterodyne method, also exhibits this behaviour. Figures and captions adapted from [12].

where $\bar{g}$ and $\overline{\omega}_\mathrm{M}$ are the mean values and ω_2 is the amplitude of the mechanical frequency modulation. Note that g here denotes linear coupling. For the particular system of a particle in a hybrid trap, these quantities are derived in Sec. 3.3.2. However, in fact, any generic auxilliary field that causes a harmonic $x_0(t)$ within the optical well (Fig. 5.1a) will lead to Eqs. 5.1 and 5.2. Without further specifications, we will now derive the Langevin equations in frequency space for a doubly-modulated system.

The Langevin equations for a standard optomechanical system are derived in Sec. 2.3.2. Having high quality factors, the rotating wave approximation (RWA) will be used for both the cavity and mechanical oscillators. From Eqs. 2.60 and 2.64, the optical amplitude and

position quadratures in frequency space[1] are:

$$\hat{Y}_{\rm a}(\omega) = ig\eta(\omega)\hat{X}(\omega) + \sqrt{\kappa}\hat{Y}_{\rm in}(\omega) \tag{5.3}$$

$$\hat{X}(\omega) = ig\mu(\omega)\hat{Y}_{\rm a}(\omega) + \sqrt{\Gamma_{\rm M}}\hat{X}_{\rm th}(\omega) \tag{5.4}$$

where $\eta(\omega)$ and $\mu(\omega)$ are functions of the optical and mechanical susceptibilities; see Eqs. 2.62 and 2.66 — again, the "RWA" label are being dropped to simplify notations. The first terms represent the backaction noise while the second terms are the filtered bath noises defined as:

$$\begin{aligned}\hat{Y}_{\rm in}(\omega) &\equiv \eta(\omega)\hat{Y}_{\rm p,in}(\omega) + \eta'(\omega)\hat{Y}_{\rm a,in}(\omega) \\ &= \chi_{\rm O}(\omega)\hat{a}_{\rm in}(\omega) + \chi^*_{\rm O}(-\omega)\hat{a}^\dagger_{\rm in}(\omega) \qquad (5.5)\\ \hat{X}_{\rm th}(\omega) &\equiv \mu(\omega)\hat{P}_{\rm in}(\omega) + \mu'(\omega)\hat{X}_{\rm in}(\omega) \\ &= \chi_{\rm M}(\omega)\hat{b}_{\rm in}(\omega) + \chi^*_{\rm M}(-\omega)\hat{b}^\dagger_{\rm in}(\omega) \qquad (5.6)\end{aligned}$$

Note that simultaneously solving Eqs. 5.3 and 5.4 leads to a closed-form solution for $\hat{Y}_{\rm a}(\omega)$, which can then be used to calculate the cavity output field. Introducing the g modulation, one sees from the modified Langevin equations:

$$\hat{Y}_{\rm a}(\omega) = \bar{g}\eta(\omega)\Big[\hat{X}(\omega+\omega_{\rm d}) - \hat{X}(\omega-\omega_{\rm d})\Big] + \sqrt{\kappa}\hat{Y}_{\rm in}(\omega) \tag{5.7}$$

$$\hat{X}(\omega) = \bar{g}\mu(\omega)\Big[\hat{Y}_{\rm a}(\omega+\omega_{\rm d}) - \hat{Y}_{\rm a}(\omega-\omega_{\rm d})\Big] + \sqrt{\Gamma_{\rm M}}\hat{X}_{\rm th}(\omega) \tag{5.8}$$

that such a closed form solution is not possible due to $\hat{Y}_{\rm a}(\omega)$ probing *shifted* displacement noises. As the modulation becomes stronger $S_{Y_{\rm a}Y_{\rm a}}(\omega)$ will have to contain noises from $\omega \pm n\omega_{\rm d}$ ($n \in \mathbb{Z}$), with n becoming higher as the modulations become stronger, although this has yet to be observed in experiments. One can only then calculate the measured spectrum iteratively, up to a finite order in the modulation strengths $\bar{g}$ and ω_2.

One can readily see why such a twin-peak spectrum appears in the experiment (see Fig. 4.5 and 5.1b). From Eq. 5.7, the cavity ampltitude spectrum measures the shifted displacement spectrum:

$$S_{Y_{\rm a}Y_{\rm a}}(\omega) \propto \left\langle \left| \hat{X}(\omega+\omega_{\rm d}) - \hat{X}(\omega-\omega_{\rm d}) \right|^2 \right\rangle, \tag{5.9}$$

resulting in sidebands of equal height at $\omega_{\rm M} \pm \omega_{\rm d}$, even for overwhelmingly small linear coupling.

Note that we have conveniently neglected the cross-correlation terms in Eq. 5.9. This is

[1] A factor of 1/2 is being absorbed into the definition of g here.

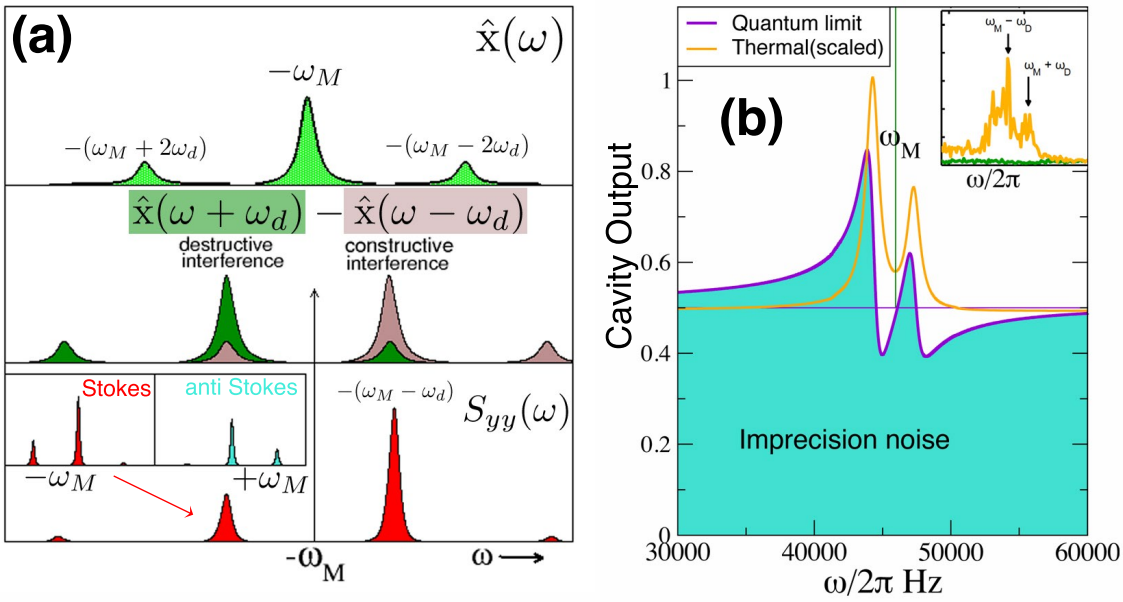

Figure 5.2: **(a)** For a generic system where both $g(t) = 2\bar{g}\sin\omega_{\rm d}t$ and $\omega_{\rm M}(t) = \overline{\omega}_{\rm M} + 2\omega_2\cos 2\omega_{\rm d}t$ are modulated, the figure illustrates schematically how the spectrum of the cavity field ($S_{yy}(\omega)$), arises from the spectrum of the mechanical motion. Top panel illustrates the $\hat{\rm x}(\omega)$ spectrum: the effect of $\omega_2 > 0$ is to produce additional $\pm 2\omega_{\rm d}$ side-peaks. Middle panel: unlike the typical optomechanical case, the cavity field now follows $\hat{\rm x}(\omega+\omega_{\rm d}) - \hat{\rm x}(\omega-\omega_{\rm d})$ rather than $\hat{\rm x}(\omega)$. The interference of the individual $\hat{\rm x}(\omega \pm \omega_{\rm d})$ components (shown in brown/green) yields constructive enhancement near $\omega \simeq \pm(\omega_{\rm M} - \omega_{\rm d})$, and destructive cancellation near $\omega \simeq \pm(\omega_{\rm M} + \omega_{\rm d})$. Instead of the "twin peak" structure seen in Fig. 5.1 for $\omega_2 = 0$, the resultant cavity output sidebands display a pair of peaks of asymmetric heights (lower panel). For small $\bar{g}$, the ratio between peaks $r \simeq (\omega_2 - 2\omega_{\rm d})^2/(\omega_2 + 2\omega_{\rm d})^2$ so the $\omega_{\rm M} + \omega_{\rm d}$ peak is strongly suppressed for $\omega_2 \sim 2\omega_{\rm d}$ ($r \approx 0$). This asymmetry is distinct from the usual Stokes/antiStokes sideband asymmetry at $\pm\omega \simeq \omega_{\rm M}$, which is still present. Lower panel shows the Stokes peaks (red). **(b)** In thermal regimes, the ratio r is insensitive to $\Gamma_{\rm M}$; however, as $\Gamma_{\rm M} \to 0$ and the backaction limit is attained, correlations between back-action and incoming noise alters the relative heights of the peaks, mainly since ponderomotive squeezing lowers the height of the $\omega_{\rm M} + \omega_{\rm d}$ peak relative to the imprecision floor. For incoming quantum shot noise, significant changes in r arise only if the oscillator is near the ground state. Inset reproduces part of Fig. 5 of [10] illustrating previously overlooked asymmetries in experimental sidebands which supports our modulated-optomechanics model. Figures and caption adapted from [12].

valid for excursions in g only; however, a simultaneous, out-of-phase $\omega_{\rm M}$ modulation given by Eq. 5.2 will result in an interference effect that lead to split-sideband asymmetry. As Figure 5.2 illustrates, $\hat{X}(\omega)$ acquires additional sidebands at $\omega \pm 2\omega_{\rm d}$, which then interfere with one another when the optical field detects the shifted spectrum. In fact, when the $\omega_{\rm M}$ modulation is strong enough, one of the sidebands become completely suppressed.

Let us now look more closely at the algebra to obtain an analytical model of the split-sideband asymmetry. For modest backaction ($\bar{g}$ small), $\hat{X}^{\pm}(\omega) \equiv \hat{X}(\omega + \omega_{\rm d}) - \hat{X}(\omega - \omega_{\rm d})$

can be written in terms of input noises only:

$$\begin{aligned}\hat{X}^{\pm}(\omega) &\approx \sqrt{\Gamma_{\rm M}}\Big[\hat{X}_{\rm th}(\omega+\omega_{\rm d})-\hat{X}_{\rm th}(\omega-\omega_{\rm d})\Big]+\bar{g}\hat{Y}_{\rm BA}(\omega)\\ &- \mathrm{i}\omega_2\sqrt{\Gamma_{\rm M}}\hat{X}^{(\omega_2)}(\omega)-\mathrm{i}\omega_2\bar{g}\hat{Y}^{(\omega_2)}_{\rm BA}(\omega)\end{aligned} \tag{5.10}$$

where the first two terms are the thermal noises, and $\hat{Y}_{\rm BA}$ represents the backaction terms driven by the imprecision noise. The last two terms are the correction terms due to $\omega_{\rm M}$ excursion.

In the thermal regime, and with $\omega_2 = 0$, $\hat{Y}_{\rm BA}(\omega)$ have negligible contribution, so the shifted spectrum mainly comes from incoming thermal noises weighted by the mechanical susceptibility $\chi_{\rm M}(\omega) = \left[-\mathrm{i}(\omega-\omega_{\rm M})+\frac{\Gamma_{\rm M}}{2}\right]^{-1}$. The anti-Stokes sideband for example, is primarily due to the weighted thermal noise operators $\chi_{\rm M}(\omega\pm\omega_{\rm d})\hat{b}_{\rm in}(\omega\pm\omega_{\rm d})$. The susceptibilities $|\chi_{\rm M}(\omega\pm\omega_{\rm d})|$ are sharply peaked at frequencies $\omega = \omega_{\rm M}\mp\omega_{\rm d}$ (since $\Gamma_{\rm M}$ is small), yielding the "twin peaks" structure since the ratio of the twin peak weights $r = |\chi_{\rm M}(\omega-\omega_{\rm d})|^2/|\chi_{\rm M}(\omega+\omega_{\rm d})|^2 = 1$.

The main effect of ω_2 is to introduce the extra correction from the $\hat{X}^{(\omega_2)}(\omega)$ term which means replacing the thermal weights:

$$\chi_{\rm M}(\omega\pm\omega_{\rm d}) \;\rightarrow\; \chi_{\rm M}(\omega\pm\omega_{\rm d})[1-\mathrm{i}\omega_2\chi_{\rm M}(\omega\mp\omega_{\rm d})] \tag{5.11}$$

Evaluating the corrections (the terms in square brackets) near the frequency peaks of the noise, we find they are $\approx (2\omega_{\rm d}\pm\omega_2)/2\omega_{\rm d}$ so the ratio of peaks in the PSD would be:

$$r \approx (2\omega_{\rm d}-\omega_2)^2/(2\omega_{\rm d}+\omega_2)^2, \tag{5.12}$$

predicting a full cancellation for $2\omega_{\rm d}\sim\omega_2$.

5.1.1 Backaction limit

Figure 5.3 shows that the split-sideband ratio given in Eq. 5.12 holds for both Stokes and anti-Stokes peaks even when $\Gamma_{\rm M}\to 0$ is taken up to the back-action limit. This is true for $S_{X^{\pm}X^{\pm}}(\omega)$ as well as $S_{Y_{\rm a}Y_{\rm a}}(\omega)$ that probes it.

However, a very different picture emerges the cavity output is considered instead: $\hat{Y}_{\rm a,out}(\omega) = \hat{Y}_{\rm a,in}-\sqrt{\kappa}\hat{Y}_{\rm a}(\omega)$. The spectrum $S^{\rm out}_{Y_{\rm a}Y_{\rm a}}(\omega)$ has to contain cross-correlations between the incoming cavity amplitude noises and the backaction fluctuations in $\hat{Y}_{\rm a}(\omega)$. For $\Delta\neq 0$, which is the case for optomechanical cooling, such a cross-correlation leads to ponderomotive squeezing within a narrow band of frequencies around resonance, and serves to change the split-sideband ratio when one of the peaks falls into the subshotnoise floor.

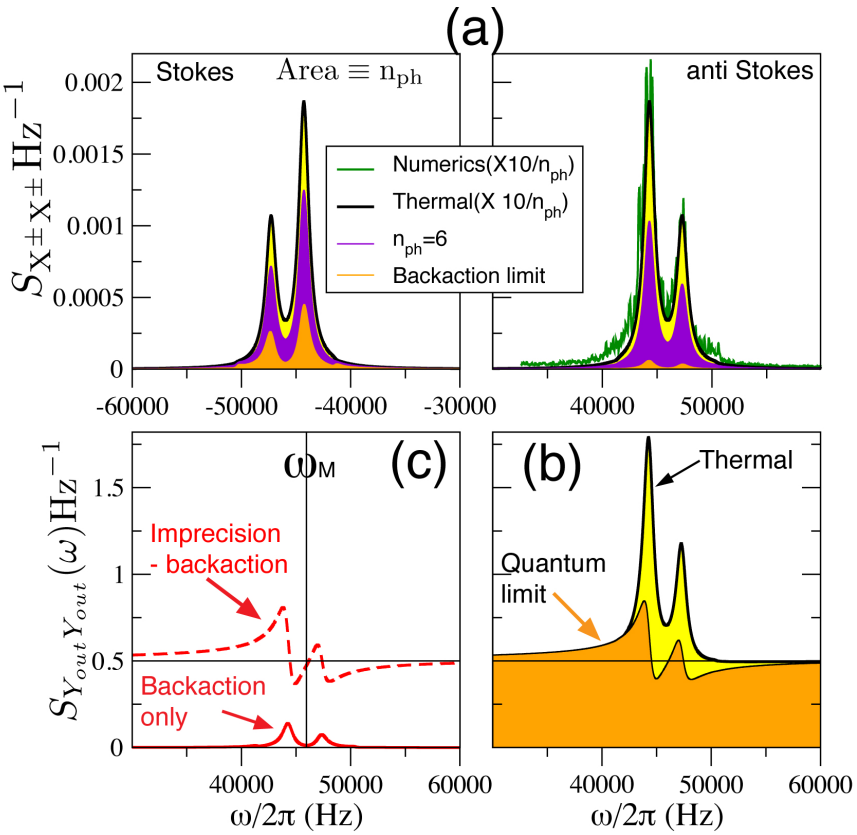

Figure 5.3: Comparison between the thermal spectrum and the quantum limit, using the analytical solutions with increasing g, ω_2 in the sideband-resolved limit, which can yield ground state cooling at sufficiently low pressures. **(a)** Shows $S_{\mathrm{X}^{\pm}\mathrm{X}^{\pm}}(\omega)$ for Stokes and anti-Stokes sidebands, as $\Gamma_M \to 0$ while the optomechanical cooling rate Γ_{opt} in each graph remains fixed. The individual sideband shapes are unchanged, but Stokes/anti-Stokes asymmetry develops. The symmetric classical spectra are scaled to a height of 1 corresponding to $\Gamma_{\mathrm{M}} = 10^{-4}\mathrm{s}^{-1}$. $\omega_2/2\omega_{\mathrm{d}} = 0.24$, for $2\omega_{\mathrm{d}} = 3 \times 2\pi$ kHz; $g = 18,500\mathrm{s}^{-1}$, $\overline{\omega}_{\mathrm{M}} = 46 \times 2\pi$ kHz, $\kappa/2 = 26 \times 2\pi$ kHz, $\Delta \simeq -\omega_{\mathrm{M}}$. **(b)** The same solutions in (b) are now added to incoming imprecision noise to obtain output spectra $S_{\mathrm{y}_{out}\mathrm{y}_{out}}(\omega)$. At high phonon occupancies, the shape is unchanged. As $n_{ph} \to n_{BA}$, the ratio above the quantum imprecision floor alters significantly. **(c)** Shows individual contributions to the PSD; the pure backaction term has the same shape as the thermal split sidebands; its interference with incoming imprecision noise lowers the height of the $\omega_{\mathrm{M}} + \omega_{\mathrm{d}}$ sideband. Figures and captions adapted from [12].

Obviously, this effect is very small, and can be easily masked by thermal fluctuations of the mechanical oscillator. The striking change in split-sideband ratio unique to modulated systems may then offer an additional signature of the quantum regime, in conjunction with the typical Stokes/anti-Stokes asymmetry observed in standard set-ups [28].

5.2 Fast-cavity model

This section considers an alternative means to compute the split-sideband ratio derived from a cavity field that follows the mechanical motion as $\cos^2 k(x)$. This is valid if $\kappa > \omega_{\mathrm{M}}$, in which case retarded dynamical effects are negligible: the case of a “fast" cavity.

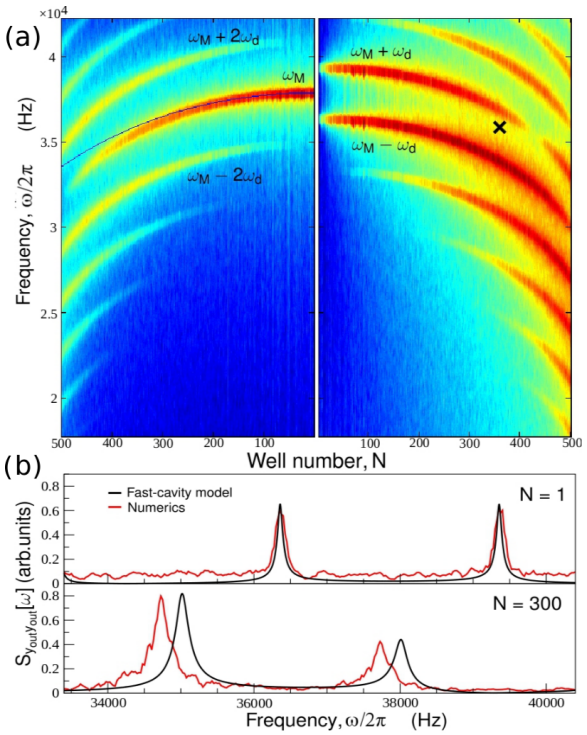

Figure 5.4: **(a)** Colormaps showing the displacement spectra (left panel $S_{\rm xx}(\omega)$) and cavity output (right panel, $S^{\rm out}_{Y_{\rm a}Y_{\rm a}}(\omega)$) for $N \in [1:500]$, obtained by numerical solution of nonlinear coupled Langevin equations. Colors indicate the noise power at each frequency. $S_{\rm xx}(\omega)$ is peaked at $\omega = \bar{\omega}_{\rm M}(N)$ which decreases with increasing N. The blue line represents the analytical Paul trap-shifted $\bar{\omega}_{\rm M}(N)$ and shows good agreement with the numerics up to $N \approx 400$. Additional weaker sidebands at $\omega \simeq \omega_{\rm M} \pm 2\omega_{\rm d}$ are also seen at higher N . In contrast, $S^{\rm out}_{Y_{\rm a}Y_{\rm a}}(\omega)$ is mainly peaked at $\omega \simeq \overline{\omega}_{\rm M} \pm \omega_{\rm d}$; For low N, a 'twin peaks' structure is seen; with increasing N an asymmetric pair develops as the $\omega \simeq \overline{\omega}_{\rm M} + \omega_{\rm d}$ peak is increasingly suppressed. We compute the asymmetry ratio using a fast-cavity model which predicts complete cancellation of $\overline{\omega}_{\rm M} + \omega_{\rm d}$ peak at $N \approx 362$ (marked by $\times$). Higher-order sidebands at $\overline{\omega}_{\rm M}(N) \pm n\omega_{\rm d}$ for odd n also appear as the frequency modulation becomes stronger. **(b)** Shows individual spectra for $N = 1$ (twin peaks) and $N = 300$ (asymmetric peaks). Numerics $\equiv$ red and analytical fits $\equiv$ black. Input power $P_{\rm in} = 0.6\,{\rm mW}$, pressure $P = 5.4 \times 10^{-2}\,{\rm mbar}$, laser detuning $\Delta = -100 \times 2\pi$ kHz, and ion trap frequency $\omega_{\rm T} \simeq 630 \times 2\pi$ Hz. Figures and captions adapted from [12].

Beginning with the linearised (classical) interaction Hamiltonian: $H^{\rm lin}_{\rm OM} = \frac{1}{2}\hbar g(t) X(t) Y_{\rm a}(t)$, where $Y_{\rm a}(t)$ is the amplitude quadrature of the cavity field. The displacement $X(t) = X_{\rm M}(t) + x_0(t)$ may be decomposed as a sum of a fast mechanical oscillation and a slow drift in the equilibrium position. The fast oscillation is $X_{\rm M}(t) \simeq X_{\rm M} \cos\Phi_{\rm M}(t)$ where $X_{\rm M}$ is the variance of the thermal motion and the accumulated phase $\Phi_{\rm M}(t) = \int_0^t \omega_{\rm M}(t')dt' = \int_0^t (\overline{\omega}_{\rm M} + 2\omega_2 \cos 2\omega_{\rm d} t')dt'$. Hence:

$$X(t) = X_{\rm M} \cos\left(\overline{\omega}_{\rm M}(N)t + \frac{\omega_2(N)}{\omega_{\rm d}} \sin 2\omega_{\rm d} t\right) + X_{\rm d} \sin\omega_{\rm d} t, \tag{5.13}$$

Substituting Eq. 5.1 and Eq. 5.13 into the interaction Hamiltonian:

$$H_{\mathrm{OM}}^{\mathrm{lin}} = \hbar\bar{g}\sin\omega_{\mathrm{d}}t\left[X_{\mathrm{M}}\cos\left(\overline{\omega}_{\mathrm{M}}t + \frac{\omega_2}{\omega_{\mathrm{d}}}\sin 2\omega_{\mathrm{d}}t\right) + X_{\mathrm{d}}\sin\omega_{\mathrm{d}}t\right]Y_{\mathrm{a}}(t). \tag{5.14}$$

Expanding the expression with Bessel and trigonometric identities, and discarding $\overline{\omega}_{\mathrm{M}}\pm 3\omega_{\mathrm{d}}$ terms,

$$\begin{aligned} H_{\mathrm{OM}}^{\mathrm{lin}} = \hbar\bar{g}Y_{\mathrm{a}}(t)X_{\mathrm{M}}\{&[J_0(\phi) - J_1(\phi)]\cdot\sin(\overline{\omega}_{\mathrm{M}} + \omega_{\mathrm{d}})t \\ &+[J_0(\phi) + J_1(\phi)]\cdot\sin(\overline{\omega}_{\mathrm{M}} - \omega_{\mathrm{d}})t\}\,, \end{aligned} \tag{5.15}$$

where J_i is the ith-order Bessel polynomial of the first kind parameterised by $\phi \equiv \frac{\omega_2}{\omega_{\mathrm{d}}}$. The optical field probes the split frequency $\overline{\omega}_{\mathrm{M}} \pm \omega_{\mathrm{d}}$ with different weights. The initial phase of the Paul trap drive is irrelevant to the asymmetry; what matters is $g(t)$ and $\omega_{\mathrm{M}}(t)$ are antiphase, which naturally follows from $H_{\mathrm{OM}}^{\mathrm{lin}}$.

The equation shows that if $J_0(\phi) = J_1(\phi)$, the coupling to the $\overline{\omega}_{\mathrm{M}} + \omega_{\mathrm{d}}$ frequency vanishes. Thus for this model one expects the ratio r to be zero if $\frac{\omega_2}{\omega_{\mathrm{d}}} \sim 1.4$, which is not too far from the prediction of the quantum model, $\frac{\omega_2}{\omega_{\mathrm{d}}} \sim 2$.

The split-sideband ratio may also be derived using a fast-cavity picture. For $\kappa > \omega_{\mathrm{M}}$, the cavity field $Y_{\mathrm{a}}(t)$ instantaneously follows the mechanical motion: $Y_{\mathrm{a}}(t) \propto \cos^2 kX(t)$; light scattered from the cavity has a similar dependence. Substituting the form for $X(t)$ from Eq. 5.13, the Fourier transform of $\cos^2 kX(t)$ may be used to calculate the cavity output PSD.

The coefficients of $\overline{\omega}_{\mathrm{M}} \pm \omega_{\mathrm{d}}$ have the ratio:

$$r = \frac{J_0[X_{\mathrm{M}}J_0(\phi)]\;J_1[X_{\mathrm{M}}J_1(\phi)] - J_0[X_{\mathrm{M}}J_1(\phi)]\;J_1[X_{\mathrm{M}}J_0(\phi)]}{J_0[X_{\mathrm{M}}J_0(\phi)]\;J_1[X_{\mathrm{M}}J_1(\phi)] + J_0[X_{\mathrm{M}}J_1(\phi)]\;J_1[X_{\mathrm{M}}J_0(\phi)]}. \tag{5.16}$$

In Fig. 5.4, the analytical results for the hybrid trap model are tested using $\bar{g} = \bar{g}(N)$ and $\overline{\omega}_{\mathrm{M}} = \overline{\omega}_{\mathrm{M}}(N)$ given by Eqs. 3.21 and 3.23.

With the simultaneous excursions in g and ω_{M}, the optical field remains equally sensitive to the split-frequency $\overline{\omega}_{\mathrm{M}}(N)\pm\omega_{\mathrm{d}}$ only when $\phi(N) = \frac{\omega_2(N)}{\omega_{\mathrm{d}}} = 0$; this happens at $N = 0$. As N increases and $\omega_2(N)$ becomes stronger, the twin-peak evolves into an asymmetric pair. In fact, one of the peaks completely vanishes when the condition $J_0(\phi) = J_1(\phi)$ is met, i.e., when $\phi(N) \approx 1.4$. This condition is seen clearly from Eq. 5.16 as well. For the parameters in Fig. 5.4, numerics indicate that complete cancellation happens at $N \approx 400$, while the fast-cavity model predicts $N \approx 362$. Note that the frequency modulation is characterised by quite a small amplitude $\omega_2 \ll \overline{\omega}_{\mathrm{M}}(N)$, so it is interesting that driving the system so far off-resonance is associated with a dramatic change in the output spectrum.

In general, sidebands of $\overline{\omega}_{\rm M} \pm n\omega_{\rm d}$, $n = 1, 3, 5, ..$ will appear for high N, as observed in Fig. 5.4. With a more sophisticated detection, these higher-order sidebands may be resolved in the experiments.

The mechanical frequency shifts by about 10%, in agreement with Eq. 3.25. For comparison $\overline{\omega}_{\rm M}(N)$ from our analytical model is indicated, showing reasonable agreement up to about $N \leq 400$. Obtaining agreement for higher $N \geq 400$ becomes increasingly challenging. One potential source of the discrepancy may be because, in using Eq. 3.24 to calculate $\overline{\omega}_{\rm M}$, $|\bar{\alpha}|^2$ has to be appropriately corrected as a result of a modified detuning (Eq. 3.20), although the modulation of Δ due to $x_0(t)$ is expected to be a minor effect, provided $\Delta \gg A$ and $\kappa \geq |\Delta|$. It is important to note that the $\overline{\omega}_{\rm M}(N)$ shifts are quite different from the usual optical spring effect seen in standard optomechanics and can be significantly larger. All approximations are tested by comparisons with the numerics which involve no linearisation: in the numerics the effective detuning, as well as $\omega_{\rm M}$ and g, are emergent properties, not input parameters.

The absence of $\Gamma_{\rm M}$ in Eq. 5.16 means the ratio persists even as the pressure is lowered. However, because quantum noises have not been included, the fast-cavity description is valid only in the thermal regime; the sideband ratio changes when quantum correlations become significant, as seen in Sec. 5.1. But, even if the quantum model may be extended to the ground-state, it is a linearised description. The fast-cavity model, while fully classical, includes all nonlinear behavior including the quadratic x^2-coupling that dominate low-N dynamics. This is not predicted by the iterative, quantum model. In the weak cooling regime, only the fast-cavity model is able to describe the nonlinear dynamics, providing a means to compute the ratio of $\omega_{\rm M} \pm \omega_{\rm d}$ to $2\omega_{\rm M}$.

5.3 Comparisons with stochastic numerics

One may test the validity and accuracy of the split-sideband ratios given by Eqs. 5.12 and 5.16 by comparing the calculated spectra with numerical solutions of equations of motion for the specific example of a levitated nanoparticle in a hybrid trap [10] since, when linearised, they reduce to the modulated optomechanics case. Comparisons are possible provided the particle motion $X(t)$ corresponds to small oscillations about an equilibrium value x_0 (which may be slowly modulated) and the cavity field dynamics $Y_{\rm a}(t)$ correspond to small fluctuations about a mean field $|\bar{\alpha}|$.

As outlined in Sec. 3.1 a nanoparticle in a hybrid electrical-optical trap experiences a dipole force potential $V_{\rm opt} = -\hbar A|a|^2 \cos^2(kx)\mathcal{F}(y,z)$ from the optical standing wave of a cavity (with axis along x). In [10], the strength of the potential $A = 26 \times 2\pi$ kHz. In the

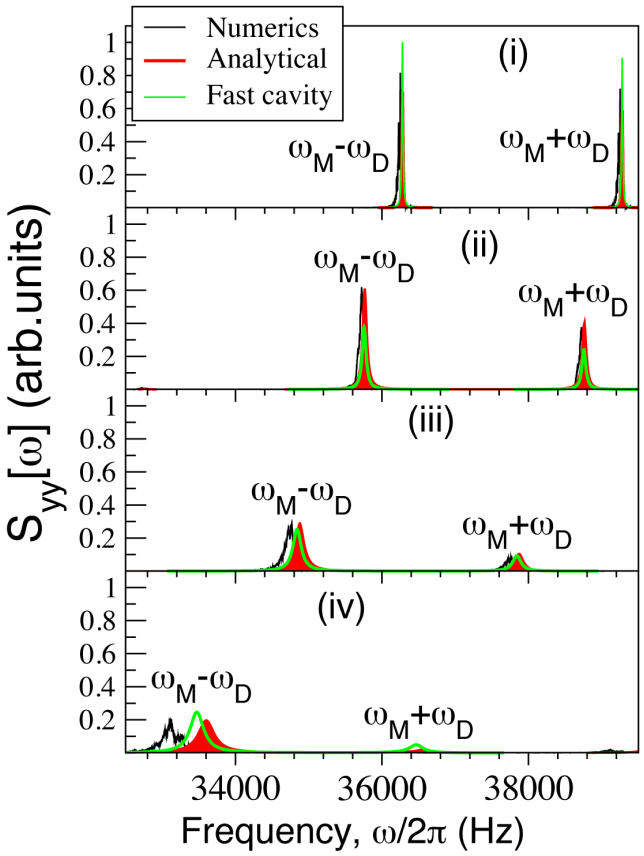

Figure 5.5: Comparison of the analytical split-sideband calculations with stochastic numerics and fast cavity model, with increasing $\bar{g}, \omega_2$ for an optically trapped particle for thermal spectra, far from the quantum limit. Here, peak heights scale with $\Gamma_{\rm M}$ and r is independent of $\Gamma_{\rm M}$. In this regime, to obtain $S_{\rm yy}(\omega)$ in units of Hz^{-1}, for arbitrary $\Gamma_{\rm M}$, graphs should be scaled as $S_{\rm yy}(\omega) \times \Gamma_{\rm M}/0.8$; in turn, for the optically trapped nanoparticles in [10], $\Gamma_{\rm M} \simeq 0.2 \times 10^4 P$, where the gas pressure ranges from $P = 1 - 10^{-8}$ mbar. $\kappa/2 = 130 \times 2\pi$ kHz, $\Delta \simeq -75 \times 2\pi$ kHz. Parameters are far from the sideband-resolved limit, so the fast-cavity model also gives reasonable results. N $= 100, 200, 300, 400$ in Eq. 3.26 hence (i) $\omega_2/2\omega_{\rm d} = 0.05$, $\bar{g} = 8500\mathrm{s}^{-1}$ (ii) $\omega_2/\omega_{\rm d} = 0.2$, $\bar{g} = 17000\mathrm{s}^{-1}$ (iii) $\omega_2/\omega_{\rm d} = 0.5$, $\bar{g} = 25000\mathrm{s}^{-1}$, (iv) $\omega_2/\omega_{\rm d} = 0.9$, $\bar{g} = 33000\mathrm{s}^{-1}$ (A typographical error in [12] has been corrected here so that: $\omega_2/2\omega_{\rm d} \to \omega_2/\omega_{\rm d}$). Figures and captions adapted from [12].

equations of motion, the particle's motion causes an effective change in the length of the cavity by modifying the detuning between the driving laser and the cavity resonance (see Eq. 3.20). Neglecting noise, the intracavity field $a(t)$ then is:

$$a(t) \approx \frac{\mathcal{E}_T}{\mathrm{i}\bar{\Delta}(t) + \kappa/2} \tag{5.17}$$

where $\mathcal{E}_T$ is the laser drive amplitude and $\bar{\Delta} = \Delta(x_0 = 0)$.

The cavity photon number $|a(t)|^2$ typically fluctuates about a mean value of $|\bar{\alpha}|^2 \approx 10^9 - 10^{10}$ photons; $k = 2\pi/\lambda$ with $\lambda = 1064$ nm. The particle becomes trapped in a given optical well N, with antinode (potential minimum) at $x = x_N$ where $2k\mathrm{x}_N = 2\pi N$. It experiences also an additional oscillating harmonic potential $V^{\rm ion}(x, y, z, t)$ from an ion

trap, whose effect is to (relatively slowly) modulate $x_0(t)$.

We test our model by comparing with numerical solutions of the equations of motion in these combined potentials, including also damping for the cavity (κ) and for mechanical degrees of freedom ($\Gamma_{\rm M}$) as well as stochastic Gaussian noise to allow for gas collisions and shot noise. This represents a stringent test of our analytical noise model since, in the numerics, $\bar{g}, \omega_{\rm M}$ and ω_2 are not input parameters: they are emergent properties of the numerical simulations. The split-sideband ratios computed using the iterative solution and fast-cavity model lead to slightly different conditions for complete sideband suppression, although both give reasonable agreement with simulations up to $\omega_2/2\omega_{\rm d} \approx 0.5$. For even higher modulations, significant contributions from higher order sidebands are not being included in the calculation, so a more accurate solution is needed. This problem is revisited in Chapter 6.

5.4 Split-sideband thermometry

The sidebands of the cavity output field in the case of a hybrid trap differ qualitatively from the standard case, with split-sideband structures seen both at low and high N. For low N (weak cooling), $S^{\rm out}_{Y_{\rm a}Y_{\rm a}}(\omega)$ has twin-peak pairs near $\omega = \pm\omega_{\rm M}$ and a further large peak at $\pm 2\omega_{\rm M}$ due to x^2 coupling to the light. For higher N (strong cooling), the split-sideband becomes asymmetric and the position-squared effects are strongly suppressed. The focus is in strong cooling, so x^2 coupling is not considered here.

A key question being tested here is whether usual procedures for inferring temperature experimentally are still reliable for these non-standard output spectra. From Eq. 5.3, in the canonical optomechanical case, the PSD of the position quadrature spectrum $S_{XX}(\omega)$ may be deduced from the cavity output (in this case exemplified by the amplitude quadrature) from the approximate relation:

$$S^{\rm out}_{Y_{\rm a}Y_{\rm a}}(\omega) \simeq g^2 |\eta(\omega)|^2 S_{XX}(\omega). \tag{5.18}$$

In the limit of long measurement time, the Wiener-Khinchin theorem connects the Fourier transform of the autocorrelation function with the power spectral density: $S_{XX}(\omega) = \left\langle |\hat{X}(\omega)|^2 \right\rangle$. The area under $S_{XX}(\omega)$ then gives the variance $\left\langle |\hat{X}|^2 \right\rangle$ which the equipartition theorem relates to temperature:

$$\frac{1}{2\pi}\int_{-\infty}^{+\infty} S_{XX}(\omega)\,{\rm d}\omega = \left\langle |\hat{X}|^2 \right\rangle = \frac{kT}{m\omega_{\rm M}}. \tag{5.19}$$

Using Eq. 5.18 and Eq. 5.19, the temperature can be extracted from a properly normalised

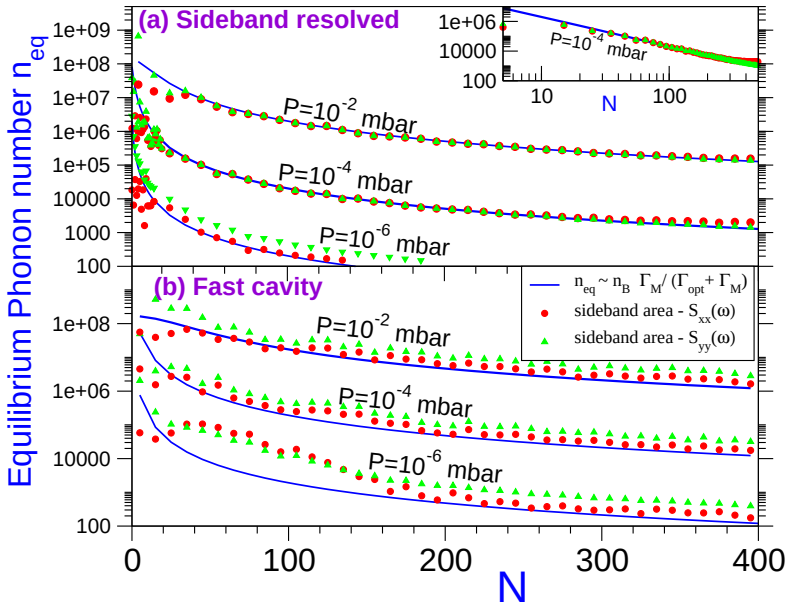

Figure 5.6: Thermometry in hybrid traps: compares final (steady state) phonon numbers inferred from the area under the sidebands of the normalised cavity output $S^{\rm out}_{Y_{\rm a}Y_{\rm a}}(\omega)/(\bar{g}^2|\eta(\omega)|^2)$ (green triangles) with those calculated directly from the displacement spectrum $S_{\rm xx}(\omega)$ (red circles). Results are given as a function of N, the optical well where the nanoparticle is trapped. The blue line represents the values using the standard optomechanical cooling formula with a period-averaged coupling $\bar{g}(N)$. Agreement between the three methods is excellent, except the very lowest few capture wells $N \leq 10$ where there is a strong contribution from the position-squared coupling term. In this case, the cavity output estimate (which integrates over both linear and nonlinear sidebands is much larger than the value estimated from $S_{\rm xx}(\omega)$. The inset shows the final phonon occupancy scales as N^{-2}. Upper panel parameters are for a high-finesse cavity $\mathcal{F} = 200,000$ which can yield ground state cooling for capture in high wells $N \geq 300-500$ for pressures $P = 10^{-6}-10^{-7}$ mbar; input power $P_{\rm in} = 0.6$ mW, laser detuning $\Delta = -70 \times 2\pi$ kHz, ion trap frequency $\omega_{\rm T} \simeq 630 \times 2\pi$ Hz. Lower panel parameters are as for Fig. 5.5. Figures and captions adapted from [12].

cavity output:

$$\frac{1}{2\pi}\int_{-\infty}^{+\infty} \frac{S^{\rm out}_{Y_{\rm a}Y_{\rm a}}(\omega)}{g^2|\eta(\omega)|^2}\,{\rm d}\omega = \frac{kT}{m\omega_{\rm M}} \tag{5.20}$$

Note that in the standard case, $S_{XX}(\omega)$ and $S^{\rm out}_{Y_{\rm a}Y_{\rm a}}(\omega)$ have very similar shapes and are peaked at $\omega_{\rm M}$. All the constant coupling parameter g does is to rescale the area under $S^{\rm out}_{Y_{\rm a}Y_{\rm a}}(\omega)$. It is implicit that the above integrals are over the mechanical sidebands only. This is especially important in the numerics or near the quantum regime since $S^{\rm out}_{Y_{\rm a}Y_{\rm a}}(\omega)$ may have a background arising from so-called imprecision noise, due to shot noise or classical laser noise. Near the quantum regime, the area of the sidebands is small and the background can contribute a significant error if the integral spans a frequency range larger

than the sideband.

For hybrid trap experiments and simulations, however, the equivalent expression to Eq. 5.18 is:

$$S^{\rm out}_{Y_{\rm a}Y_{\rm a}}(\omega) \simeq \bar{g}^2|\eta(\omega)|^2 S_{X^{\pm}X^{\pm}}(\omega), \tag{5.21}$$

as the optical field now probes the shifted displacement spectrum:
$S_{X^{\pm}X^{\pm}}(\omega) = \left\langle |\hat{X}(\omega+\omega_{\rm d}) - \hat{X}(\omega-\omega_{\rm d})|^2 \right\rangle$.

In a manner similar to 5.19, we can extract the temperature from $S_{X^{\pm}X^{\pm}}(\omega)$:

$$\frac{1}{2\pi}\int_{-\infty}^{+\infty} S_{X^{\pm}X^{\pm}}(\omega)\,{\rm d}\omega = \left\langle |\hat{X}^{\pm}|^2 \right\rangle = \frac{kT}{m\omega_{\rm M}}. \tag{5.22}$$

In the thermal regime, 5.21 relates $S_{X^{\pm}X^{\pm}}(\omega)$ to a properly normalised $S^{\rm out}_{Y_{\rm a}Y_{\rm a}}(\omega)$; 5.22 becomes

$$\frac{1}{2\pi}\int_{-\infty}^{+\infty} \frac{S^{\rm out}_{Y_{\rm a}Y_{\rm a}}(\omega)}{\bar{g}^2|\eta(\omega)|^2}\,{\rm d}\omega = \frac{kT}{m\omega_{\rm M}}. \tag{5.23}$$

In Fig. 5.6 we test Eq. 5.23 by adopting $\bar{g} = \bar{g}(N)$ specific to the hybrid trap. The temperature is obtained independently by calculating the area of $S_{XX}(\omega)$ obtained from the full stochastic numerics; this is accessible to theory but not usually to experiments measuring homodyne or heterodyne cavity spectra. This temperature is compared with that obtained from a numerical simulation of $S^{\rm out}_{Y_{\rm a}Y_{\rm a}}(\omega)$.

Additionally, the temperature (in K) is also estimated from the cooling rate in Eq. 3.27. For high N, the accuracy of Eq. 3.28 is limited by the small-angle approximations used in deriving the shifted average parameters; nonetheless, Fig. 5.6 shows good agreement, at least for high N, between the three methods: time-averaging Eq. 3.28, from the area of the sidebands of $S_{XX}(\omega)$ and of the normalised $S^{\rm out}_{Y_{\rm a}Y_{\rm a}}(\omega)$.

There are some evident discrepancies. For really low N, however, the discrepancy can be explained by noting the cavity output spectra $S^{\rm out}_{Y_{\rm a}Y_{\rm a}}(\omega)$ are dominated by the nonlinear x^2-coupling sidebands at $\omega \simeq \pm 2\omega_{\rm M}$. This sideband is not present in $S_{XX}(\omega)$; this source of error could be improved by integrating only the area under the $\omega \sim \omega_{\rm M}$ sidebands; nevertheless, care is needed for $N \leq 100$.

In the important sideband resolved case of Fig. 5.6a which can lead to ground state cooling, there are increasing discrepancies with lower pressure as the sideband area becomes small; this is partly a numerical error which requires stronger averaging by the stochastic numerics; however, the systematic overestimation of temperature by $S^{\rm out}_{Y_{\rm a}Y_{\rm a}}(\omega)$ is attributed to the contribution from the imprecision floor (from laser shot noise). With knowledge of

$\omega_{\rm M}$ this can be improved by integrating strictly only over the frequency range under the sidebands; as the mean frequency changes with N, at present the numerics integrate over a much wider frequency range than is spanned by the sidebands.

For the case of the fast cavity, there is also a systematic over-estimation of the temperature from $S^{\rm out}_{Y_{\rm a}Y_{\rm a}}(\omega)$ even at the highest pressures, where the sideband area is large and the imprecision noise contribution is negligible. This is attributed to the uncertainty in $g(N)$; The temperature depends on $g(N)^2$ so is sensitive to this value; this may indicate that the analytically computed $g(N)$ in the fast cavity dynamics is underestimated by $20-30\%$. There is also an extremely large discrepancy between the Langevin numerics and the optomechanical formula for low N; calculation of sideband area in this regime is numerically challenging: since $\Gamma_{\rm M} \propto P$, in this case, the cooling rates $\Gamma_{\rm opt}(N) \to 0$ for low N (e.g., for the experiments considered here, $\Gamma_{\rm M} \approx 0.11 \times 10^4 P$ Hz where the pressure P is in mBar). The sidebands are thus extremely narrow so the numerical estimation of the area under the sidebands becomes very difficult.

Fig. 5.6 also indicates the approximate point where $r \approx 0$ and a single peak (as opposed to a twin-peak structure) dominates the sideband structure of the cavity output. This provides a signature of high N capture. The inferred value of N represents a key source of uncertainty for experimental thermometry since N is at present inferred from the sideband shape. Fortunately for $N \gg 100$ the variation of temperature on N is sufficiently slow, that an uncertainty in $N \sim 10-50$ still allows a reasonable estimate of $g(N)$.

6 | Modulated optomechanics

This chapter presents a general matrix solution for calculating the quantum noise spectrum for periodically driven optomechanics, including multi-mode systems with arbitrary modulation in the optomechanical parameters. This is compared with a similar Floquet method [65], as well as with the iterative solution developed in Sec. 5.1. The robustness of the matrix algorithm is verified through numerics, including the two-timescale Langevin (T2SL) solutions in the quantum regime [14]. Finally, the last section discusses how the cross-correlation spectra can be accessible through proper heterodyning. This chapter has been adapted from [13].

6.1 Time-dependent Hamiltonian

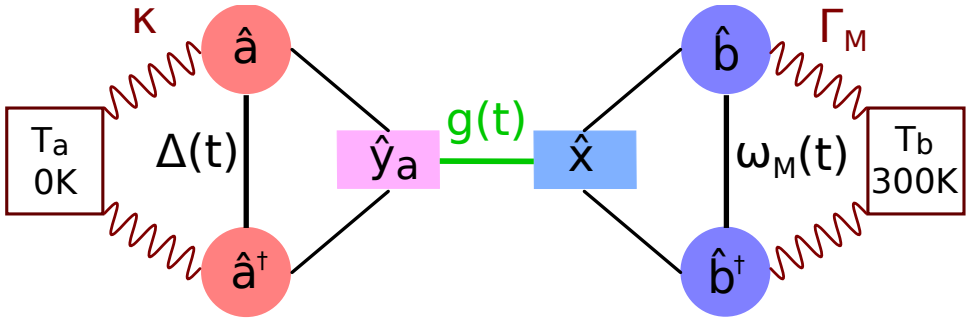

Figure 6.1: Schematic of the modulated optomechanical Hamiltonian. $\hat{a}, \hat{a}^\dagger$ and $\hat{b}, \hat{b}^\dagger$ represent the optical and mechanical modes. The optical mode is driven by a strong coherent field, resulting in a linearized optomechanical coupling g that connects the optical amplitude quadrature $\hat{y}_{\rm a}(t) = \frac{1}{\sqrt{2}}[\hat{a}(t) + \hat{a}^\dagger(t)]$ with the position quadrature $\hat{x}(t) = \frac{1}{\sqrt{2}}[\hat{b}(t) + \hat{b}^\dagger(t)]$. The system operators are coupled to their respective baths by κ for the zero-temperature optical bath, and by $\Gamma_{\rm M}$ for the mechanical bath at $300K$ leading to damping and dissipation. While for standard optomechanics $g, \omega_{\rm M}, \Delta$ are constant, the solutions investigated here are for set-ups where the paramters are harmonically modulated. Figure and caption are adapted from [13].

For compactness and generality, Eq. (2.36) can be extended into an n-mode quadratic Hamiltonian $\hat{H}(t) = \frac{1}{2}\mathbf{c}^{\mathsf{T}}(t)\mathbf{H}(t)\mathbf{c}(t)$, where the Hamiltonian *matrix* $\mathbf{H}(t)$ contains the coupling frequencies between the modes and $\mathbf{c}(t) = \begin{pmatrix}\hat{c}_1(t) & \hat{c}_1^\dagger(t) & \cdots & \hat{c}_n(t) & \hat{c}_n^\dagger(t)\end{pmatrix}^{\mathsf{T}}$ is

a vector of $2n$ system operators. The resulting Heisenberg's equation of motion is [81]:

$$\dot{\mathbf{c}}(t) = -\mathrm{i}\sigma\mathbf{H}(t)\mathbf{c}(t), \tag{6.1}$$

where $\hbar = 1$, and for bosonic ladder operators the canonical commutation relation (CCR) is

$$\sigma = [\mathbf{c}, \mathbf{c}^\dagger] = \bigoplus_{l=1}^{n} \begin{pmatrix} 1 & 0 \\ 0 & -1 \end{pmatrix}. \tag{6.2}$$

Each of the ith mode of $\mathbf{c}(t)$ is coupled to an infinite bath with rate γ_i which is described by a quantum Langevin equation:

$$\dot{\mathbf{c}}(t) = -\mathrm{i}\sigma\mathbf{H}(t)\mathbf{c}(t) - \frac{\gamma}{2}\mathbf{c}(t) + \mathbf{c}_{\mathrm{in}}(t), \tag{6.3}$$

where $\gamma = \mathsf{diag}\begin{pmatrix}\gamma_1 & \gamma_1 & \cdots & \gamma_n & \gamma_n\end{pmatrix}$, and the *scaled* input noise operators $\mathbf{c}_{\mathrm{in}}(t) \equiv \begin{pmatrix}\sqrt{\gamma}_1\hat{c}_{\mathrm{in},1}(t) & \sqrt{\gamma}_1\hat{c}^\dagger_{\mathrm{in},1}(t) & \cdots & \sqrt{\gamma}_n\hat{c}_{\mathrm{in},n}(t) & \sqrt{\gamma}_n\hat{c}^\dagger_{\mathrm{in},n}(t)\end{pmatrix}^{\mathsf{T}}$. They are Gaussian noises assumed to be delta-correlated:

$$\begin{aligned} \left\langle \hat{c}_{\mathrm{in},i}(t)[\hat{c}_{\mathrm{in},i'}(t')]^\dagger \right\rangle &= (\bar{n}_i + 1)\delta_{ii'}\delta(t-t') \\ \left\langle [\hat{c}_{\mathrm{in},i}(t)]^\dagger \hat{c}_{\mathrm{in},i'}(t') \right\rangle &= \bar{n}_i\delta_{ii'}\delta(t-t'), \end{aligned} \tag{6.4}$$

where the $2i$th element of $\mathbf{c}_{\mathrm{in}}(t)$ is denoted by $\hat{c}_{\mathrm{in},i}$. The mode occupancy $\bar{n}_i$ is set by the bath temperature. Furthermore, a matrix of noise correlations in time is defined:

$$\begin{aligned} &\left\langle \mathbf{c}_{\mathrm{in}}(t)[\mathbf{c}_{\mathrm{in}}(t')]^\dagger \right\rangle \equiv \mathbf{N}\delta(t-t') \\ &= \mathsf{diag}\begin{pmatrix}\gamma_1(\bar{n}_1+1) & \gamma_1\bar{n}_1 & \cdots & \gamma_n(\bar{n}_n+1) & \gamma_n\bar{n}_n\end{pmatrix}\delta(t-t'). \end{aligned} \tag{6.5}$$

In the case of a time-independent Hamiltonian $\mathbf{H}(t) = \mathbf{H}$, Eq. (6.1) is diagonal in Fourier space:

$$\mathbf{c}(\omega) = \mathbf{T}(\omega)\mathbf{c}_{\mathrm{in}}(\omega), \tag{6.6}$$

where the transfer matrix $\mathbf{T}(\omega) = \left(-\mathrm{i}\omega\mathbf{I} + \mathrm{i}\sigma\mathbf{H} + \frac{\gamma}{2}\right)^{-1}$, $\mathbf{I}$ is the identity matrix, and our convention for the Fourier transform is such that: $[\mathbf{c}(\omega)]^\dagger = \int_{-\infty}^{+\infty} \mathrm{d}\omega \mathrm{e}^{-\mathrm{i}\omega t}[\mathbf{c}(t)]^\dagger$ (see Appendix A.1). Equation (6.6) underlines the essence of the linear amplifier model of standard optomechanics [5]: by working in frequency space the output noises are obtained from the input noises via simple matrix inversion.

The explicit time-dependence of $\mathbf{H}(t)$ – slowly-modulated or otherwise – prevents a straightforward application of the Fourier transform to obtain a matrix equation similar

to Eq. (6.6). Nonetheless, one can apply Fourier techniques to Eq. (6.1) in two ways: (i) by Fourier-expanding the Hamiltonian matrix, or (ii) by expanding both the Hamiltonian matrix and the system operators [65]. One can then obtain a linear system either of frequency-shifted operators or of the Fourier components of the operators. In the following text the equivalence of methods (i) and (ii) is shown by deriving the power spectrum under two assumptions: 1.) input noises are Gaussian and stationary and 2.) no explicit time-dependence is introduced in the signal during detection.

6.2 Method (i): Matrix equation of shifted operators

First the periodic Hamiltonian matrix is expressed as a Fourier series: $\mathbf{H}(t) = \sum_{k\in\mathrm{Z}} \mathrm{H}_k \mathrm{e}^{\mathrm{i}k\omega_\mathrm{d}t}$. Equation (6.1) becomes

$$\dot{\mathbf{c}}(t) = \left(-\mathrm{i}\sigma \sum_k \mathrm{H}_k \mathrm{e}^{\mathrm{i}k\omega_\mathrm{d}t} - \frac{\gamma}{2}\right)\mathbf{c}(t) + \mathbf{c}_\mathrm{in}(t), \tag{6.7}$$

which in frequency space becomes

$$\left[-\mathrm{i}\omega\mathbf{I} + \frac{\gamma}{2}\right]\mathbf{c}(\omega) = -\mathrm{i}\sigma \sum_k \mathrm{H}_k \mathbf{c}(\omega + k\omega_\mathrm{d}) + \mathbf{c}_\mathrm{in}(\omega). \tag{6.8}$$

Because of the time-dependence of $\mathbf{H}(t)$ the vector $\mathbf{c}(\omega)$ depends on $\mathbf{c}(\omega + k\omega_\mathrm{d})$, preventing us from expressing Eq. (6.8) as a matrix equation similar to Eq. (6.6). Instead, the shifted equations are considered:

$$\begin{aligned}\left[-\mathrm{i}(\omega + s\omega_\mathrm{d})\mathbf{I} + \frac{\gamma}{2}\right]\mathbf{c}(\omega + s\omega_\mathrm{d}) = \\ -\mathrm{i}\sigma \sum_k \mathrm{H}_k \mathbf{c}(\omega + (k+s)\omega_\mathrm{d}) + \mathbf{c}_\mathrm{in}(\omega + s\omega_\mathrm{d})\end{aligned} \tag{6.9}$$

for each k, s. A matrix equation of the form $\mathbf{c} = \mathbf{T}\mathbf{c}_\mathrm{in}$ can then be obtained for the modulated system:

$$\begin{pmatrix} \vdots \\ \mathbf{c}(\omega{+}2\omega_\mathrm{d}) \\ \mathbf{c}(\omega{+}\omega_\mathrm{d}) \\ \mathbf{c}(\omega) \\ \mathbf{c}(\omega{-}\omega_\mathrm{d}) \\ \mathbf{c}(\omega{-}2\omega_\mathrm{d}) \\ \vdots \end{pmatrix} = \begin{pmatrix} \ddots & & \vdots & & & & \\ & \mathrm{X}(\omega{+}2\omega_\mathrm{d}) & \mathrm{A}_{-1} & \mathrm{A}_{-2} & \mathrm{A}_{-3} & \mathrm{A}_{-4} & \\ & \mathrm{A}_1 & \mathrm{X}(\omega{+}\omega_\mathrm{d}) & \mathrm{A}_{-1} & \mathrm{A}_{-2} & \mathrm{A}_{-3} & \\ \cdots & \mathrm{A}_2 & \mathrm{A}_1 & \mathrm{X}(\omega) & \mathrm{A}_{-1} & \mathrm{A}_{-2} & \cdots \\ & \mathrm{A}_3 & \mathrm{A}_2 & \mathrm{A}_1 & \mathrm{X}(\omega{-}\omega_\mathrm{d}) & \mathrm{A}_{-1} & \\ & \mathrm{A}_4 & \mathrm{A}_3 & \mathrm{A}_2 & \mathrm{A}_1 & \mathrm{X}(\omega{-}2\omega_\mathrm{d}) & \\ & & & \vdots & & & \ddots \end{pmatrix}^{-1} \begin{pmatrix} \vdots \\ \mathbf{c}_\mathrm{in}(\omega{+}2\omega_\mathrm{d}) \\ \mathbf{c}_\mathrm{in}(\omega{+}\omega_\mathrm{d}) \\ \mathbf{c}_\mathrm{in}(\omega) \\ \mathbf{c}_\mathrm{in}(\omega{-}\omega_\mathrm{d}) \\ \mathbf{c}_\mathrm{in}(\omega{-}2\omega_\mathrm{d}) \\ \vdots \end{pmatrix} \tag{6.10}$$

where the $2n \times 2n$ matrix elements are

$$\begin{aligned} \mathrm{A}_s &= \mathrm{i}\sigma \mathrm{H}_s & (6.11) \\ \mathrm{X}(\omega + s\omega_\mathrm{d}) &= -\mathrm{i}(\omega + s\omega_\mathrm{d})\mathbf{I} + \mathrm{i}\sigma \mathrm{H}_0 + \frac{\gamma}{2}. & (6.12) \end{aligned}$$

The sth row, lth column element of the transfer matrix is denoted as $\mathbf{T}_{sl}(\omega)$, with the central block being $[T^{-1}]_{00}(\omega) = X(\omega)$.

The departure point to solve the measured power spectrum analytically is:

$$S_{\mathbf{cc}^\dagger}(\omega) \equiv \lim_{T\to\infty} \left\langle \mathbf{c}(\omega)[\mathbf{c}(\omega)]^\dagger \right\rangle. \tag{6.13}$$

where the frequency-space variables are understood to be gated Fourier transforms: $\mathbf{c}(\omega) = \frac{1}{\sqrt{T}} \int_0^T \mathrm{d}t \mathrm{e}^{\mathrm{i}\omega_\mathrm{d} t} \mathbf{c}(t)$. Equation 6.13 is a $2n \times 2n$ matrix of spectra. Note that Ref. [65] offers a different way to calculate the measured spectrum but this point will be dealt with later in Sec. 6.4 C.

From Eq. (6.10), $\mathbf{c}(\omega) = \sum_{l\in\mathrm{Z}} \mathbf{T}_{0l}(\omega)\mathbf{c}_\mathrm{in}(\omega - l\omega_\mathrm{d})$. Substituting this in Eq. (6.13):

$$\begin{aligned} S_{\mathbf{cc}^\dagger}(\omega) &= \lim_{T\to\infty} \sum_{l,l'} \mathbf{T}_{0l}(\omega) \left\langle \mathbf{c}_\mathrm{in}(\omega - l\omega_\mathrm{d}) \right. \\ &\times \left. [\mathbf{c}_\mathrm{in}(\omega - l'\omega_\mathrm{d})]^\dagger \right\rangle [\mathbf{T}_{0l'}(\omega)]^\dagger & (6.14) \end{aligned}$$

It follows from Eq. (6.5) (proof in Appendix E.1) that

$$\lim_{T\to\infty} \left\langle \mathbf{c}_\mathrm{in}(\omega - l\omega_\mathrm{d})[\mathbf{c}_\mathrm{in}(\omega - l'\omega_\mathrm{d})]^\dagger \right\rangle = \mathbf{N}\delta_{ll'}. \tag{6.15}$$

Threfore,

$$S_{\mathbf{cc}^\dagger}(\omega) = \sum_{l\in\mathrm{Z}} \mathbf{T}_{0l}(\omega)\mathbf{N}[\mathbf{T}_{0l}(\omega)]^\dagger. \tag{6.16}$$

In the solution above the Hamiltonian matrix is Fourier expanded while the system operators are left as is, leading to a matrix equation of shifted operators.

6.3 Method (ii): Matrix equation of Fourier modes

In an alternative derivation [65] both the Hamiltonian matrix and the system operators are expanded in a Fourier series. Let $\mathbf{H}(t) = \sum_{k\in\mathrm{Z}} \mathrm{H}_k \mathrm{e}^{\mathrm{i}k\omega_\mathrm{d} t}$ and $\mathbf{c}(t) = \sum_{l\in\mathrm{Z}} \mathbf{c}^{(l)}(t)\mathrm{e}^{\mathrm{i}l\omega_\mathrm{d} t}$. Then starting from Eq. (6.3), the relation $\mathbf{H}(t)\mathbf{c}(t) = \sum_k H_k \mathbf{c}(t)\mathrm{e}^{\mathrm{i}k\omega_\mathrm{d} t} = \sum_k H_k \sum_l \mathbf{c}^{(l-k)}\mathrm{e}^{\mathrm{i}l\omega_\mathrm{d} t}$

is used to arrive at:

$$\sum_l \left[\dot{\mathbf{c}}^{(l)}(t) + \left(\mathrm{i}l\omega_\mathrm{d}\mathbf{I} + \frac{\gamma}{2}\right)\mathbf{c}^{(l)}(t)\right]\mathrm{e}^{\mathrm{i}l\omega_\mathrm{d}t}$$
$$= -\mathrm{i}\sigma\sum_{l,k}\left[H_k\mathbf{c}^{(l-k)}(t) + \mathbf{c}_\mathrm{in}(t)\delta_{l,0}\right]\mathrm{e}^{\mathrm{i}l\omega_\mathrm{d}t}. \tag{6.17}$$

A quantum Langevin equation is identified for each Fourier mode:

$$\left[-\mathrm{i}(\omega - l\omega_\mathrm{d})\mathbf{I} + \frac{\gamma}{2}\right]\mathbf{c}^{(l)}(\omega)$$
$$= -\mathrm{i}\sigma\sum_k H_k\mathbf{c}^{(l-k)}(\omega) + \mathbf{c}_\mathrm{in}(\omega)\delta_{l,0}, \tag{6.18}$$

Here stationary input noises are assumed and placed into the zeroth Fourier component. In general, periodic input noises can be treated as well [82]. The coupled quantum Langevin equations can be written as an infinite-dimensional matrix equation:

$$\begin{pmatrix} \vdots \\ \mathbf{c}^{(-2)}(\omega) \\ \mathbf{c}^{(-1)}(\omega) \\ \mathbf{c}^{(0)}(\omega) \\ \mathbf{c}^{(1)}(\omega) \\ \mathbf{c}^{(2)}(\omega) \\ \vdots \end{pmatrix} = \begin{pmatrix} \ddots & & \vdots & & & & \\ & \mathrm{X}(\omega+2\omega_\mathrm{d}) & \mathrm{A}_{-1} & \mathrm{A}_{-2} & \mathrm{A}_{-3} & \mathrm{A}_{-4} & \\ & \mathrm{A}_1 & \mathrm{X}(\omega+\omega_\mathrm{d}) & \mathrm{A}_{-1} & \mathrm{A}_{-2} & \mathrm{A}_{-3} & \\ \cdots & \mathrm{A}_2 & \mathrm{A}_1 & \mathrm{X}(\omega) & \mathrm{A}_{-1} & \mathrm{A}_{-2} & \cdots \\ & \mathrm{A}_3 & \mathrm{A}_2 & \mathrm{A}_1 & \mathrm{X}(\omega-\omega_\mathrm{d}) & \mathrm{A}_1 & \\ & \mathrm{A}_4 & \mathrm{A}_3 & \mathrm{A}_2 & \mathrm{A}_1 & \mathrm{X}(\omega-2\omega_\mathrm{d}) & \\ & & \vdots & & & & \ddots \end{pmatrix}^{-1} \begin{pmatrix} \vdots \\ 0 \\ 0 \\ \mathbf{c}_\mathrm{in}(\omega) \\ 0 \\ 0 \\ \vdots \end{pmatrix}, \tag{6.19}$$

with the same transfer matrix as in Eq.(6.10). The Fourier components are sometimes referred to as sidebands or introduced as "auxiliary" modes [83].

From Eq. (6.19), the lth Fourier mode $\mathbf{c}^{(l)}(\omega) = \mathbf{T}_{l0}(\omega)\mathbf{c}_\mathrm{in}(\omega)$, so $\mathbf{c}(\omega) = \sum_{l\in\mathrm{Z}}\mathbf{c}^{(l)}(\omega + l\omega_\mathrm{d})$. Reference [65] constructs the spectrum from the Fourier modes, where the role of the Kronecker delta correlation in Eq. (17) is played by matching of equal and opposite Fourier indices. Here, Eq. (6.13) is used to calculate the measured power spectrum:

$$\begin{aligned} S_{\mathbf{cc}^\dagger}(\omega) &= \lim_{T\to\infty}\sum_{l,l'}\mathbf{T}_{l0}(\omega + l\omega_\mathrm{d})\left\langle\mathbf{c}_\mathrm{in}(\omega + l\omega_\mathrm{d})\right. \\ &\times \left.[\mathbf{c}_\mathrm{in}(\omega + l'\omega_\mathrm{d})]^\dagger\right\rangle[\mathbf{T}_{l'0}(\omega + l'\omega_\mathrm{d})]^\dagger \end{aligned} \tag{6.20}$$

Using the Kronecker delta correlation in Eq. (6.15):

$$S_{\mathbf{cc}^\dagger}(\omega) = \sum_{l\in\mathrm{Z}}\mathbf{T}_{l0}(\omega + l\omega_\mathrm{d})\mathbf{N}[\mathbf{T}_{l0}(\omega + l\omega_\mathrm{d})]^\dagger. \tag{6.21}$$

The infinite matrix $\mathbf{T}$ and its inverse have diagonals that are invariant (up to a frequency

displacement) with respect to an equal shift in the row and column indices:

$$\mathbf{T}_{ll}(\omega) = \mathbf{T}_{l+n,l+n}(\omega + n\omega_{\mathrm{d}}). \tag{6.22}$$

This translation property of $\mathbf{T}$ is a crucial feature that will be invoked throughout the paper. Shifting the indices of Eq. (6.21) by $-l$, Eqs. (6.16) and (6.21) are equivalent. Therefore, methods (i) and (ii) yield equivalent power spectra, a key result of this chapter.

6.4 Simulation of split-sideband spectra

In this section the expressions for methods (i) and (ii) are tested and verified, as well the iterative solution in Sec. 5.1 — called method (iii) — against a numerical solution of the stochastic Langevin equations. Methods (i) and (ii) yield indistinguishable results. Both solutions show the same convergence properties in that they need to be truncated at a higher order as the modulations become stronger. To ensure invertibility and convergence, the matrix in Eq. (6.10) is truncated at an arbitrarily high odd dimension (17×17 block matrices).

For the numerics, a set of stochastic Langevin equations is explicitly solved corresponding to the semiclassical dynamics of the system where each operator in Eq. (E.3) is replaced with its (in general complex) expectation value and its adjoint with the corresponding complex conjugates. The stochastic noises c_{in} have a Gaussian distribution with an average variance equal to the step size in the temporal propagation, such that $\left\langle c_{\mathrm{in},i}(t)c^*_{\mathrm{in},i'}(t')\right\rangle = \left\langle c^*_{\mathrm{in},i}(t)c_{\mathrm{in},i'}(t')\right\rangle = 2\pi(\bar{n}+1/2)\delta_{i,i'}\delta(t-t')$.

6.4.1 Split-sideband spectra in the strong modulation regime

Figure 6.2 compares methods (i)/(ii) with method (iii) as well as with the numerical simulation of the intracavity spectrum of the doubly-modulated system exhibiting the characteristic split-sideband separated by $2\omega_{\mathrm{d}}$ about ω_{M}. To compare with previous studies [12], each spectrum is parameterized by both g and ω_2. As was previously observed [12], the ratio of the split-sidebands change as the parameter $\omega_2/\omega_{\mathrm{d}}$ increases. Up to $\omega_2/\omega_{\mathrm{d}} = 0.9$, all the three spectra exhibit progressively suppressed $\omega_{\mathrm{M}} + \omega_{\mathrm{d}}$ peak, and all show good agreement. From this point onward, however, the iterative solution fails to change the split-sideband ratio, while the full solution matches very well with the numerics, even going past the complete suppression point at $\omega_2/\omega_{\mathrm{d}} \approx \sqrt{2}$. This behaviour can also be seen in Fig. 6.2b which plots the ratio of the split-sidebands as g and ω_2 increases. Fig. 6.2c also verifies the split-sideband ratio persists regardless of the cooperativity and is only

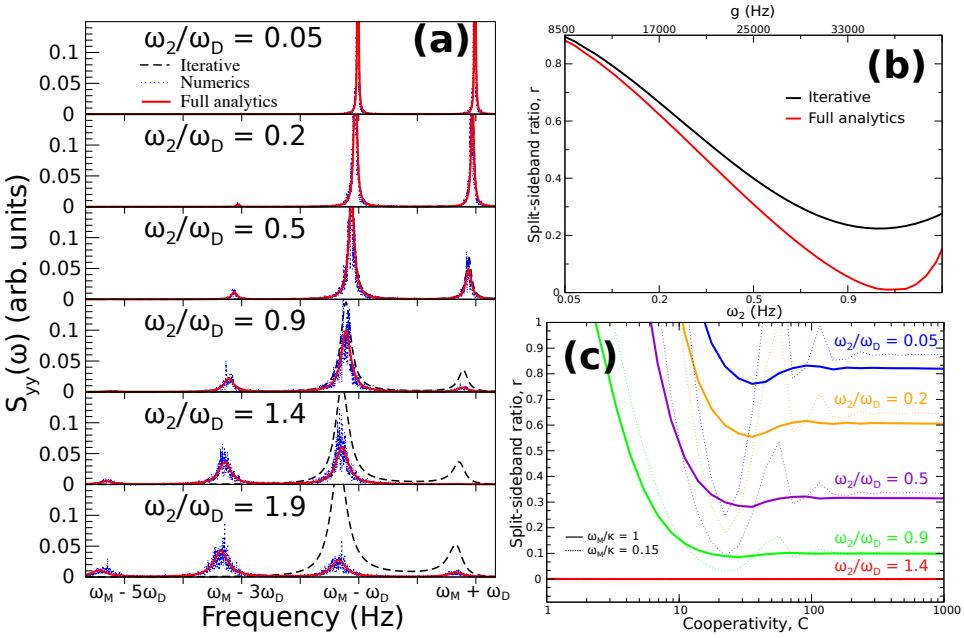

Figure 6.2: **a.)** Comparison of the full analytical solution (red, solid) with the iterative solution (black, dashed) of the cavity spectrum $S_{\rm yy}(\omega)$ for different values of $\omega_2/\omega_{\rm d}$, with $\omega_{\rm d}$ fixed. The stochastic numerics (blue, dotted) are obtained by solving the first-order coupled Langevin equations using XMDS2. There is good agreement among the three, where we see one of the twin peaks is progressively suppressed, until around $\omega_2/\omega_{\rm d} = 0.9$, where from this point onward the iterative solution fail to show further suppression. The full analytical spectra, on the other hand, agree very well with numerics - even showing higher-order sidebands. Parameters are: $\omega_{\rm d}/\omega_{\rm M} = 0.05$, $\Delta_2 = 0$, $\bar{n}_{\rm b} = \frac{k}{\hbar\omega_{\rm M}} 300K$. **b.)** Sideband ratio vs. g and $\omega_{\rm M}$ for the same system in **(a)**. Note the full analytical solution (red, lower) achieves the suppression point, after which the ratio bounces back to $R > 0$ as $\omega_2/\omega_{\rm d}$ is further increased. The g in **(a)** changes with each $\omega_2/\omega_{\rm d}$ and is given here in the alternative axis. **c.** Split-sideband ratio vs. cooperativity $C = \frac{4g^2}{\kappa\Gamma_{\rm M}}$ for $\omega_2/\omega_{\rm d} = 0.05$, 0.2, 0.5, 0.9, and 1.4; and for both sideband-resolved (solid, $\omega_{\rm M}/\kappa = 1$) and otherwise (dotted, $\omega_{\rm M}/\kappa = 0.15$). Parameters are: $\omega_{\rm d}/\omega_{\rm M} = 0.05$, $\Delta_2 = 0$, $\bar{n}_{\rm b} = \frac{k}{\hbar\omega_{\rm M}} 300K$. Split-sideband resolution is ensured by the condition $\Gamma_{\rm opt} \ll 2\omega_{\rm d} \leftrightarrow \frac{C\Gamma_{\rm M}}{2\omega_{\rm d}} \ll 1$. Figures and captions are adapted from [13].

determined by $\omega_2/\omega_{\rm d}$. Depending on $\kappa/\omega_{\rm M}$, the split-sideband ratio may fluctuate before reaching a constant value. The higher the $\omega_2/\omega_{\rm d}$ the lower cooperativity is required to reach a constant ratio, so at the suppression point $r \approx 0$ for all C. Split sidebands are ensured to be well-resolved by choosing $\Gamma_{\rm opt} \ll 2\omega_{\rm d}$.

A new result of the comparison with the full Fourier methods (i/ii) is to provide a more accurate value of the point at which the second sideband is fully suppressed: here the suppression point is observed at $\omega_2/\omega_{\rm d} \approx \sqrt{2}$. An earlier analysis based on the approximate method (iii) gives $\omega_2/\omega_{\rm d} \sim 2$ [12]; however, that analysis of the low order iterative solution neglected the modification to the susceptibilities due to higher-order backactions. The second sideband remains very weak across the entire $\omega_2/\omega_{\rm d} \sim 1$ to 2 range so the underlying physical explanation remains valid. Curiously, the fast-cavity model, which uses a Bessel expansion of the modulations in the interaction Hamiltonian presented in Sec. 5.2, also

predicted the more accurate $\omega_2/\omega_\mathrm{d} \approx \sqrt{2}$ result.

6.4.2 Optical squeezing in homodyne spectra

Measured spectra detect the cavity output spectrum $\hat{a}_\mathrm{out}(\omega) = \hat{a}_\mathrm{in} - \sqrt{\kappa}\hat{a}(\omega)$, presenting additional interesting effects arising from correlations between the incoming noise and the intracavity field due to quantum backaction. In particular such correlations give rise to ponderomotive squeezing and power spectrum values below the shot-noise floor near $\omega \approx \omega_\mathrm{M}$.

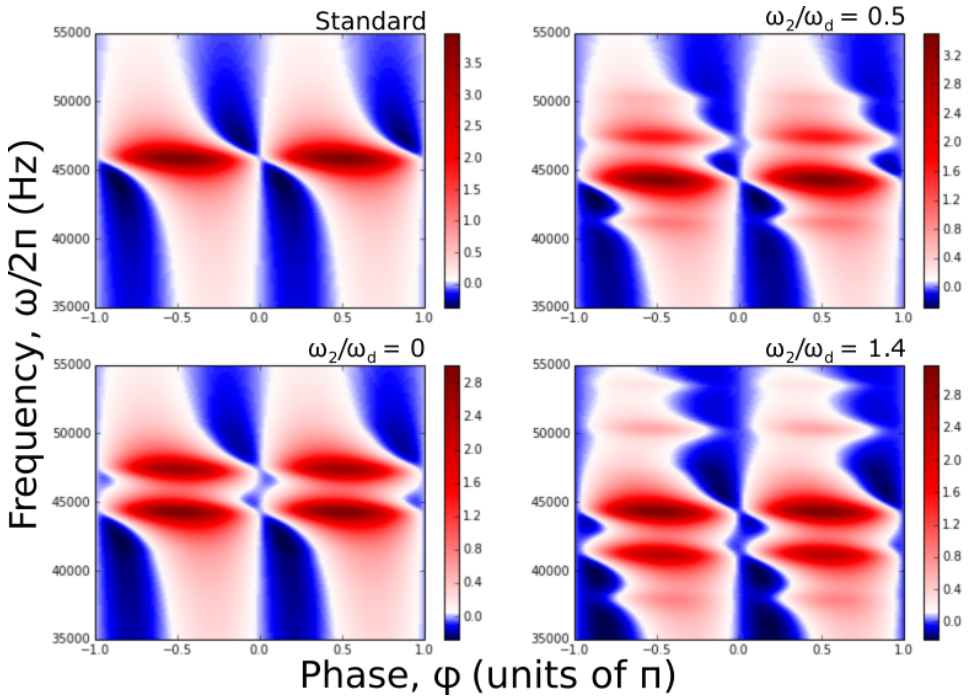

Figure 6.3: Color map of the homodyne spectra $S^{\phi}_{\mathrm{hom}}(\omega)$ versus the local oscillator (LO) angle ϕ for the standard case, as well as the slowly-modulated cases with varying $\omega_2/\omega_\mathrm{d}$. $g = 18.5$ kHz. Two optical modes are used: the cooling mode at $\Delta = -\omega_\mathrm{M}$ brings down the phonon occupation from 300 K to $\bar{n}_\mathrm{b} < 1$ while the probe mode at $\Delta_\mathrm{p} = 0$ is used for readout. Both are at $\bar{n}_\mathrm{a} = 0$ and $\Gamma_\mathrm{M} = 2.3 \times 10^{-5}$. The blue (red) region indicate noise below (above) the imprecision floor. A flat spectrum is obtained for the amplitude quadrature ($\phi = 0$), while a twin-peak around ω_M for the phase quadrature $\phi = \pi/2$. The colormaps are shown for the standard case, as well as for the slowly-modulated case for three different $\omega_2/\omega_\mathrm{d}$. Aside from familiar regions of squeezing characteristic to standard optomechanics, squeezing between the twin-peaks is also seen. Maximum squeezing at ≈ 1 dB (20% below the noise floor) is achieved at $\phi = \pi/4$. At the suppression point $\omega_2/\omega_\mathrm{d} \approx \sqrt{2}$ regions of high backaction noise (red) are replaced by squeezing. The rest of parameters are the same as in Fig. 6.2a. Figures and captions are adapted from [13].

The measured homodyne spectrum detects a single optical quadrature:

$$i_\mathrm{hom}(t) = e^{i\phi}\hat{a}_\mathrm{out}(t) + e^{-i\phi}a^{\dagger}_\mathrm{out}(t) \tag{6.23}$$

and hence the measured power spectrum $S_{\rm hom}(\omega) = \langle |i_{\rm hom}(\omega)|^2 \rangle$, has four components:

$$\begin{aligned} S_{\rm hom}(\omega) &= \left\langle \hat{a}_{\rm out}(\omega)[\hat{a}_{\rm out}(\omega)]^\dagger \right\rangle + \left\langle [\hat{a}_{\rm out}(\omega)]^\dagger \hat{a}_{\rm out}(\omega) \right\rangle \\ &+ \langle \hat{a}_{\rm out}(\omega)\hat{a}_{\rm out}(\omega)\rangle \, {\rm e}^{2{\rm i}\phi} + \left\langle [\hat{a}_{\rm out}(\omega)]^\dagger [\hat{a}_{\rm out}(\omega)]^\dagger \right\rangle {\rm e}^{-2{\rm i}\phi}, \end{aligned} \tag{6.24}$$

where ϕ is the local oscillator phase ($\phi = 0$ for amplitude, and $\phi = \pi/2$ for phase quadrature).

Another advantage of the linear amplifier matrix formalism is that outputs the full covariance matrix, facilitating calculation of the homodyne spectra which are constructed from several separate components. Usually, a probe mode different from the control beam is used for detection. When probe coupling is weak and $\Delta_{\rm p} = 0$ it does not alter system dynamics but otherwise the probe could significantly couple to the oscillator motion regardless of the quadrature being measured. The matrix methods are extendable to any number of modes so probe dynamics can be easily integrated.

Figure 6.3 shows the color map of the quantum homodyne spectra for the standard case, as well as the modulated case for three different modulation strengths. Large regions of squeezing of up to ≈ 1 dB (20 % below the noise floor) can be observed for $0 < \phi < \pi/2$. The matrix method correctly replicates the squeezing profile of the standard case [37]. As expected for an on-resonance probe, the optical field shows no peaks at $\phi = 0$ while coupling most strongly with the mechanical oscillator at $\phi = \pi/2$. Optical squeezing at the mechanical frequency is impossible to see in standard optomechanics through homodyne detection, so sensing on-resonance will always be degraded by back-action noise, unless one performs a synodyne detection [75], or introduce modulations within the system [60, 62].

Adding a slow modulation in $g(t)$ allows the measurement of the cross-correlation $\langle \hat{x}(\omega + \omega_{\rm d})\hat{x}(\omega - \omega_{\rm d})\rangle$ that causes squeezing between the twin peaks. Introducing an additional periodicity in $\omega_{\rm M}(t)$ at $2\omega_{\rm d}$ further increases the contribution of the cross-correlation. The result is a squeezed region that grows with $\omega_2/\omega_{\rm d}$ until it completely suppresses back-action noise (red) on resonance for $\omega_2/\omega_{\rm d} \approx \sqrt{2}$. Such optical squeezing have been demonstrated for resonantly modulated optomechanical systems, but off-resonant modulated optomechanical systems could possibly offer a novel way of exploiting cross-correlations for quantum sensing.

6.4.3 Sub-shot noise dynamics

To further verify the analytical results, a comparison of the homodyne PSD of a slowly-modulated system is made with numerical solutions obtained from two-timescale stochastic Langevin (T2SL). T2SL extends the stochastic Runge-Kutta method by considering dif-

ferent timescales for the deterministic and stochastic evolutions. Recall that the cavity output contains non-trivial correlations between the input and intracavity fields: $\hat{a}_{\rm out}(t) = \hat{a}_{\rm in}(t) - \sqrt{\kappa}\hat{a}(t)$. Because the noises are delta-correlated $\left\langle \hat{a}_{\rm in}(t)\hat{a}^{\dagger}_{\rm in}(t')\right\rangle = \delta(t-t')$, it is crucial to store the state every time a stochastic kick is applied if one hopes to capture fragile correlations in the cavity output. However, the data array size becomes unmanageable if a stochastic term is added for every Runge-Kutta increment. The solution is then to consider propagating deterministically for a certain time-interval before applying stronger, but less frequent stochastic increments. This is valid because the standard deviations of Gaussian noises are additive. For more exotic types of noises, T2SL may not then be valid, although this is beyond the scope of the study.

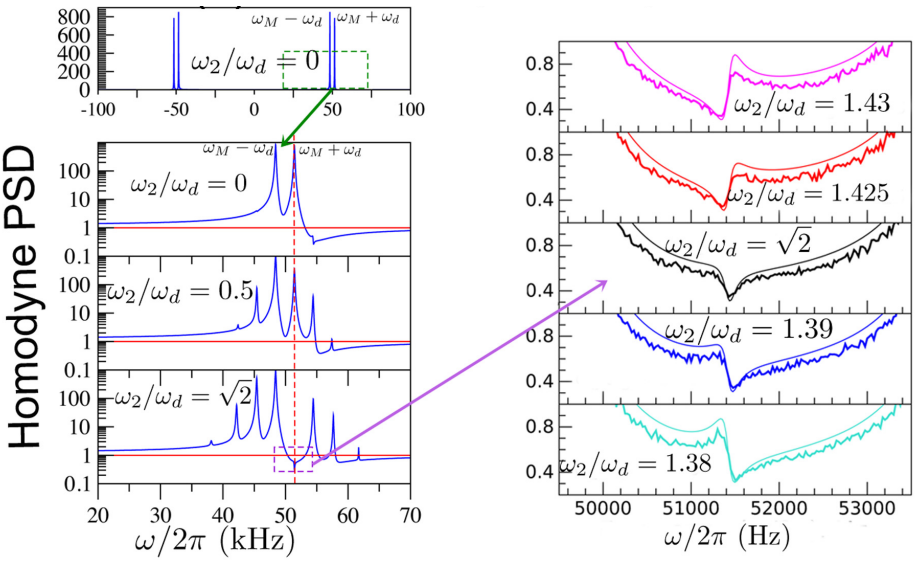

Figure 6.4: Analytical homodyne PSD for a slowly-modulated optomechanical system for different $\omega_2/\omega_{\rm d}$. Near the complete suppression condition $\omega_2/\omega_{\rm d} = \sqrt{2}$, the Fano-like peaks flip in orientation. Such detail agreed very well with two-timescale stochastic Langevin (T2SL), which allows classical numerical solutions of the cavity output spectra in the quantum regime, even in the presence of nonlinearities [14]. Figure is adapted from [14].

Figure 6.4 illustrates the excellent agreement between analytical and T2SL solutions in the quantum regime, where a flipping of the Fano-like mechanical sideband happens around the suppression condition $\omega_2/\omega_{\rm d} \approx \sqrt{2}$. Note that T2SL is a fully classical simulation of quantum dynamics. A finer explanation of the types of quantum features that can be simulated by T2SL can be found in [14].

6.5 Discussion

Although both methods (i) and (ii) give the same results for both intracavity and homodyne-detected power spectra, this section now investigates whether the equivalence holds for

more general types of spectra. In particular, the heterodyne detection of modulated optomechanical systems is discussed.

6.5.1 Connections between methods (i) and (ii)

In summary, for both methods a set of output field modes is obtained from a set of input noises by the action of a transfer matrix $\mathbf{T}$. However, in method (i) the output field operator $\mathbf{c}(\omega)$ originates from multiple, frequency-shifted input noise components $c_{\rm in}(\omega + l\omega_{\rm d})$. In method (ii), in contrast, the dynamical operators were decomposed into a Fourier series $\mathbf{c}(t) = \sum_{l\in \rm Z} \mathbf{c}^{(l)}(t)\mathrm{e}^{\mathrm{i}l\omega_{\rm d}t}$. In this case these components $\mathbf{c}^{(l)}(\omega + l\omega_{\rm d})$ originate from the effect of the transfer matrix on a *single* input noise component $c_{\rm in}(\omega)$.

To investigate these differences, the measured power spectra Eq. (6.13) is rewritten in terms of the autocorrelation function [3]:

$$\begin{aligned}
&\lim_{T\to\infty} \left\langle \mathbf{c}(\omega)[\mathbf{c}(\omega)]^\dagger \right\rangle \\
&\equiv \lim_{T\to\infty} \frac{1}{T}\int_0^T \mathrm{d}t \int_0^T d\tau \mathrm{e}^{\mathrm{i}\omega\tau} \left\langle \mathbf{c}(t+\tau)[\mathbf{c}(t)]^\dagger \right\rangle \\
&= \lim_{T\to\infty} \frac{1}{T}\int_{-T/2}^{T/2} \mathrm{d}t S(\omega, t)
\end{aligned} \tag{6.25}$$

where $S(\omega, t)$ is defined as the Fourier transform of the autocorrelation function. For an ordinary (unmodulated) optomechanical system, the stationarity (i.e. time-translation invariance) of the stochastic process leads to the Wiener-Khinchin theorem:
$\lim_{T\to\infty} \left\langle \mathbf{c}(\omega)[\mathbf{c}(\omega)]^\dagger \right\rangle = S(\omega)$ (independent of t).

In method (ii), the periodic modulation of the $\mathbf{c}(t)$ naturally implies the periodic modulation of $S(\omega, t)$:

$$S(\omega, t) = \sum_{l\in \rm Z} S^{(m)}(\omega)\mathrm{e}^{\mathrm{i}m\omega_{\rm d}t} \tag{6.26}$$

and in [65] it was shown that the measured spectrum is the zeroth-order component $S^{(0)}(\omega)$.

Although the higher order spectral terms $S^{(m)}(\omega)$ appear to be experimentally inaccessible, we show below that these $|m| > 0$ contributions may be measured using heterodyne detection with a beat frequency $2\Omega = n\omega_{\rm d}$ resonant with the modulation. Hence the question arises as to how they can be calculated. It has been shown that $S^{(m)}(\omega)$ can be computed from the Fourier components of the operator using method (ii) [65]. In Appendix E.3 we show that the higher spectral components are, in fact, straightforwardly related to cross-correlations between the method (i) operators:

$$\lim_{T\to\infty} \left\langle \mathbf{c}(\omega)[\mathbf{c}(\omega + m\omega_{\rm d})]^\dagger \right\rangle = S^{(m)}(\omega) \tag{6.27}$$

and hence higher order components of the spectrum are also obtainable from method (i).

6.5.2 Measuring non-stationary spectrum components with heterodyne detection

Heterodyne detection measures a rotating quadrature:

$$i_{\text{het}}(t) = e^{i\phi+\Omega t}\hat{a}_{\text{out}}(t) + e^{-i(\phi+\Omega t)}a^{\dagger}_{\text{out}}(t) \tag{6.28}$$

and we take $\phi = 0$ as the power spectrum is in general insensitive to ϕ. Hence, in frequency space, $i_{\text{het}}(\omega) = \hat{a}_{\text{out}}(\omega+\Omega) + [\hat{a}_{\text{out}}(\omega-\Omega)]^{\dagger}$.

In getting the power spectrum $S_{\text{het}}(\omega) = \lim_{T\to\infty}\left\langle |i_{\text{het}}(\omega)|^2\right\rangle$, intuition suggests that only the terms correlated at the same frequency will survive while the cross-correlations will vanish. Another way to look at this is through the time domain, where the heterodyne signal in time will give rise to a time-dependent autocorrelator, and the cross terms carrying $\pm e^{2i\Omega t}$ will get averaged out in the Fourier transform [65]. Both viewpoints regarding the cancellation of cross correlations rely on the crucial fact that the noises are delta-correlated. However, on closer inspection, the cross correlations $\langle\hat{a}_{\text{out}}(\omega-\Omega)\hat{a}_{\text{out}}(\omega+\Omega)\rangle$ and $\left\langle[\hat{a}_{\text{out}}(\omega+\Omega)]^{\dagger}[\hat{a}_{\text{out}}(\omega-\Omega)]^{\dagger}\right\rangle$ can indeed be measured if the local oscillator frequency Ω is chosen appropriately. This is easy to show using method (i):

$$\begin{aligned}
&\lim_{T\to\infty}\left\langle \mathbf{c}(\omega+\Omega)[\mathbf{c}(\omega-\Omega)]^{\dagger}\right\rangle \\
&= \lim_{T\to\infty}\sum_{l,l'\in\mathbf{Z}}\mathbf{T}_{0l}(\omega+\Omega)\left\langle \mathbf{c}_{\text{in}}(\omega+l\omega_{\text{d}}+\Omega)\right. \\
&\times\left.[\mathbf{c}_{\text{in}}(\omega+l'\omega_{\text{d}}-\Omega)]^{\dagger}\right\rangle[\mathbf{T}_{0l'}(\omega-\Omega)]^{\dagger} \\
&= \sum_{l\in\mathbf{Z}}\mathbf{T}_{0l}(\omega+\Omega)\mathbf{N}[T_{0,l+n}(\omega-\Omega)]^{\dagger}
\end{aligned} \tag{6.29}$$

The noise correlation in Eq. (6.5) forces $l' = l+n$, and also $n \equiv \frac{2\Omega}{\omega_{\text{d}}} \in \text{Z}$. Such cross-correlations are useful in quantum sensing [64, 75], and Eq. (6.29) illuminates the interesting fact that, by introducing an appropriate phase reference Ω – whether intrinsic to the system, or externally – it becomes possible that a delta-correlated input noise (which vanishes if $\omega \neq \omega'$) can give rise to a non-zero correlation of output noises at different frequencies. In particular, cross-correlations (and hence, rotating parts of the cavity output spectrum) can be recovered naturally in modulated systems using heterodyne detection. The same idea has been applied on the level of rotating *mechanical* quadratures using the Fourier components of the periodic spectrum [65] which, from Appendix E.3, are equivalent to unequal-frequency cross correlations of shifted operators.

7 | Summary and Conclusions

In summary, this thesis presented a general analysis of levitated optomechanical systems with periodically driven fields. In levitated schemes, the particle's position x_0 in the optical well crucially determines the optomechanical interaction and dynamics. With only optical gradient forces, the particle settles at the antinode where the quadratic coupling is weak. However, by adding a time-periodic auxilliary field, the particle does an approximately harmonic excursion $x_0(t)$ across the optical well, and cyclically samples the linear region of the optical potential where the optomechanical coupling is strong.

This general picture has been useful for modelling the dynamics of a levitated particle in the combined cavity and Paul trap potentials. The hybrid nature of the trap manifests in the mutual frequency shifts, which are helpful in estimating unknown experimental parameters (such as the optomechanical cooling rate) from simultaneous readouts of mechanical frequency ω_{M} and secular frequency ω_{S}. The Paul trap proves to be more than just a passive trapping field — it is indispensable for particle cooling. With the addition of the Paul trap, stable trapping up to 10^{-5} mbar at high N resulted in strong cavity cooling of the nanoparticle at $\sim 1000\mathrm{s}^{-1}$, showing 1000-fold reduction in the steady-state phonon occupation from room temperature. The area under a single sideband decreases proportionally with pressure, as expected from a linear optomechanical cooling. Scattered light shows evidence of trapping up to 10^{-6} mbar, with a possibility of ground state cooling at 10^{-7} mbar, though a more sensitive detection is required to improve signal-to-noise ratio. The low well N catch showed nonlinearities: twin-peak spectra around ω_{M} together with a dominant $2\omega_{\mathrm{M}}$, which indicates that optical gradient forces prevail over the Paul trap. Quadratic coupling offers optomechanical cooling, preparation of macroscopic quantum states, and quantum non-demolition measurement of energy — sought after for phonon counting experiments — although the zero-point fluctuations at the antinode are very small that the single phonon coupling is notororiously weak. A study of the transient response of a particle trapped in a high well N showed 2x faster damping of the quadratic versus the linear sideband.

Nonlinear, stochastic simulations of the full 3D dynamics of the particle reveal an N -

dependence of the sideband spectra: as the trapping well N goes higher, the twin-peaks evolve into an asymmetric pair of mechanical sidebands split by $\omega \pm \omega_{\rm d}$. This behavior is, in fact, not exclusive to the hybrid trap — it is generic to periodically driven levitated systems. A harmonic excursion in the particle's equilibrium position cause simultaneous, out-of-phase modulations in the optomechanical coupling $g = 2\bar{g}\sin\omega_{\rm d}t$ and mechanical frequency $\omega_{\rm M} = \overline{\omega}_{\rm M} + 2\omega_2\cos\omega_{\rm d}t$, with $\bar{g}$ and ω_2 proportional to the amplitude of modulation in the equilibrium position $x_0(t)$. The split-sideband asymmetry can also be understood via frequency space: because of $g(t)$, the optical field probes the shifted displacement spectra $\langle\hat{x}(\omega+\omega_{\rm d} - \hat{x}(\omega-\omega_{\rm d})\rangle^2$ instead. With $\omega_2 = 0$, the interference term can be neglected, resulting in a twin-peak spectra. However, as $\omega_{\rm M}(t)$ grows, the correlation spectra leads to a constructive interference in one of the split-sidebands, and destructive interference in the other. The split-sideband ratio r can be derived analytically by (1) solving the shifted quantum Langevin equations iteratively and (2) via a fast-cavity solution using Bessel functions. Expressions for $g(N,t)$ and $\omega_{\rm M}(N,t)$ are obtained explicitly for the hybrid trap experiment for comparison with stochastic numerics — for small backaction, analysis and numerics have good agreement. Stochastic simulations also allowing estimation of the system's center-of-mass temperature from the split-sideband area. Understanding split-sideband spectroscopy is useful not only for thermometry in periodically driven levitated systems, but also as an additional signature of the quantum limit: the split-sideband ratio remains constant with decreasing pressure but changes shape because of ponderomotive squeezing around the suppressed peak.

A distinctive feature of doubly-modulated optomechanics is the $r = 0$ condition: one of the split-sidebands become completely suppressed and squeezed in the quantum regime. This happens for strong modulations for which neither the iterative and fast-cavity solutions yield a definitive conclusion. To investigate the strong modulation regime, a matrix algorithm using shifted noises (method i) is derived to solve the quantum noise spectra of periodically modulated optomechanical systems. We compare this with a similar Floquet approach (method ii) [65] and the iterative solution (method iii). Methods (i) and (ii) give equivalent spectra, while method (iii), is an analytical approximation to method (i). The equivalent methods (i)/(ii) are compared with Langevin stochastic simulations of the doubly-modulated optomechanical Hamiltonian. The previously unexplored regime of slow but strong modulations in the optomechanical coupling and mechanical frequency provide a stringent test of the analytical methods. Methods (1)/(ii) demonstrate excellent agreement, confirming split-sideband suppression at $\omega_2/\omega_{\rm d} \approx \sqrt{2}$. Method (iii), being effectively a low-order truncation of the transfer matrix of method (i), also shows good agreement up to a certain modulation amplitude. *Resonant* squeezing in the quantum regime is pre-

dicted for the doubly-modulated system as a result of enhanced cross-correlations in the shifted mechanical spectrum when $\omega_2/\omega_\mathrm{d} \approx \sqrt{2}$. While squeezing at the mechanical frequency has been seen in other modulated schemes [75, 60], we demonstrate possible new schemes for resonant squeezing in slowly-modulated set-ups. Finally, an explicit connection is establised between unequal-frequency correlations of shifted operators and the Fourier components of the periodic spectrum. The cross-correlations (and hence, rotating components of the spectrum) are recovered by choosing the heterodyne local oscillator frequency to be resonant with the modulation of the optomechanical system.

Experimental challenges lie ahead before ground state cooling of levitated nanospheres can be finally achieved. Both feedback and cavity set-ups have to address the issue of recoil heating, which is foreseen as the major roadblock to the quantum regime. Nonspherical geometries more adapted to the cavity shape are being considered [84]; for example, microtoroids and disks, which maximise optomechanical coupling while minimising recoil heating [77]. In addition, magnetic [85] and electrical [86] levitation of nanoparticles have also been proposed. Much interest have also been put into levitating nanodiamonds with NV centers [87, 88] for spin control and novel spin-displacement couplings. Lastly, levitated optomechanics have found applications in studies of nonequilibrium thermodynamics [89, 90]; for example as testbeds for quantum fluctuation theorems [91], which do not require ground state cooling.

Meanwhile, the host of optomechanical set-ups and applications notwithstaning, many experiments still employ traditional continuous, linear detections schemes such as homodyne and heterodyne. In addition, the quantum noise spectra still remains to be the central readout of interest. The hybrid electro-optical trap may or may not be the route to ground state cooling of levitated nanoparticles, but the analysis of the quantum noise spectra of periodically driven optomechanical set-ups motivated by that experiment will hopefully be useful to future optomechanical studies.

A | Wiener-Khinchin Theorem

This appendix proves the Wiener-Khinchin theorem which states that, in the limit of long measurement times, the modulus square of the gated Fourier transform of the measured signal is equal to the Fourier transform of the autocorrelation function.

A.1 Fourier transform convention

Given an operator as a function of time $\hat{u}(t)$, the Fourier transform $\mathcal{F}[\hat{u}(t)]$ is:

$$\hat{u}(\omega) \equiv \int_{-\infty}^{+\infty} \mathrm{d}t\, \mathrm{e}^{\mathrm{i}\omega t}\hat{u}(t) \tag{A.1}$$

There are two conventions [3, 19] for the Fourier transform of the adjoint $\hat{u}^\dagger(t)$.

$$\hat{u}^\dagger(\omega) \equiv \left[\int_{-\infty}^{+\infty} \mathrm{d}t\, \mathrm{e}^{\mathrm{i}\omega t}\hat{u}(t)\right]^\dagger = [\hat{u}(\omega)]^\dagger \tag{A.2}$$

$$\hat{u}^\dagger(\omega) \equiv \int_{-\infty}^{+\infty} \mathrm{d}t\, \mathrm{e}^{\mathrm{i}\omega t}\hat{u}^\dagger(t) = [\hat{u}(-\omega)]^\dagger. \tag{A.3}$$

The latter [19] is followed throughout the work.

The following properties of the Fourier transform will be useful:

$$\mathcal{F}\left[\dot{\hat{u}}(t)\right] = -\mathrm{i}\omega\hat{u}(\omega) \tag{A.4}$$

A.2 Autocorrelation and power spectral density

In experiments and numerics, one has access only to a finite signal, so the *gated* Fourier transform is defined:

$$\hat{\tilde{u}}(\omega) \equiv \frac{1}{\sqrt{T}}\int_0^T \mathrm{d}t\, \mathrm{e}^{\mathrm{i}\omega t}\hat{u}(t), \tag{A.5}$$

where T is the measurement time. The power spectral density (PSD) or power spectrum:

$$S_{uu}(\omega) \equiv \lim_{T\to\infty}\left\langle \hat{\tilde{u}}(\omega)\left[\hat{\tilde{u}}(\omega)\right]^\dagger\right\rangle = \left\langle|\tilde{u}(\omega)|^2\right\rangle \tag{A.6}$$

measures the average noise power within a frequency range. The equality is for the case of complex-valued signals.

Periodic signals have infinite extent, so the PSD cannot be calculated analytically from Eq. A.6. Instead, the Fourier transform of the autocorrelation function is calculated:

$$C_{uv}(\tau, t) \equiv \left\langle \hat{u}^\dagger(\tau + t)\hat{u}(t) \right\rangle = \left\langle \hat{u}^\dagger(\tau)\hat{u}(0) \right\rangle, \tag{A.7}$$

where the equality applies to stationary (time-translation invariant) signals.

A.3 Proof of Wiener-Khinchin theorem

Substituting Eq. A.5 in Eq. A.6:

$$\begin{aligned} S_{uu}(\omega) &= \lim_{T\to\infty} \frac{1}{T} \left\langle \int_0^T \mathrm{d}t_1\, \mathrm{e}^{\mathrm{i}\omega t_1} \hat{u}(t_1) \int_0^T \mathrm{d}t_2\, \mathrm{e}^{-\mathrm{i}\omega t_2} \hat{u}^\dagger(t_2) \right\rangle \\ &= \lim_{T\to\infty} \int_0^T \mathrm{d}t_2 \int_0^T \mathrm{d}t_1\, \mathrm{e}^{\mathrm{i}\omega(t_1 - t_2)} \left\langle \hat{u}(t_1)\hat{u}^\dagger(t_2) \right\rangle \\ &= \int_{-\infty}^{\infty} \mathrm{d}t \int_{-\infty}^{\infty} \mathrm{d}\tau\, \mathrm{e}^{\mathrm{i}\omega\tau} \left\langle \hat{u}(t + \tau)\hat{u}^\dagger(t) \right\rangle, \end{aligned} \tag{A.8}$$

where in the last line, $t_1 = t + \tau$ and $t_2 = t$ and the limit $T \to \infty$ is taken. For stationary signals, the outer integral vanishes and the inner integral simplifies to Eq. A.7.

B | Langevin Equation

This appendix derives the Langevin equations from the independent oscillator model [66] to describe the Brownian motion of a quantum harmonic oscillator due to a thermal bath. Applying rotating wave approximation (RWA) to the model, the input-output relation of the optical cavity is also derived.

B.1 Independent oscillator model

The Langevin equations from the independent oscillator model presented in Chapter 2 are derived. The combined system-bath Hamiltonian are expressed in terms of the ladder operators, and make the canonical transformation $\hat{a}_j \to \mathrm{i}\hat{a}_j$ for consistency with literature:

$$\hat{H} = \hbar\omega_{\mathrm{eff}}\omega\hat{b}^\dagger\hat{b} + \sum_j \omega_j \hat{b}_j^\dagger \hat{b}_j + \mathrm{i}\hbar\omega_j\Big(\hat{b}_j^\dagger\hat{b} - \hat{b}_j\hat{b}^\dagger + \varsigma\hat{b}_j^\dagger\hat{b}^\dagger - \varsigma\hat{b}\hat{b}_j\Big), \tag{B.1}$$

The first two terms are the bare oscillator energy for the system and bath modes, and the effective frequency $\omega_{\mathrm{eff}} = \omega_{\mathrm{M}} + \omega_j$. The last term is the interaction, where $\varsigma = 0$ means we use the RWA. The canonical transformation can be understood as a velocity-coupling model where the particle's position is coupled to the bath momenta: $\frac{\hbar\omega_j}{2}(\hat{x} + \hat{p}_j)^2$. It can be shown that this model is unitarily equivalent to the independent-oscillator model; however, applying RWA does not lead to a unique thermal equilibrium state for the bath [66] and is shown to violate Ehrenfest theorem [92]. One must ensure the bath is weakly coupled to neglect this error. The equation of motion for the bath is:

$$\dot{\hat{b}}_j(t) = -\mathrm{i}\omega_j\hat{b}_j(t) + \omega_j\Big[\hat{b}(t) + \varsigma\hat{b}^\dagger(t)\Big] \tag{B.2}$$

with the solution

$$\hat{b}_j(t) = \hat{b}_j(t_0)\mathrm{e}^{-\mathrm{i}\omega_j(t-t_0)} + \int_{-\infty}^{t} \mathrm{d}t'\,\mathrm{e}^{-\mathrm{i}\omega_j(t-t')}\omega_j\Big[\hat{b}(t') + \varsigma\hat{b}^\dagger(t')\Big], \tag{B.3}$$

which is substituted in the equation of motion for the system:

$$\dot{\hat{b}}(t) = -\mathrm{i}\omega_{\mathrm{eff}}\hat{b}(t) + \sum_j \omega_j \Big[\hat{b}_j(t) - \varsigma\hat{b}_j^\dagger(t)\Big]. \tag{B.4}$$

At this point a continuum of bath modes is assumed: $\sum_j \omega_j^2 \to \int_{-\infty}^{+\infty} \mathrm{d}\omega\, \rho(\omega)\omega^2$, where $\rho(\omega)$ is the density of states. Unlike in [3], the limit of integration is taken to be from $-\infty$ by adopting a rotating frame and by assuming the bath is infinite [93]. Furthermore:

$$\frac{\Gamma_{\mathrm{M}}(\omega)}{2\pi} \equiv \rho(\omega)\omega^2, \tag{B.5}$$

where Γ_{M} is the mechanical damping rate. Eq. B.4 is solved and Eq. B.5 is used to obtain:

$$\begin{aligned}
\dot{\hat{b}}(t) &= -\mathrm{i}\omega_{\mathrm{eff}}\hat{b}(t) - \int_{-\infty}^{\infty} \mathrm{d}\omega \sqrt{\frac{\Gamma_{\mathrm{M}}(\omega)}{2\pi}} \Big[\hat{b}_{t_0}(\omega)\mathrm{e}^{-\mathrm{i}\omega(t-t_0)} - \varsigma\hat{b}_{t_0}^\dagger(\omega)\mathrm{e}^{\mathrm{i}\omega(t-t_0)}\Big] \\
&- \int_{-\infty}^{t} \mathrm{d}t' \int_{-\infty}^{\infty} \mathrm{d}\omega\, \frac{\Gamma_{\mathrm{M}}(\omega)}{2\pi} \Big[\mathrm{e}^{-\mathrm{i}\omega(t-t')} + \varsigma\mathrm{e}^{-\mathrm{i}\omega(t-t')}\Big]\hat{b}(t') \\
&- \int_{-\infty}^{t} \mathrm{d}t' \int_{-\infty}^{\infty} \mathrm{d}\omega\, \frac{\Gamma_{\mathrm{M}}(\omega)}{2\pi} \Big[\varsigma\mathrm{e}^{-\mathrm{i}\omega(t-t')} + \varsigma\mathrm{e}^{\mathrm{i}\omega(t-t')}\Big]\hat{b}^\dagger(t'),
\end{aligned} \tag{B.6}$$

Using the Markov approximation: $\Gamma_{\mathrm{M}}(\omega) = \Gamma_{\mathrm{M}}$, and defining the input noise operator:

$$\hat{b}_{\mathrm{in}}(t) \equiv -\frac{1}{2\pi}\int_{-\infty}^{\infty} \mathrm{d}\omega\, \hat{b}_{t_0}(\omega)\mathrm{e}^{-\mathrm{i}\omega(t-t_0)}, \tag{B.7}$$

where $\hat{b}_{t_0}(\omega)$ is the frequency-dependent initial condition for the bath modes. Furthermore:

$$\int_{-\infty}^{\infty} \mathrm{d}\omega\, \mathrm{e}^{-\mathrm{i}\omega(t-t')} = 2\pi\delta(t-t') \tag{B.8}$$

$$\int_{-\infty}^{t} \mathrm{d}t\, \delta(t-t')\hat{b}(t') = \frac{1}{2}\hat{b}(t), \tag{B.9}$$

where the factor of 1/2 appears due to a change in integration limits. Using Eqs. B.7 to B.9, Eq. B.6 becomes

$$\dot{\hat{b}}(t) = -\mathrm{i}\omega_{\mathrm{eff}}\hat{b}(t) - \frac{\Gamma_{\mathrm{M}}}{2}\Big[\hat{b}(t) + \varsigma\hat{b}^\dagger(t)\Big] + \sqrt{\Gamma_{\mathrm{M}}}\Big[\hat{b}_{\mathrm{in}}(t) - \varsigma\hat{b}_{\mathrm{in}}^\dagger(t)\Big] \tag{B.10}$$

B.1.1 Without rotating wave approximation

Setting $\varsigma = 1$, the Langevin equation without RWA reads:

$$\dot{\hat{b}}(t) = -\mathrm{i}\omega_{\mathrm{eff}}\hat{b}(t) - \frac{\Gamma_{\mathrm{M}}}{2}\sqrt{2}\hat{X}(t) - \mathrm{i}\sqrt{\Gamma_{\mathrm{M}}}\hat{P}_{\mathrm{in}}(t) \tag{B.11}$$

In terms of quadratures,

$$\dot{\hat{X}}(t) = \omega_{\rm eff}\hat{P}(t) - \Gamma_{\rm M}\hat{X}(t) \tag{B.12}$$

$$\dot{\hat{P}}(t) = -\omega_{\rm eff}\hat{X}(t) - \sqrt{2\Gamma_{\rm M}}\hat{P}_{\rm in}(t), \tag{B.13}$$

which leads to the second-order differential equation:

$$\ddot{\hat{X}}(t) = -\omega_{\rm eff}^2\hat{X}(t) - \Gamma_{\rm M}\dot{\hat{X}}(t) - \omega_{\rm eff}\sqrt{2\Gamma_{\rm M}}\hat{P}_{\rm in}(t), \tag{B.14}$$

B.1.2 With rotating wave approximation

Meanwhile, $\varsigma = 0$ yields the Langevin equation with RWA:

$$\dot{\hat{b}}(t) = -{\rm i}\omega_{\rm eff}\hat{b}(t) - \frac{\Gamma_{\rm M}}{2}\hat{b}(t) - \sqrt{\Gamma_{\rm M}}\hat{b}_{\rm in}(t), \tag{B.15}$$

which in terms of quadratures reads:

$$\dot{\hat{X}}(t) = \omega_{\rm eff}\hat{P}(t) - \frac{\Gamma_{\rm M}}{2}\hat{X}(t) - \sqrt{\Gamma_{\rm M}}\hat{X}_{\rm in}(t) \tag{B.16}$$

$$\dot{\hat{P}}(t) = -\omega_{\rm eff}\hat{X}(t) - \frac{\Gamma_{\rm M}}{2}\hat{P}(t) - \sqrt{\Gamma_{\rm M}}\hat{P}_{\rm in}(t), \tag{B.17}$$

Comparing this with Eq. B.13, the main difference that RWA makes is to distribute the damping and fluctuations equally between the quadratures. Solving the simultaneous equations and noting $\omega_{\rm eff}\hat{Y}_{\rm p}(t)$, one will arrive at Eq. B.14 all the same.

B.2 Input-output relations

Equation B.7 is rewritten for the cavity mode:

$$\hat{a}_{\rm in}(t) \equiv \frac{1}{2\pi}\int_{-\infty}^{\infty} {\rm d}\omega\, \hat{a}_{t_0}(\omega){\rm e}^{-{\rm i}\omega(t-t_0)}, \tag{B.18}$$

where $t_0 < t$. If instead $t_1 > t$, the output field can then be derived:

$$\hat{a}_j(t) = \hat{a}_j(t_1){\rm e}^{-{\rm i}\omega_j(t-t_1)} - \int_t^{\infty} \omega_j {\rm e}^{-{\rm i}\omega_j(t-t')}\hat{a}(t') \tag{B.19}$$

Defining the first term as the output field:

$$\hat{a}_{\rm out}(t) = \hat{a}_j(t_1){\rm e}^{-{\rm i}\omega_j(t-t_1)} \tag{B.20}$$

and assuming Markovian approximation, Eq. B.4 becomes

$$\dot{\hat{a}}(t) = -\mathrm{i}\omega_{\mathrm{eff}}\hat{a}(t) - \frac{\kappa}{2}\hat{a}(t) - \sqrt{\kappa}\hat{a}_{\mathrm{in}}(t) \tag{B.21}$$

Eq. B.18 and Eq. B.21 are equated to obtain the input-output relation:

$$\hat{a}_{\mathrm{out}}(t) = \hat{a}_{\mathrm{in}}(t) + \sqrt{\kappa}\hat{a}(t) \tag{B.22}$$

B.2.1 Simulating Markov processes

The Langevin equation is a stochastic differential equation describing a continuous Markov process [94]. Defining the stochastic increment

$$\Xi(\mathrm{d}t\,; x, t) \equiv X(t + \mathrm{d}t) - X(t), \tag{B.23}$$

the conditions of
(i) Markovianity: $X(t + \mathrm{d}t)$ depends only on $X(t)$ and not on any other previous times $X(t' < t)$;
(ii) smoothness: $\Xi(\mathrm{d}t\,; x, t)$ is infinitely differentiable with respect to $\mathrm{d}t\,, x, t$; and
(iii) continuity: $\Xi(\mathrm{d}t\,; x, t) \to 0$ as $\mathrm{d}t \to 0$ for all x and t
(iv) self-consistency: $\Xi(\mathrm{d}t\,; x, t) = \Xi(\alpha\,\mathrm{d}t\,; x, t) + \Xi(\mathrm{d}t - \alpha\,\mathrm{d}t\,; x, t + \alpha\,\mathrm{d}t)$ for $0 < \alpha < 1$
restrict the form of $\Xi(\mathrm{d}t\,; x, t)$ to:

$$\Xi(\mathrm{d}t\,; x, t) = A(X(t), t)\,\mathrm{d}t + D^{1/2}(X(t), t)N(t)(\mathrm{d}t)^{1/2}, \tag{B.24}$$

where $A(X(t), t)$ and $D(X(t), t)$ are the drift and diffusion functions, and $\mathbf{N}(\mu = 0, \sigma = 1) = N(t)$ is the delta-correlated unit Gaussian random variable. The proof of Eq. B.24 can be found in [94]. While Eq. B.24 is useful for simulation, it can also be written in a more familiar form:

$$\frac{\mathrm{d}X(t)}{\mathrm{d}t} = A(X(t), t) + D^{1/2}(X(t), t)\Gamma(t), \tag{B.25}$$

by defining the Gaussian white noise process:

$$\Gamma(t) = \lim_{\mathrm{d}t \to 0} \mathbf{N}(0, (\mathrm{d}t)^{-1}). \tag{B.26}$$

From the combined potential of Eqs. 3.4 and 3.8, the equations of motion can be derived, which are then solve numerically using Runge-Kutta algorithm. A stochastic term is added to the cavity and mechanical mode in the axial direction to simulate the Gaussian noises acquired due to bath couplings. Also included in the y direction are the terms to

account for gravity pulling the nanosphere away from the point of maximum intensity, as well as additional offsets that may be incurred due to a misalignment between the Paul trap and the optical cavity. Combined, these offsets may cause trapping instabilities, as has been observed in numerics. The dynamics is described by nine highly non-linear, coupled Langevin equations:

$$\dot{Y_{\mathrm{a}}} = -\left[\Delta + A\cos^2(kx)\mathcal{F}(y,z)\right]Y_{\mathrm{p}} - \sqrt{\frac{\kappa}{2}}Y_{\mathrm{a}} - \mathcal{E} + \sqrt{\kappa}Y_{\mathrm{a,in}}(t) \tag{B.27}$$

$$\dot{Y_{\mathrm{p}}} = \left[\Delta + A\cos^2(kx)\mathcal{F}(y,z)\right]Y_{\mathrm{a}} - \sqrt{\frac{\kappa}{2}} \tag{B.28}$$

$$\frac{\dot{p}_x}{m} = -\frac{\hbar k A}{m}(Y_{\mathrm{a}}^2 + Y_{\mathrm{p}}^2)\sin(2kx)\mathcal{F}(y,z) - \omega_t^2\hat{x}\sin\omega_d t - \Gamma_{\mathrm{M}}\frac{p_x}{m} + \sqrt{\Gamma}_{\mathrm{M}}x_{\mathrm{in}}(t) \tag{B.29}$$

$$\frac{\dot{p}_y}{m} = 4\hbar A(Y_{\mathrm{a}}^2 + Y_{\mathrm{p}}^2)\cos^2(kx)\mathcal{F}(y,z)y - \omega_t^2(y + y_{\mathrm{off}})\sin\omega_d t - \Gamma_{\mathrm{M}}\frac{p_y}{m} - \mathrm{g} \tag{B.30}$$

$$\frac{\dot{p}_z}{m} = 4\epsilon\hbar A(Y_{\mathrm{a}}^2 + Y_{\mathrm{p}}^2)\cos^2(kx)\mathcal{F}(y,z)z - \omega_t^2 z\sin\omega_d t \tag{B.31}$$

$$\dot{x} = p_x/m \tag{B.32}$$

$$\dot{y} = p_y/m \tag{B.33}$$

$$\dot{z} = p_z/m, \tag{B.34}$$

where the mechanical coordinates x, y, z, p_x, p_y, p_z, and cavity quadratures $Y_{\mathrm{a}}, Y_{\mathrm{p}}$ are real, classical variables. A is the coupling strength (Eq. 3.5), $\mathcal{F}(y,z) = \exp\left[-2(y^2+z^2)/w^2\right]$ is the Gaussian beam envelope, $\mathcal{E}$ is the amplitude of the laser input, y_{off} is the arbitrary offset to account for misalignment between the cavity and the Paul trap, and $\mathrm{g} = 9.8m/s^2$. $Y_{\mathrm{a,in}}(t)$ and $x_{\mathrm{in}}(t)$ are Gaussian, delta-correlated noises. Optical readout modes can also be added.

Note that g or ω_{M} need not be fed into the numerics because they emerge naturally from the nonlinear equations. All the crucial quanties such as A, ω_{T} can be worked out from the experimental parameters given parameters can be found in Table 4.1. This provides a stringent test of the analytical methods, which provide a means to derive the input power and nanosphere charge from the mechanical and secular frequency readings in the experiment.

C | Linear Detection Methods

In this appendix, linear detection methods typically used in optomechanical experiments are discussed. The readout field emanating from the cavity contains the both the intracavity dynamics and the input laser field, as seen in the input-output relation: $\hat{a}_{\rm out} = \hat{a}_{\rm in} + \sqrt{\kappa}\hat{a}$ derived in Appendix B.22. When this field impinges on a square-law photodetector, the photodetected signal will be $\hat{a}^\dagger_{\rm out}\hat{a}_{\rm out}$. Direct photodetection has two disadvantages: 1) the fluctuations in $\hat{a}_{\rm out}$, which contain information about the mechanical motion, will be too weak; and 2) non-trivial cross-correlations between $\hat{a}_{\rm out}$ and $\hat{a}^\dagger_{\rm out}$ will be lost.

Phase-sensitive detection methods, such as homodyne and heterodyne, addresses these problems by beating the desired signal with a strong laser field, called the local oscillator (LO): $a_{\rm LO}(t) = |a_{\rm LO}|e^{i\theta}e^{-i\omega_l t}$, where $|a_{\rm LO}| \gg \hat{a}_{\rm out}$ and θ is the LO phase. In a balanced detection [95], only the components of linear order in $\hat{a}_{\rm out}$ are measured.

C.1 Homodyne

Setting $|a_{\rm LO}| = 1$ and moving into a frame rotating with ω_l leads to the (balanced) homodyne detected signal:

$$i^\theta_{\rm hom}(t) = \hat{a}_{\rm out}e^{-i\theta} + \hat{a}^\dagger_{\rm out}e^{i\theta}. \tag{C.1}$$

The homodyne signals with orthogonal phases can be written in matrix form:

$$\begin{pmatrix} i^\theta_{\rm hom} \\ i^{\theta+\pi/2}_{\rm hom} \end{pmatrix} = \begin{pmatrix} e^{-i\theta} & e^{i\theta} \\ -ie^{-i\theta} & ie^{i\theta} \end{pmatrix} \begin{pmatrix} \hat{a}_{\rm out} \\ \hat{a}^\dagger_{\rm out}. \end{pmatrix} \tag{C.2}$$

Substituting $i^\theta_{\rm hom}(t)$ in Eq. A.6 gives the homodyne spectrum:

$$S_{Y_{\rm hom}}(\omega) = S_{\hat{a}\hat{a}^\dagger}(\omega) + S_{\hat{a}^\dagger\hat{a}}(\omega) + e^{-2i\theta}S_{\hat{a}\hat{a}}(\omega) + e^{2i\theta}S_{\hat{a}^\dagger\hat{a}^\dagger}(\omega) \tag{C.3}$$

While homodyning can have access to the coherent sum of $\hat{a}_{\rm out}$ and $\hat{a}^\dagger_{\rm out}$, and hence to their cross-spectra, important correlations between orthogonal homodyne signals — which contain, for example, complex correlations that show on-resonance squeezing [75] — cannot

be measured as the LO can only have one θ at a time. In the following we will consider more sophisticated detection methods to measure complex correlations.

C.2 Heterodyne

Heterodyne detection is an extension of homodyning by choosing a LO frequency $\Omega \neq \omega_l$. The consequence then is that the heterodyne signal is explicitly time-dependent:

$$i_{\mathrm{het}}(t) = \hat{a}_{\mathrm{out}} \mathrm{e}^{\mathrm{i}(\Omega t - \theta)} + \hat{a}^{\dagger}_{\mathrm{out}} \mathrm{e}^{-\mathrm{i}(\Omega t - \theta)} \tag{C.4}$$

In other words, there is no frame by which the heterodyne signal will be completely stationary. Similarly, the orthogonal heterodyne signals can be written in matrix form:

$$\begin{pmatrix} i^{\theta}_{\mathrm{het}} \\ i^{\theta+\pi/2}_{\mathrm{het}} \end{pmatrix} = \begin{pmatrix} \cos\Omega t & -\sin\Omega t \\ \sin\Omega t & \cos\Omega t \end{pmatrix} \begin{pmatrix} i^{\theta}_{\mathrm{hom}} \\ i^{\theta+\pi/2}_{\mathrm{hom}} \end{pmatrix} \tag{C.5}$$

Clearly, heterodyning is just a simple rotation of homodyne signals in time domain: $i_{\mathrm{het}}(t) = i^{\theta}_{\mathrm{hom}} \cos\Omega t - i^{\theta+\pi/2}_{\mathrm{hom}} \sin\Omega t$. One might think, because $i_{\mathrm{het}}(t)$ contains coherent sum of orthogonal homodyne signals, one will be able to measure their cross-correlation spectrum. Unfortunately, the heterodyne PSD acquires time-dependent correlation terms:

$$S_{Y_{\mathrm{het}}}(\omega, t) = S_{\hat{a}\hat{a}^{\dagger}}(\omega + \Omega) + S_{\hat{a}^{\dagger}\hat{a}}(\omega - \Omega) + S_{\mathrm{corr}}(\omega, t) \tag{C.6}$$

such that $S_{\mathrm{corr}}(\omega, t) = S_{\hat{a}\hat{a}}(\omega)\mathrm{e}^{2\mathrm{i}(\theta+\Omega t)} + S_{\hat{a}^{\dagger}\hat{a}^{\dagger}}(\omega)\mathrm{e}^{-2\mathrm{i}(\theta+\Omega t)}$ gets averaged out due to the continuous nature of the measurement. Hence, the measured heterodyne spectrum

$$S_{Y_{\mathrm{het}}}(\omega) = S_{\hat{a}\hat{a}^{\dagger}}(\omega + \Omega) + S_{\hat{a}^{\dagger}\hat{a}}(\omega - \Omega). \tag{C.7}$$

Equation C.7 does not converge to Eq. C.3 in the same way that Eq. C.4 converges to Eq. C.1 when the limit $\Omega \to 0$ is taken. The terms $S_{\hat{a}\hat{a}}(\omega)$ and $S_{\hat{a}^{\dagger}\hat{a}^{\dagger}}(\omega)$, where ponderomotive squeezing originates, are lost.

In [96], a method called r-heterodyning recovers this loss of correlations can be recovered by convoluting the heterodyne signal with an appropriate filter function, thereby exposing optical squeezing. Details of this method can be found in [96]. Another alternative is to perform a two-heterodyne scheme, called synodyne detection [75].

D | Iterative solution

This appendix presents the iterative solution used to calculate the quantum noise spectra valid for weak modulations. The following has been adapted from a section in the supplementary material of [12].

Slowly-modulated Optomechanics

Considered here is the case where g, ω_{M} are now modulated, but sufficiently slowly $\omega_{\mathrm{d}} \ll \omega_{\mathrm{M}}$ so that linearisation about equilibrium is still possible; a harmonically modulated optomechanical coupling $g(t) = 2\bar{g}\sin\omega_{\mathrm{d}}t$ as well as a modulated mechanical frequency $\omega_{\mathrm{M}}(t) = \overline{\omega}_{\mathrm{M}} + 2\omega_2\cos 2\omega_{\mathrm{d}}t$ are assumed.

Introducing the $g = 2\bar{g}\sin\omega_{\mathrm{d}}t$ and $\omega_{\mathrm{M}} = \overline{\omega}_{\mathrm{M}} + 2\omega_2\cos 2\omega_{\mathrm{d}}t$ modulations, the corresponding Fourier-transformed spectra become:

$$\hat{\mathrm{y}}(\omega) = \bar{g}\eta(\omega)\cdot[\hat{\mathrm{x}}(\omega+\omega_{\mathrm{d}}) - \hat{\mathrm{x}}(\omega-\omega_{\mathrm{d}})] + \sqrt{\kappa}\hat{Y}_{in}(\omega). \tag{D.1}$$

In other words, the optical field does not directly probe the mechanical motion but rather is sensitive to the difference between the displacement spectra at $\omega_{\mathrm{M}} \pm \omega_{\mathrm{d}}$. Conversely, the displacement spectrum is now:

$$\begin{aligned}\hat{\mathrm{x}}(\omega) &= \bar{g}\mu(\omega)\cdot(\hat{\mathrm{y}}(\omega+\omega_{\mathrm{d}}) - \hat{\mathrm{y}}(\omega-\omega_{\mathrm{d}})) + \sqrt{\Gamma_{\mathrm{M}}}\hat{X}_{th}(\omega)\\ &- i\omega_2\mathcal{G}(\omega)\end{aligned} \tag{D.2}$$

with a similar dependence on shifted spectra. However, in this case there is also a correction due to the frequency modulation:

$$\begin{aligned}\mathcal{G}(\omega) &= \chi_{\mathrm{M}}(\omega)\left\{\hat{b}(\omega+2\omega_{\mathrm{d}}) + \hat{b}(\omega-2\omega_{\mathrm{d}})\right\}\\ &- \chi^*_{\mathrm{M}}(-\omega)\left\{\hat{b}^\dagger(\omega+2\omega_{\mathrm{d}}) + \hat{b}^\dagger(\omega-2\omega_{\mathrm{d}})\right\}\end{aligned} \tag{D.3}$$

Unlike the standard case, Eqs. D.1 and D.2 can no longer be solved in closed form. However, they can be solved iteratively, in a perturbative regime where $\omega_2 \ll \omega_\mathrm{d}$ and also for modest values of the coupling $g \ll \kappa, \omega_\mathrm{M}$. The latter condition implies back-action terms are not too large. Although here, a single mode is used for both cooling and read-out, in general, experiments will involve two modes, one for trapping/cooling, while a weaker probe field is used for read-out. The probe mode will have a much lower α so much smaller g. The present case is restricted to values of g which are not too large. In this case, iterative substitution of Eqs. D.1 and D.2 leads to expressions relating $\hat{\mathrm{x}}(\omega)$ to terms shifted by the harmonics of the drive frequency $\hat{\mathrm{x}}(\omega \pm n\omega_\mathrm{d})$ where $(n = 0, 1, 2, ...)$. Truncation is done at $n \leq 2$.

Spectrum of Shifted-Displacement $\hat{\mathrm{X}}^{\pm}(\omega)$

In this section explicit solutions are given for the shifted displacement spectrum:

$$\hat{\mathrm{X}}^{\pm}(\omega) = \hat{\mathrm{x}}(\omega + \omega_\mathrm{d}) - \hat{\mathrm{x}}(\omega - \omega_\mathrm{d}) \tag{D.4}$$

since to obtain the intracavity spectrum, $\hat{\mathrm{y}}(\omega)$ we simply need to interfere this with the cavity-filtered incoming noise term $\hat{Y}_{in}(\omega)$. From this, the cavity output (relevant to for example heterodyne detection) can easily be obtained. Terms in ω_2^2 can also be included, but their effect in the spectra is not significant, so they are not presented here.

Hence, $\hat{\mathrm{X}}^{\pm}(\omega)$ is solved up to *quadratic* order in g, ω_2 (i.e. retaining terms in $g^2, g\omega_2$). To a good approximation, the vector of noises are obtained:

$$\hat{\mathrm{X}}^{\pm}(\omega) \simeq \vec{\mathcal{A}}_{X^{\pm}}(\omega) \cdot \mathcal{Z}_{mod}(\omega), \tag{D.5}$$

noting that the noises vector in this case, $\mathcal{Z}_{mod} = (\hat{b}_{in}(\omega + \omega_\mathrm{d}), \hat{b}^{\dagger}_{in}(\omega + \omega_\mathrm{d}), \hat{b}_{in}(\omega - \omega_\mathrm{d}), \hat{b}^{\dagger}_{in}(\omega - \omega_\mathrm{d}), \hat{a}_{in}(\omega), \hat{a}^{\dagger}_{in}(\omega), \hat{a}_{in}(\omega + 2\omega_\mathrm{d}), \hat{a}^{\dagger}_{in}(\omega + 2\omega_\mathrm{d}), \hat{a}_{in}(\omega - 2\omega_\mathrm{d}), \hat{a}^{\dagger}_{in}(\omega - 2\omega_\mathrm{d}))$ now comprises the shifted vectors. The iterative solution can be extended to include higher harmonics $\omega \pm n\omega_\mathrm{d}$ where $n = 3, 4...$ since for very large ω_2, higher order sidebands become important. However, modest values of $\omega_2 \leq \omega_\mathrm{d}$ are considered so the cut-off is made at $n = 2$; comparison with the full stochastic numerics were used to test convergence.

For convenience a few symbols are defined:

$$\begin{aligned} \mathcal{M}(\omega \pm \omega_\mathrm{d}) &= 1 + \bar{g}^2 \mu(\omega \pm \omega_\mathrm{d}) \eta(\omega \pm 2\omega_\mathrm{d}) \\ \mathcal{N}(\omega) &= 1 + \bar{g}^2 \eta(\omega) \left(\mu(\omega + \omega_\mathrm{d}) + \mu(\omega - \omega_\mathrm{d}) \right). \end{aligned} \tag{D.6}$$

to represent the modifications to the mechanical susceptibilities due to second-order backactions. Furthermore:

$$\begin{aligned}
\mathcal{C}_1(\omega) &= \tilde{\chi}_{\rm M}(\omega+\omega_{\rm d})\tilde{\chi}_{\rm M}(\omega-\omega_{\rm d}) \\
\mathcal{C}_1^{\dagger}(\omega) &= \mathcal{C}_1^{*}(-\omega) \\
\mathcal{C}_{3\pm}(\omega) &= \tilde{\chi}_{\rm M}(\omega\pm\omega_{\rm d})\tilde{\chi}_{\rm M}(\omega\pm 3\omega_{\rm d}) \\
\mathcal{C}_{3\pm}^{\dagger}(\omega) &= \mathcal{C}_{3\pm}^{*}(-\omega),
\end{aligned} \tag{D.7}$$

where $\tilde{\chi}_{\rm M}(\omega) = \frac{\chi_{\rm M}(\omega)}{\mathcal{M}(\omega)}$ and $\tilde{\mu}(\omega) = \frac{\mu(\omega)}{\mathcal{M}(\omega)}$ are the modified susceptibilities.

The vector of coefficients can be conveniently split for $\hat{\rm X}^{\pm}(\omega)$:

$$\vec{\mathcal{A}}_{X^{\pm}}(\omega) = \mathcal{N}^{-1}(\omega)\left[\vec{\mathcal{A}'}_{X^{\pm}}(\omega) - i\omega_2\vec{\mathcal{G}}_{X^{\pm}}(\omega)\right] \tag{D.8}$$

into a vector, $\vec{\mathcal{A}'}_{X^{\pm}}$, corresponding to $\omega_2 = 0$ and another vector, $\vec{\mathcal{G}}_{X^{\pm}}(\omega)$ which comprises the terms dependent on ω_2.

In Chapter 5, the shifted-displacement was expressed as a sum of thermal and backaction terms:

$$\begin{aligned}
\hat{\rm X}^{\pm}(\omega) &= \bar{g}\hat{\rm Y}_{BA}(\omega) - i\omega_2\bar{g}\hat{\rm Y}_{BA}^{(\omega_2)}(\omega) \\
&+ \sqrt{\Gamma_{\rm M}}[\hat{X}_{th}(\omega+\omega_{\rm d}) - \hat{X}_{th}(\omega-\omega_{\rm d}) - i\omega_2\hat{\rm X}_{\omega_2}(\omega)]
\end{aligned}$$

Below the thermal and backaction terms are given explicitly in terms of the noise vectors.

Thermal Noise Coefficients of $\hat{\rm X}^{\pm}(\omega)$

For the thermal components in Eq.D.9:

$\sqrt{\Gamma_{\rm M}}[\hat{X}_{th}(\omega+\omega_{\rm d}) - \hat{X}_{th}(\omega-\omega_{\rm d}) - i\omega_2\hat{\rm X}_{\omega_2}(\omega)] \equiv \mathcal{A}_{b_{in}}(\omega+\omega_{\rm d})\hat{b}_{in}(\omega+\omega_{\rm d}) + \mathcal{A}_{b_{in}}(\omega-\omega_{\rm d})\hat{b}_{in}(\omega-\omega_{\rm d}) + \mathcal{A}_{b_{in}^{\dagger}}(\omega+\omega_{\rm d})\hat{b}_{in}^{\dagger}(\omega+\omega_{\rm d}) + \mathcal{A}_{b_{in}^{\dagger}}(\omega-\omega_{\rm d})\hat{b}_{in}^{\dagger}(\omega-\omega_{\rm d})$

where the corresponding coefficients are given by:

$$\begin{aligned}
\mathcal{A}'_{b_{in}}(\omega\pm\omega_{\rm d}) &= \pm\sqrt{\Gamma_{\rm M}}\tilde{\chi}_{\rm M}(\omega\pm\omega_{\rm d}) \\
\mathcal{A}'_{b_{in}^{\dagger}}(\omega\pm\omega_{\rm d}) &= \pm\sqrt{\Gamma_{\rm M}}\tilde{\chi}_{\rm M}^{*}(-(\omega\pm\omega_{\rm d}))
\end{aligned} \tag{D.9}$$

and:

$$\begin{aligned}\mathcal{G}_{b_{in}}(\omega \pm \omega_{\rm d}) &= \mp\sqrt{\Gamma_{\rm M}}\mathcal{C}_1(\omega) \\ \mathcal{G}_{b_{in}^\dagger}(\omega \pm \omega_{\rm d}) &= \pm\sqrt{\Gamma_{\rm M}}\mathcal{C}_1^\dagger(\omega).\end{aligned} \tag{D.10}$$

All the thermal noise terms scale with $\sqrt{\Gamma_{\rm M}}$; this means that whenever thermal processes are dominant the PSD spectra globally scale with $\Gamma_{\rm M}$: the shape of the functions $S_{\rm xx}(\omega)$ and $S_{\rm yy}(\omega)$ does not depend on $\Gamma_{\rm M}$, but their height and area scale linearly with $\Gamma_{\rm M}$.

Backaction terms in $\hat{\rm X}^{\pm}(\omega)$

The incoming optical noise (here shot noise) drives fluctuations in the displacement which induces backaction noises in $\hat{\rm X}^{\pm}(\omega)$.

The backaction terms in Eq.D.9 are:

$$\bar{g}\hat{\rm Y}_{BA}(\omega) - i\omega_2\bar{g}\hat{\rm Y}_{BA}^{(\omega_2)}(\omega) \equiv \mathcal{A}_{a_{in}}(\omega)\hat{a}_{in}(\omega) + \mathcal{A}_{a_{in}^\dagger}(\omega)\hat{a}_{in}^\dagger(\omega) + \mathcal{A}_{a_{in}}(\omega+2\omega_{\rm d})\hat{a}_{in}(\omega+2\omega_{\rm d}) + \mathcal{A}_{a_{in}^\dagger}(\omega+2\omega_{\rm d})\hat{a}_{in}^\dagger(\omega+2\omega_{\rm d}) + \mathcal{A}_{a_{in}}(\omega-2\omega_{\rm d})\hat{a}_{in}(\omega-2\omega_{\rm d}) + \mathcal{A}_{a_{in}^\dagger}(\omega-2\omega_{\rm d})\hat{a}_{in}^\dagger(\omega-2\omega_{\rm d}).$$

For which the corresponding coefficients:

$$\begin{aligned}\mathcal{A}'_{a_{in}}(\omega) &= -\bar{g}\left[\tilde{\mu}(\omega+\omega_{\rm d}) + \tilde{\mu}(\omega-\omega_{\rm d})\right]\sqrt{\kappa}\chi_o(\omega) \\ \mathcal{A}'_{a_{in}^\dagger}(\omega) &= -\bar{g}\left[\tilde{\mu}(\omega+\omega_{\rm d}) + \tilde{\mu}(\omega-\omega_{\rm d})\right]\sqrt{\kappa}\chi_o^*(-(\omega)),\end{aligned}$$

and:

$$\begin{aligned}\mathcal{G}_{a_{in}}(\omega) &= \bar{g}\mathcal{C}_1\sqrt{\kappa}\chi_o(\omega) \\ \mathcal{G}_{a_{in}^\dagger}(\omega) &= \bar{g}\mathcal{C}_1^\dagger\sqrt{\kappa}\chi_o^*(-\omega).\end{aligned} \tag{D.11}$$

Meanwhile, the backaction noise coefficients at $\omega \pm 2\omega_{\rm d}$ are:

$$\begin{aligned}\mathcal{A}'_{a_{in}}(\omega \pm 2\omega_{\rm d}) &= \bar{g}\tilde{\mu}(\omega \pm \omega_{\rm d})\sqrt{\kappa}\chi_o(\omega \pm 2\omega_{\rm d}) \\ \mathcal{A}'_{a_{in}^\dagger}(\omega \pm 2\omega_{\rm d}) &= \bar{g}\tilde{\mu}(\omega \pm \omega_{\rm d})\sqrt{\kappa}\chi_o^*(-(\omega \pm 2\omega_{\rm d}))\end{aligned}$$

and the corresponding ω_2 corrections are:

$$\begin{aligned}\mathcal{G}_{a_{in}}(\omega \pm 2\omega_{\rm d}) &= -\bar{g}\mathcal{C}_T\sqrt{\kappa}\chi_o(\omega \pm 2\omega_{\rm d}) \\ \mathcal{G}_{a_{in}^\dagger}(\omega \pm 2\omega_{\rm d}) &= -\bar{g}\mathcal{C}_T\sqrt{\kappa}\chi_o^*(-(\omega \pm 2\omega_{\rm d})),\end{aligned} \tag{D.12}$$

with $\mathcal{C}_T = (\mathcal{C}_1 + \mathcal{C}_1^\dagger + \mathcal{C}_{3\pm} + \mathcal{C}_{3\pm}^\dagger)$.

For clarity, the † terms are explicitly presented. They may also be given from $\mathcal{A}'_{a_{in}^\dagger}(\omega) = \mathcal{A}'^*_{a_{in}}(-\omega)$ etc.; however the $i\omega_2$ terms mean that extra care is needed.

Cavity Output Noise Spectra

The PSD of $\hat{\mathrm{X}}^\pm(\omega)$ can be obtained using the coefficients calculated above. Hence $\langle |x(\omega)|^2 \rangle = S_{X^\pm X^\pm}$ is given by:

$$\begin{aligned} S_{X^\pm X^\pm}(\omega) &= \left(|\mathcal{A}_{b_{in}}(\omega+\omega_\mathrm{d})|^2 + |\mathcal{A}_{b_{in}}(\omega-\omega_\mathrm{d})|^2 \right) \bar{n}_b \\ &+ \left(\left|\mathcal{A}_{b_{in}^\dagger}(\omega+\omega_\mathrm{d})\right|^2 + \left|\mathcal{A}_{b_{in}^\dagger}(\omega-\omega_\mathrm{d})\right|^2 \right) (\bar{n}_b + 1) \\ &+ \left|\mathcal{A}_{a_{in}^\dagger}(\omega)\right|^2 \\ &+ \left|\mathcal{A}_{a_{in}^\dagger}(\omega+2\omega_\mathrm{d})\right|^2 + \left|\mathcal{A}_{a_{in}^\dagger}(\omega-2\omega_\mathrm{d})\right|^2 \end{aligned} \tag{D.13}$$

where the noise correlators have been used in Eq. 2.41 and 2.42 and assumed $\bar{n}_a = 0$.

The solutions to $\hat{\mathrm{X}}^\pm(\omega)$ also enable us to easily construct equivalent vectors for the intracavity field and cavity output, including symmetrised spectra if desired, in terms of noises.

For example, the intracavity field $\hat{\mathrm{y}}(\omega) = \frac{1}{\sqrt{2}}(\hat{a}(\omega) + \hat{a}^\dagger(\omega))$ is constructed by scaling the $\hat{\mathrm{X}}^\pm(\omega)$ vector and adding the cavity-filtered incoming noise:

$$\hat{\mathrm{y}}(\omega) = \bar{g}\eta(\omega)\hat{\mathrm{X}}^\pm(\omega) + \sqrt{\kappa}\hat{Y}_{in}(\omega). \tag{D.14}$$

Meanwhile, the cavity output amplitude is given by the standard relation $\hat{a}_{out}(\omega) = \hat{a}_{in}(\omega) - \sqrt{\kappa}\hat{a}$ and the spectrum of its amplitude quadrature $\hat{y}_{out}(\omega) = \frac{1}{\sqrt{2}}(\hat{a}_{out}(\omega) + \hat{a}_{out}^\dagger(\omega))$ is considered:

$$\hat{\mathrm{y}}_{out}(\omega) = \hat{y}_{in}(\omega) - \sqrt{\kappa}\hat{\mathrm{y}}(\omega). \tag{D.15}$$

Hence:

$$\hat{\mathrm{y}}_{out}(\omega) = \hat{I}(\omega) - \sqrt{\kappa}\bar{g}\eta(\omega)\hat{\mathrm{X}}^\pm(\omega) \tag{D.16}$$

where $\hat{I}(\omega) = \hat{y}_{in}(\omega) - \hat{Y}_{in}(\omega)$ and $\hat{y}_{in}(\omega) = \frac{1}{\sqrt{2}}(\hat{a}_{in}(\omega) + \hat{a}_{in}^\dagger(\omega))$. The cavity output PSD is then given in the form:

$$S_{\mathrm{y}_{out}\mathrm{y}_{out}}(\omega) = S_{II}(\omega) + \kappa\bar{g}^2|\eta(\omega)|^2 S_{X^\pm X^\pm}(\omega) + \sqrt{\kappa}\bar{g}S_{IX^\pm}(\omega) \tag{D.17}$$

where $S_{II}(\omega) = \left\langle \hat{I}^\dagger(\omega)\hat{I}(\omega) \right\rangle$ sets the imprecision noise floor and $S_{IX^\pm}(\omega) = 2\mathrm{Re}[\eta(\omega)\hat{I}^\dagger(\omega)\mathrm{X}^\pm(\omega)]$ is the correlation of the displacement spectrum with imprecision noise.

Suppression of the $\omega_{\mathrm{M}} + \omega_{\mathrm{d}}$ Sidebands

The suppression of the peaks at $\omega = \omega_{\mathrm{M}} + \omega_{\mathrm{d}}$ and at $\omega = -(\omega_{\mathrm{M}} + \omega_{\mathrm{d}})$ in $S_{\mathrm{y}_{out}\mathrm{y}_{out}}$ and S_{yy} can now be analysed. The asymmetry in the thermal regime is considered, where the sideband ratio r is invariant. In this case, we can neglect all the optical noise terms can be neglected to simplify (Eq. D.17):

$$\begin{aligned}\frac{S_{\mathrm{y}_{out}\mathrm{y}_{out}}(\omega)}{\kappa\bar{g}^2|\eta(\omega)|^2} \approx &\left(|\mathcal{A}_{b_{in}}(\omega+\omega_{\mathrm{d}})|^2 + |\mathcal{A}_{b_{in}}(\omega-\omega_{\mathrm{d}})|^2\right)\bar{n}_b \\ &+ \left(\left|\mathcal{A}_{b_{in}^\dagger}(\omega+\omega_{\mathrm{d}})\right|^2 + \left|\mathcal{A}_{b_{in}^\dagger}(\omega-\omega_{\mathrm{d}})\right|^2\right)(\bar{n}_b+1)\end{aligned}$$

From this, the sideband heights can be obtained; for example, the height of the $\omega_{\mathrm{M}}+\omega_{\mathrm{d}}$ peak (correct up to a factor of n_b) is

$$|\mathcal{A}_{b_{in}}(\omega-\omega_{\mathrm{d}})|^2 = |\tilde{\chi}_{\mathrm{M}}(\omega-\omega_{\mathrm{d}})|^2\,|1 - i\omega_2\tilde{\chi}_{\mathrm{M}}(\omega+\omega_{\mathrm{d}})|^2\,,$$

the height of the $\omega_{\mathrm{M}} - \omega_{\mathrm{d}}$ peak is

$$|\mathcal{A}_{b_{in}}(\omega+\omega_{\mathrm{d}})|^2 = |\tilde{\chi}_{\mathrm{M}}(\omega+\omega_{\mathrm{d}})|^2\,|1 - i\omega_2\tilde{\chi}_{\mathrm{M}}(\omega-\omega_{\mathrm{d}})|^2\,,$$

and so on.

As in previous sections, note that all the susceptibilities $\tilde{\chi}_{\mathrm{M}}(\omega) = \frac{\chi_{\mathrm{M}}(\omega)}{\mathcal{M}(\omega)}$ are normalised by a factor $\mathcal{M}(\omega)$ arising from second-order backactions. This prevents unphysical spikes from emerging in the spectrum in the limit $\Gamma_{\mathrm{M}} \to 0$. Since the analysis is in the thermal regime, these normalisations may be omitted to get a simple reweighting of the thermal noise coefficients due to ω_2 correction.

$$|\mathcal{A}_{b_{in}}(\omega\pm\omega_{\mathrm{d}})|^2 = |\chi_{\mathrm{M}}(\omega\pm\omega_{\mathrm{d}})|^2\,|1 - i\omega_2\chi_{\mathrm{M}}(\omega\mp\omega_{\mathrm{d}})|^2$$

The weighting factor $|1 - i\omega_2\chi_{\mathrm{M}}(\omega\mp\omega_{\mathrm{d}})|^2$ can be seen as the ω_2 correction to the original height $|\chi_{\mathrm{M}}(\omega\pm\omega_{\mathrm{d}})|^2$.

The susceptibilities $\chi_{\mathrm{M}}(\omega\pm\omega_{\mathrm{d}})$ are sharply peaked at $\omega = \omega_{\mathrm{M}} \mp \omega_{\mathrm{d}}$, hence so is $\mathcal{A}_{b_{in}}(\omega\pm\omega_{\mathrm{d}})$. Evaluating Eq. D.18 at either $\omega = \omega_{\mathrm{M}} + \omega_{\mathrm{d}}$ or $\omega = \omega_{\mathrm{M}} - \omega_{\mathrm{d}}$:

$$|\mathcal{A}_{b_{in}}(\omega_{\mathrm{M}}\pm\omega_{\mathrm{d}})|^2 = \frac{4}{\Gamma_{\mathrm{M}}^2}\,|1 - i\omega_2\chi_{\mathrm{M}}(\omega_{\mathrm{M}}\mp 2\omega_{\mathrm{d}})|^2 \tag{D.18}$$

where

$$\chi_{\rm M}(\omega_{\rm M} \mp 2\omega_{\rm d}) = \frac{1}{\mp i 2\omega_{\rm d} + \frac{\Gamma_{\rm M}}{2}}. \tag{D.19}$$

Supposing that $\frac{\Gamma_{\rm M}}{2} \ll 2\omega_{\rm d}$, the sideband ratio is then

$$r = \frac{|\mathcal{A}_{b_{in}}(\omega_{\rm M} - \omega_{\rm d})|^2}{|\mathcal{A}_{b_{in}}(\omega_{\rm M} + \omega_{\rm d})|^2} \approx \frac{(2\omega_{\rm d} - \omega_2)^2}{(2\omega_{\rm d} + \omega_2)^2}. \tag{D.20}$$

Cavity output spectra in the quantum backaction limit

As seen previously and in the main text, in the limit $\Gamma_{\rm M} \to 0$, the thermal terms in Eq. D.13 are negligible and $\hat{X}^{\pm}(\omega) \simeq \bar{g} Y_T(\omega)$ where the total backaction $Y_T(\omega) = \bar{g}\hat{\rm Y}_{BA}(\omega) - i\omega_2 \bar{g}\hat{\rm Y}_{BA}^{(\omega_2)}(\omega)$. In this case,

$$S_{X^{\pm}X^{\pm}} \approx \left(\left| \mathcal{A}_{a_{in}^{\dagger}}(\omega + 2\omega_{\rm d}) \right|^2 + \left| \mathcal{A}_{a_{in}^{\dagger}}(\omega - 2\omega_{\rm d}) \right|^2 + \left| \mathcal{A}_{a_{in}^{\dagger}}(\omega) \right|^2 \right) \tag{D.21}$$

The resulting backaction-dominated spectrum has the same asymmetry as the thermal spectrum: two peaks with height ratio r, as illustrated in Fig4c of the main text.

However, the cavity output spectrum includes also contributions arising from interference with incoming imprecision noise, thus terms like $\frac{\hat{\rm Y}_{imp}(\omega)}{\sqrt{\kappa}} - \bar{g}\hat{\rm Y}_T(\omega)$ as shown in Eq.7 ofthe main text. Equation D.21 above exposes a new feature of the modulated system: there are backaction terms in dependent on $\omega \pm 2\omega_{\rm d}$ which are uncorrelated with $\hat{\rm Y}_{imp}(\omega)$ so cannot interfere with it. These terms are not present in standard (unmodulated) optomechanics.

In particular, if Eq. D.21 is split into $S_{X^{\pm}X^{\pm}} = S_{Y_{ba}} + S_{Y_{ba2}}$ to differentiate ω and $\pm 2\omega_{\rm d}$ backactions, the cavity output spectrum can be written as:

$$S_{\rm y_{out}y_{out}} = S_{II} + \sqrt{\kappa}\bar{g} S_{IY_{ba}} + \kappa \bar{g}^2 |\eta(\omega)|^2 (S_{Y_{ba}Y_{ba}} + S_{Y_{ba2}Y_{ba2}}) \tag{D.22}$$

While the terms $S_{Y_{ba}Y_{ba}} + S_{Y_{ba2}Y_{ba2}}$ give the same ratio as the thermal spectrum, the imprecision noise S_{II} plus the correlation term $S_{IY_{ba}}$ changes the sideband ratio in the quantum limit.

Future experiments may elucidate further the novel form of the noise spectra of the modulated trap. Comparisons with nonlinear stochastic numerics validate the model in the classical regime, but do not include the non-commuting properties of the quantum noise spectra in Eq.2.41 thus cannot test the model in the quantum limit.

E | Proofs: modulated optomechanics

Some proofs and supplementary details relating to Chapter 6 are given in this appendix.

E.1 Frequency-space noise correlation in terms of Kronecker delta

This section shows the noise correlation used to derive Eq. (6.16) follows from the delta-correlation in time of Eq. (6.4).

$$\begin{aligned}
&\lim_{T\to\infty}\left\langle \mathbf{c}_{\mathrm{in}}(\omega+l\omega_{\mathrm{d}})[\mathbf{c}_{\mathrm{in}}(\omega+l'\omega_{\mathrm{d}})]^{\dagger}\right\rangle \\
&=\lim_{T\to\infty}\left\langle \frac{1}{\sqrt{T}}\int_0^T \mathrm{d}t\mathrm{e}^{\mathrm{i}(\omega+l\omega_{\mathrm{d}})t}\mathbf{c}_{\mathrm{in}}(t)\right. \\
&\left.\times\frac{1}{\sqrt{T}}\int_0^T \mathrm{d}t'\mathrm{e}^{-\mathrm{i}(\omega+l'\omega_{\mathrm{d}})t}[\mathbf{c}_{\mathrm{in}}(t')]^{\dagger}\right\rangle \\
&=\lim_{T\to\infty}\frac{1}{T}\int_0^T \mathrm{d}t\mathrm{e}^{\mathrm{i}(\omega+l\omega_{\mathrm{d}})t}\int_0^T \mathrm{d}t' e^{-\mathrm{i}(\omega+l'\omega_{\mathrm{d}})t'}\left\langle \mathbf{c}_{\mathrm{in}}(t)[\mathbf{c}_{\mathrm{in}}(t')]^{\dagger}\right\rangle \\
&=\lim_{T\to\infty}\frac{1}{T}\int_0^T \mathrm{d}t\mathrm{e}^{\mathrm{i}(\omega+l\omega_{\mathrm{d}})t}\int_0^T \mathrm{d}t' e^{-\mathrm{i}(\omega+l'\omega_{\mathrm{d}})t'}\mathbf{N}\delta(t-t') \\
&=\mathbf{N}\lim_{T\to\infty}\frac{1}{T}\int_0^T \mathrm{d}t\mathrm{e}^{\mathrm{i}(l-l')\omega_{\mathrm{d}}t} \\
&=\mathbf{N}\delta_{ll'}
\end{aligned} \tag{E.1}$$

A generalisation can be obtained for the case of different frequencies that may arise from an external drive during detection. Assuming a frequency difference ω_{diff}, equation (E.1) becomes:

$$\begin{aligned}
&\lim_{T\to\infty}\left\langle \mathbf{c}_{\mathrm{in}}(\omega+l\omega_{\mathrm{d}})[\mathbf{c}_{\mathrm{in}}(\omega+\omega_{\mathrm{diff}}+l'\omega_{\mathrm{d}})]^{\dagger}\right\rangle \\
&=\mathbf{N}\delta_{(l-l')\omega_{\mathrm{d}},\omega_{\mathrm{diff}}}
\end{aligned} \tag{E.2}$$

The Kronecker delta forces ω_{diff} to be an integer multiple of ω_{d}. In the case of Eq. (6.29), we take $\omega_{\text{diff}} = 2\Omega$. For $\omega_{\text{diff}} = 0$, Eq. (E.2) simplifies to Eq. (E.1).

E.2 Analysis of the slowly-modulated system

In this section the general formalism in Sec. 6.1 is applied to analyze in detail the slowly-modulated optomechanical system used to model levitated nanoparticles in a hybrid electro-optical trap.

E.2.1 Time-periodic Langevin equations

Let $\mathbf{c}(t) \equiv \begin{pmatrix} \hat{a}(t) & \hat{a}^\dagger(t) & \hat{b}(t) & \hat{b}^\dagger(t) \end{pmatrix}^{\mathsf{T}}$ and denote the $2l$th element of $\mathbf{c}(t)$ by $\hat{c}_l$ so that $\hat{c}_1 \equiv \hat{a}$ and $\hat{c}_2 \equiv \hat{b}$. The optical and mechanical modes are coupled to their baths at κ and Γ_{M}, respectively so $\gamma = \mathsf{diag}\begin{pmatrix} \kappa & \kappa & \Gamma_{\text{M}} & \Gamma_{\text{M}} \end{pmatrix}$. After symmetrising Eq. (2.36) and using the CCR Eq. (6.2), Eq. (6.1) for the optomechanical system is, explicitly,

$$\begin{pmatrix} \dot{\hat{a}}(t) \\ \dot{\hat{a}}^\dagger(t) \\ \dot{\hat{b}}(t) \\ \dot{\hat{b}}^\dagger(t) \end{pmatrix} = \begin{pmatrix} \mathrm{i}\Delta(t) - \frac{\kappa}{2} & 0 & \mathrm{i}g(t) & \mathrm{i}g(t) \\ 0 & -\mathrm{i}\Delta(t) - \frac{\kappa}{2} & -\mathrm{i}g(t) & -\mathrm{i}g(t) \\ \mathrm{i}g(t) & \mathrm{i}g(t) & -\mathrm{i}\omega_{\text{M}}(t) - \frac{\Gamma_{\text{M}}}{2} & 0 \\ -\mathrm{i}g(t) & -\mathrm{i}g(t) & 0 & \mathrm{i}\omega_{\text{M}}(t) - \frac{\Gamma_{\text{M}}}{2} \end{pmatrix} \begin{pmatrix} \hat{a}(t) \\ \hat{a}^\dagger(t) \\ \hat{b}(t) \\ \hat{b}^\dagger(t) \end{pmatrix} + \begin{pmatrix} \sqrt{\kappa}\hat{a}_{\text{in}}(t) \\ \sqrt{\kappa}\hat{a}^\dagger_{\text{in}}(t) \\ \sqrt{\Gamma}_{\text{M}}\hat{b}_{\text{in}}(t) \\ \sqrt{\Gamma}_{\text{M}}\hat{b}^\dagger_{\text{in}}(t) \end{pmatrix}. \tag{E.3}$$

E.2.2 Matrix equation for the slowly-modulated system

Equation (6.10) is a general equation that computes the system operators from the input noises for any n-mode modulated optomechanical system. To get the equation for a slowly-modulated system we set $\mathbf{c}(\omega + m\omega_{\text{d}}) \equiv \begin{pmatrix} \hat{a}(\omega + m\omega_{\text{d}}) & \hat{a}^\dagger(\omega + m\omega_{\text{d}}) & \hat{b}(\omega + m\omega_{\text{d}}) & \hat{b}^\dagger(\omega + m\omega_{\text{d}}) \end{pmatrix}^{\mathsf{T}}$ and $\mathbf{c}_{\text{in}}(\omega) \equiv \begin{pmatrix} \sqrt{\kappa}\hat{a}_{\text{in}}(\omega) & \sqrt{\kappa}\hat{a}^\dagger_{\text{in}}(\omega) & \sqrt{\Gamma}_{\text{M}}\hat{b}_{\text{in}}(\omega) & \sqrt{\Gamma}_{\text{M}}\hat{b}^\dagger_{\text{in}}(\omega) \end{pmatrix}^{\mathsf{T}}$. Moreover, the matrix elements are derived from the Hamiltonian Eq. (2.36) and the parameters in Eq. (4.1), using Eq. (6.11) and Eq. (6.12):

$$\begin{aligned} \mathrm{X}_n = \mathsf{diag}\,(&\chi_{\text{O}}(\omega + n\omega_{\text{d}})\ \chi^*_{\text{O}}(-\omega - n\omega_{\text{d}}) \\ &\chi_{\text{M}}(\omega + n\omega_{\text{d}})\ \chi^*_{\text{M}}(-\omega - n\omega_{\text{d}})) \end{aligned} \tag{E.4}$$

$$\mathrm{A}_{\pm 1} = \pm\bar{g} \left(\begin{array}{cccc} & & 1 & 1 \\ & & -1 & -1 \\ \hline 1 & 1 & & \\ -1 & -1 & & \end{array}\right) \tag{E.5}$$

$$\mathrm{A}_{\pm 2} = \mathrm{i} \left(\begin{array}{cccc} -\Delta_2 & 0 & & \\ 0 & \Delta_2 & & \\ \hline & & \omega_2 & 0 \\ & & 0 & -\omega_2, \end{array}\right) \tag{E.6}$$

$\mathrm{A}_{|n|>2} = 0$ because modulations greater than $2\omega_\mathrm{d}$ are not considered here. Equation E.4 is substituted in Eq. E.6 in the matrix equation (6.10) and the power spectrum is calculated using Eq. (6.16).

E.3 Components of the periodic spectrum in terms of shifted operators

The components of the periodic spectrum can also be calculated using the shifted operators approach where they have a new interpretation as cross-correlations of operators shifted at different frequencies.

As mentioned Sec. 6.4 C, the assumption of the Floquet formalism is a periodic spectrum $S(\omega, t) = \sum_{m\in\mathrm{Z}} S^{(m)}(\omega)\mathrm{e}^{\mathrm{i}m\omega_\mathrm{d}t}$ with Fourier components [65]:

$$\begin{aligned} S^{(m)}(\omega) &= \sum_l \int_{-\infty}^{+\infty} \frac{\mathrm{d}\omega'}{2\pi} \left\langle \mathbf{c}^{(l)}(\omega + l\omega_\mathrm{d})[\mathbf{c}^{(l-m)}(\omega')]^\dagger \right\rangle \\ &= \sum_l \int_{-\infty}^{+\infty} \frac{\mathrm{d}\omega'}{2\pi} \mathbf{T}_{l0}(\omega + l\omega_\mathrm{d}) \left\langle \mathbf{c}_\mathrm{in}(\omega)[\mathbf{c}_\mathrm{in}(\omega')]^\dagger \right\rangle \\ &\times [\mathbf{T}_{l-m,0}(\omega' + l\omega_\mathrm{d})]^\dagger \\ &= \sum_l \mathbf{T}_{l0}(\omega + l\omega_\mathrm{d})\mathbf{N}[\mathbf{T}_{l-m,0}(\omega + l\omega_\mathrm{d})]^\dagger \end{aligned} \tag{E.7}$$

where Eq. (6.19) have been used and the noise correlation of Eq. (6.5) expressed in frequency space.

Consider the cross-correlation of shifted operators from method (i):

$$\begin{aligned}
&\lim_{T\to\infty}\left\langle \mathbf{c}(\omega)[\mathbf{c}(\omega+m\omega_{\mathrm{d}})]^{\dagger}\right\rangle \\
&=\sum_{l\in\mathrm{Z}}\mathbf{T}_{0l}(\omega)\left\langle \mathbf{c}_{\mathrm{in}}(\omega-l\omega_{\mathrm{d}})[\mathbf{c}_{\mathrm{in}}(\omega-l\omega_{\mathrm{d}})]^{\dagger}\right\rangle[\mathbf{T}_{-m,l}(\omega)]^{\dagger} \\
&=\sum_{l}\mathbf{T}_{0l}(\omega)\mathbf{N}[\mathbf{T}_{-m,l}(\omega)]^{\dagger}=S^{(m)}(\omega)
\end{aligned} \tag{E.8}$$

where in the last line the translation property of $\mathbf{T}$ has been invoked. The Fourier components of the Fourier spectrum can therefore be calculated using method (i).

Bibliography

[1] J. D. Teufel, T. Donner, Dale Li, J. W. Harlow, M. S. Allman, K. Cicak, A. J. Sirois, J. D. Whittaker, K. W. Lehnert, and R. W. Simmonds. Sideband cooling of micromechanical motion to the quantum ground state. *Nature*, 475:359, 2011.

[2] Jasper Chan, T. P. Mayer Alegre, Amir H. Safavi-Naeini, Jeff T. Hill, Alex Krause, Simon Gröblacher, Markus Aspelmeyer, and Oskar Painter. Laser cooling of a nanomechanical oscillator into its quantum ground state. *Nature*, 478:89, 2011.

[3] W.P. Bowen and G.J. Milburn. *Quantum Optomechanics*. CRC Press, 2015.

[4] Amir H Safavi-Naeini and Oskar Painter. Proposal for an optomechanical traveling wave phonon-photon translator. *New Journal of Physics*, 13(1):013017, 2011.

[5] Thierry Botter, Daniel W. C. Brooks, Nathan Brahms, Sydney Schreppler, and Dan M. Stamper-Kurn. Linear amplifier model for optomechanical systems. *Phys. Rev. A*, 85(1):013812, 2012.

[6] Piergiacomo Zucconi Galli Fonseca. *Levitated optomechanics in a hybrid electro-optical trap*. PhD thesis, University College London, 2017.

[7] Yong-Chun Liu, Yun-Feng Xiao, Xingsheng Luan, and Chee Wei Wong. Dynamic dissipative cooling of a mechanical resonator in strong coupling optomechanics. *Phys. Rev. Lett.*, 110(15):153606, 2013.

[8] March Raymond E. An introduction to quadrupole ion trap mass spectrometry. *Journal of Mass Spectrometry*, 32(4):351, 1997.

[9] E B Aranas, P Z G Fonseca, P F Barker, and T S Monteiro. Thermometry of levitated nanoparticles in a hybrid electro-optical trap. *Journal of Optics*, 19(3):034003, 2017.

[10] P. Z. G. Fonseca, E. B. Aranas, J. Millen, T. S. Monteiro, and P. F. Barker. Nonlinear dynamics and strong cavity cooling of levitated nanoparticles. *Phys. Rev. Lett.*, 117(17):173602, 2016.

[11] Nikolai Kiesel, Florian Blaser, Uroš Delić, David Grass, Rainer Kaltenbaek, and Markus Aspelmeyer. Cavity cooling of an optically levitated submicron particle. *Proceedings of the National Academy of Sciences*, 110(35):14180, 2013.

[12] E B Aranas, P Z G Fonseca, P F Barker, and T S Monteiro. Split-sideband spectroscopy in slowly modulated optomechanics. *New Journal of Physics*, 18(11):113021, 2016.

[13] E. B. Aranas, M. Javed Akram, Daniel Malz, and T. S. Monteiro. Quantum noise spectra for periodically driven cavity optomechanics. *Phys. Rev. A*, 96(6):063836, 2017.

[14] M. J. Akram, E. B. Aranas, N. P. Bullier, J. E. Lang, and T. S. Monteiro. Stochastic Langevin propagation for classical and quantum optomechanics. *ArXiv e-prints*, January 2018.

[15] B. P. Abbott et al. Observation of gravitational waves from a binary black hole merger. *Phys. Rev. Lett.*, 116(6):061102, 2016.

[16] B. P. Abbott et al. Gw170817: Observation of gravitational waves from a binary neutron star inspiral. *Phys. Rev. Lett.*, 119(16):161101, 2017.

[17] A. Antognini et al. Proton structure from the measurement of 2s-2p transition frequencies of muonic hydrogen. *Science*, 339(6118):417, 2013.

[18] V. B. Braginskiĭ and A. B. Manukin. Ponderomotive Effects of Electromagnetic Radiation. *Soviet Journal of Experimental and Theoretical Physics*, 25:653, 1967.

[19] Markus Aspelmeyer, Tobias J. Kippenberg, and Florian Marquardt. Cavity optomechanics. *Rev. Mod. Phys.*, 86(4):1391, 2014.

[20] L. Neumeier, T. E. Northup, and D. E. Chang. Reaching the optomechanical strong coupling regime with a single atom in a cavity. *ArXiv e-prints*, 2017.

[21] L. Magrini, R. A. Norte, R. Riedinger, I. Marinković, D. Grass, U. Delić, S. Gröblacher, S. Hong, and M. Aspelmeyer. Nanophotonic near-field levitated optomechanics. *ArXiv e-prints*, 2018.

[22] A. A. Clerk, M. H. Devoret, S. M. Girvin, Florian Marquardt, and R. J. Schoelkopf. Introduction to quantum noise, measurement, and amplification. *Rev. Mod. Phys.*, 82(2):1155, 2010.

[23] T. P. Purdy, R. W. Peterson, and C. A. Regal. Observation of radiation pressure shot noise on a macroscopic object. *Science*, 339(6121):801, 2013.

[24] Sydney Schreppler, Nicolas Spethmann, Nathan Brahms, Thierry Botter, Maryrose Barrios, and Dan M. Stamper-Kurn. Optically measuring force near the standard quantum limit. *Science*, 344(6191):1486, 2014.

[25] A. D. O'Connell, M. Hofheinz, M. Ansmann, Radoslaw C. Bialczak, M. Lenander, Erik Lucero, M. Neeley, D. Sank, H. Wang, M. Weides, J. Wenner, John M. Martinis, and A. N. Cleland. Quantum ground state and single-phonon control of a mechanical resonator. *Nature*, 464:697, 2010.

[26] Florian Marquardt, Joe P. Chen, A. A. Clerk, and S. M. Girvin. Quantum theory of cavity-assisted sideband cooling of mechanical motion. *Phys. Rev. Lett.*, 99(9):093902, 2007.

[27] I. Wilson-Rae, N. Nooshi, W. Zwerger, and T. J. Kippenberg. Theory of ground state cooling of a mechanical oscillator using dynamical backaction. *Phys. Rev. Lett.*, 99(9):093901, 2007.

[28] Amir H. Safavi-Naeini, Jasper Chan, Jeff T. Hill, Thiago P. Mayer Alegre, Alex Krause, and Oskar Painter. Observation of quantum motion of a nanomechanical resonator. *Phys. Rev. Lett.*, 108(3):033602, 2012.

[29] A. J. Weinstein, C. U. Lei, E. E. Wollman, J. Suh, A. Metelmann, A. A. Clerk, and K. C. Schwab. Observation and interpretation of motional sideband asymmetry in a quantum electromechanical device. *Phys. Rev. X*, 4(4):041003, 2014.

[30] Sungkun Hong, Ralf Riedinger, Igor Marinković, Andreas Wallucks, Sebastian G. Hofer, Richard A. Norte, Markus Aspelmeyer, and Simon Gröblacher. Hanbury brown and twiss interferometry of single phonons from an optomechanical resonator. *Science*, 2017.

[31] E. E. Wollman, C. U. Lei, A. J. Weinstein, J. Suh, A. Kronwald, F. Marquardt, A. A. Clerk, and K. C. Schwab. Quantum squeezing of motion in a mechanical resonator. *Science*, 349(6251):952, 2015.

[32] J. M. Pirkkalainen, E. Damskägg, M. Brandt, F. Massel, and M. A. Sillanpää. Squeezing of quantum noise of motion in a micromechanical resonator. *Phys. Rev. Lett.*, 115(24):243601, 2015.

[33] F. Lecocq, J. B. Clark, R. W. Simmonds, J. Aumentado, and J. D. Teufel. Quantum nondemolition measurement of a nonclassical state of a massive object. *Phys. Rev. X*, 5(4):041037, 2015.

[34] M. J. Woolley and A. A. Clerk. Two-mode squeezed states in cavity optomechanics via engineering of a single reservoir. *Phys. Rev. A*, 89(6):063805, 2014.

[35] C. F. Ockeloen-Korppi, E. Damskägg, J. M. Pirkkalainen, M. Asjad, A. A. Clerk, F. Massel, M. J. Woolley, and M. A. Sillanpää. Stabilized entanglement of massive mechanical oscillators. *Nature*, 556(7702):478, 2018.

[36] Stefan Weis, Rémi Rivière, Samuel Deléglise, Emanuel Gavartin, Olivier Arcizet, Albert Schliesser, and Tobias J. Kippenberg. Optomechanically induced transparency. *Science*, 330(6010):1520, 2011.

[37] T. P. Purdy, P.-L. Yu, R. W. Peterson, N. S. Kampel, and C. A. Regal. Strong optomechanical squeezing of light. *Phys. Rev. X*, 3(3):031012, 2013.

[38] Amir H Safavi-Naeini, Jasper Chan, Jeff T Hill, Simon Gröblacher, Haixing Miao, Yanbei Chen, Markus Aspelmeyer, and Oskar Painter. Laser noise in cavity-optomechanical cooling and thermometry. *New Journal of Physics*, 15(3):035007, 2013.

[39] A. Pontin, C. Biancofiore, E. Serra, A. Borrielli, F. S. Cataliotti, F. Marino, G. A. Prodi, M. Bonaldi, F. Marin, and D. Vitali. Frequency-noise cancellation in optomechanical systems for ponderomotive squeezing. *Phys. Rev. A*, 89(3):033810, 2014.

[40] T. A. Palomaki, J. D. Teufel, R. W. Simmonds, and K. W. Lehnert. Entangling mechanical motion with microwave fields. *Science*, 342(6159):710, 2013.

[41] Wojciech Hubert Zurek. Decoherence, einselection, and the quantum origins of the classical. *Rev. Mod. Phys.*, 75(3):715, 2003.

[42] Gian Carlo Ghirardi, Philip Pearle, and Alberto Rimini. Markov processes in hilbert space and continuous spontaneous localization of systems of identical particles. *Phys. Rev. A*, 42(1):78, 1990.

[43] Oriol Romero-Isart, Mathieu L Juan, Romain Quidant, and J Ignacio Cirac. Toward quantum superposition of living organisms. *New Journal of Physics*, 12(3):033015, 2010.

[44] P. F. Barker and M. N. Shneider. Cavity cooling of an optically trapped nanoparticle. *Phys. Rev. A*, 81(2):023826, 2010.

[45] D. E. Chang, C. A. Regal, S. B. Papp, D. J. Wilson, J. Ye, O. Painter, H. J. Kimble, and P. Zoller. Cavity opto-mechanics using an optically levitated nanosphere. *Proceedings of the National Academy of Sciences*, 107(3):1005, 2010.

[46] A. Ashkin and J. M. Dziedzic. Optical levitation in high vacuum. *Applied Physics Letters*, 28(6):333, 1976.

[47] Oriol Romero-Isart. Quantum superposition of massive objects and collapse models. *Phys. Rev. A*, 84(5):052121, 2011.

[48] Kurt Jacobs, Lin Tian, and Justin Finn. Engineering superposition states and tailored probes for nanoresonators via open-loop control. *Phys. Rev. Lett.*, 102(5):057208, 2009.

[49] A. Vinante, M. Bahrami, A. Bassi, O. Usenko, G. Wijts, and T. H. Oosterkamp. Upper bounds on spontaneous wave-function collapse models using millikelvin-cooled nanocantilevers. *Phys. Rev. Lett.*, 116(9):090402, 2016.

[50] Andrew A. Geraci, Scott B. Papp, and John Kitching. Short-range force detection using optically cooled levitated microspheres. *Phys. Rev. Lett.*, 105(10):101101, 2010.

[51] Zhang-Qi Yin, Andrew A. Geraci, and Tongcang Li. Optomechanics of levitated nanoparticles. *International Journal of Modern Physics B*, 27(26):1330018, 2013.

[52] Tongcang Li, Simon Kheifets, and Mark G. Raizen. Millikelvin cooling of an optically trapped microsphere in vacuum. *Nature Physics*, 7:527, 2011.

[53] Jan Gieseler, Bradley Deutsch, Romain Quidant, and Lukas Novotny. Subkelvin parametric feedback cooling of a laser-trapped nanoparticle. *Phys. Rev. Lett.*, 109(10):103603, 2012.

[54] Vijay Jain, Jan Gieseler, Clemens Moritz, Christoph Dellago, Romain Quidant, and Lukas Novotny. Direct measurement of photon recoil from a levitated nanoparticle. *Phys. Rev. Lett.*, 116(24):243601, 2016.

[55] Jamie Vovrosh, Muddassar Rashid, David Hempston, James Bateman, Mauro Paternostro, and Hendrik Ulbricht. Parametric feedback cooling of levitated optomechanics in a parabolic mirror trap. *J. Opt. Soc. Am. B*, 34(7):1421, 2017.

[56] Peter Asenbaum, Stefan Kuhn, Stefan Nimmrichter, Ugur Sezer, and Markus Arndt. Cavity cooling of free silicon nanoparticles in high vacuum. *Nature Communications*, 4:2743, 2013.

[57] G. A. T. Pender, P. F. Barker, Florian Marquardt, J. Millen, and T. S. Monteiro. Optomechanical cooling of levitated spheres with doubly resonant fields. *Phys. Rev. A*, 85(2):021802, 2012.

[58] J. Millen, P. Z. G. Fonseca, T. Mavrogordatos, T. S. Monteiro, and P. F. Barker. Cavity cooling a single charged levitated nanosphere. *Phys. Rev. Lett.*, 114(12):123602, 2015.

[59] Carlton M. Caves, Kip S. Thorne, Ronald W. P. Drever, Vernon D. Sandberg, and Mark Zimmermann. On the measurement of a weak classical force coupled to a quantum-mechanical oscillator. i. numbers of principle. *Rev. Mod. Phys.*, 52(2):341, 1980.

[60] A A Clerk, F Marquardt, and K Jacobs. Back-action evasion and squeezing of a mechanical resonator using a cavity detector. *New Journal of Physics*, 10(9):095010, 2008.

[61] A Szorkovszky, A A Clerk, A C Doherty, and W P Bowen. Detuned mechanical parametric amplification as a quantum non-demolition measurement. *New Journal of Physics*, 16(4):043023, 2014.

[62] B A Levitan, A Metelmann, and A A Clerk. Optomechanics with two-phonon driving. *New Journal of Physics*, 18(9):093014, 2016.

[63] A. Mari and J. Eisert. Gently modulating optomechanical systems. *Phys. Rev. Lett.*, 103(21):213603, 2009.

[64] Andreas Kronwald, Florian Marquardt, and Aashish A. Clerk. Arbitrarily large steady-state bosonic squeezing via dissipation. *Phys. Rev. A*, 88(6):063833, 2013.

[65] Daniel Malz and Andreas Nunnenkamp. Floquet approach to bichromatically driven cavity-optomechanical systems. *Phys. Rev. A*, 94(2):023803, 2016.

[66] G. W. Ford, J. T. Lewis, and R. F. O'Connell. Quantum langevin equation. *Phys. Rev. A*, 37(11):4419, 1988.

[67] C. Doolin, B. D. Hauer, P. H. Kim, A. J. R. MacDonald, H. Ramp, and J. P. Davis. Nonlinear optomechanics in the stationary regime. *Phys. Rev. A*, 89(5):053838, 2014.

[68] Jan Gieseler, Lukas Novotny, and Romain Quidant. Thermal nonlinearities in a nanomechanical oscillator. *Nature Physics*, 9:806, 2013.

[69] G A Brawley, M R Vanner, P E Larsen, S Schmid, A Boisen, and W P Bowen. Nonlinear optomechanical measurement of mechanical motion. *Nature Communications*, 7:10988, 2016.

[70] A. Nunnenkamp, K. Børkje, and S. M. Girvin. Single-photon optomechanics. *Phys. Rev. Lett.*, 107(6):063602, 2011.

[71] M. Tsang. Testing quantum mechanics: a statistical approach. *Quantum Measurements and Quantum Metrology*, 1:84, 2013.

[72] Kjetil Børkje. Heterodyne photodetection measurements on cavity optomechanical systems: Interpretation of sideband asymmetry and limits to a classical explanation. *Phys. Rev. A*, 94(4):043816, 2016.

[73] K. Gottfried and T.M. Yan. *Quantum Mechanics: Fundamentals*. Graduate Texts in Contemporary Physics. Springer New York, 2013.

[74] Vladimir B. Braginsky, Yuri I. Vorontsov, and Kip S. Thorne. Quantum nondemolition measurements. *Science*, 209(4456):547–557, 1980.

[75] L. F. Buchmann, S. Schreppler, J. Kohler, N. Spethmann, and D. M. Stamper-Kurn. Complex squeezing and force measurement beyond the standard quantum limit. *Phys. Rev. Lett.*, 117(3):030801, 2016.

[76] D.F. Walls and G.J. Milburn. *Quantum Optics*. Springer study edition. Springer-Verlag, 1994.

[77] Anika C. Pflanzer, Oriol Romero-Isart, and J. Ignacio Cirac. Master-equation approach to optomechanics with arbitrary dielectrics. *Phys. Rev. A*, 86(1):013802, 2012.

[78] A. Nunnenkamp, K. Børkje, J. G. E. Harris, and S. M. Girvin. Cooling and squeezing via quadratic optomechanical coupling. *Phys. Rev. A*, 82(2):021806, 2010.

[79] Eric D. Black. An introduction to pound-drever-hall laser frequency stabilization. *American Journal of Physics*, 69(1):79, 2001.

[80] Paul S. Epstein. On the resistance experienced by spheres in their motion through gases. *Phys. Rev.*, 23(6):710, 1924.

[81] A. Serafini. *Quantum Continuous Variables: A Primer of Theoretical Methods*. Taylor & Francis Group, 2017.

[82] Daniel Malz and Andreas Nunnenkamp. Optomechanical dual-beam backaction-evading measurement beyond the rotating-wave approximation. *Phys. Rev. A*, 94(5):053820, 2016.

[83] G. A. Peterson, F. Lecocq, K. Cicak, R. W. Simmonds, J. Aumentado, and J. D. Teufel. Demonstration of efficient nonreciprocity in a microwave optomechanical circuit. *Phys. Rev. X*, 7(3):031001, 2017.

[84] Thai M. Hoang, Yue Ma, Jonghoon Ahn, Jaehoon Bang, F. Robicheaux, Zhang-Qi Yin, and Tongcang Li. Torsional optomechanics of a levitated nonspherical nanoparticle. *Phys. Rev. Lett.*, 117(12):123604, 2016.

[85] O. Romero-Isart, L. Clemente, C. Navau, A. Sanchez, and J. I. Cirac. Quantum magnetomechanics with levitating superconducting microspheres. *Phys. Rev. Lett.*, 109(14):147205, 2012.

[86] D. Goldwater and J. Millen. Levitated electromechanics: all-electrical cooling of levitated nano- and micro-particles. *ArXiv e-prints*, 2018.

[87] T Delord, L Nicolas, L Schwab, and G Hétet. Electron spin resonance from nv centers in diamonds levitating in an ion trap. *New Journal of Physics*, 19(3):033031, 2017.

[88] Klemens Hammerer and Markus Aspelmeyer. Diamonds take off. *Nature Photonics*, 9:633, 2015.

[89] Loïc Rondin, Jan Gieseler, Francesco Ricci, Romain Quidant, Christoph Dellago, and Lukas Novotny. Direct measurement of kramers turnover with a levitated nanoparticle. *Nature Nanotechnology*, 12:1130, 2017.

[90] J. Millen, T. Deesuwan, P. Barker, and J. Anders. Nanoscale temperature measurements using non-equilibrium brownian dynamics of a levitated nanosphere. *Nature Nanotechnology*, 9:425, 2014.

[91] Thai M. Hoang, Rui Pan, Jonghoon Ahn, Jaehoon Bang, H. T. Quan, and Tongcang Li. Experimental test of the differential fluctuation theorem and a generalized jarzynski equality for arbitrary initial states. *Phys. Rev. Lett.*, 120(8):080602, 2018.

[92] G.W. Ford and R.F. O'Connell. Inconsistency of the rotating wave approximation with the ehrenfest theorem. *Physics Letters A*, 215(5):245, 1996.

[93] C. W. Gardiner and M. J. Collett. Input and output in damped quantum systems: Quantum stochastic differential equations and the master equation. *Phys. Rev. A*, 31(6):3761, 1985.

[94] Daniel T. Gillespie. The mathematics of brownian motion and johnson noise. *American Journal of Physics*, 64(3):225, 1996.

[95] H. R. Carleton and W. T. Maloney. A balanced optical heterodyne detector. *Appl. Opt.*, 7(6):1241, 1968.

[96] A. Pontin, J. E. Lang, A. Chowdhury, P. Vezio, F. Marino, B. Morana, E. Serra, F. Marin, and T. S. Monteiro. Imaging correlations in heterodyne spectra for quantum displacement sensing. *Phys. Rev. Lett.*, 120(2):020503, 2018.

[97] M. Bhattacharya, A. N. Vamivakas, and P. Barker. Levitated optomechanics: introduction. *J. Opt. Soc. Am. B*, 34(6):LO1, 2017.

[98] Levi P. Neukirch and A. Nick Vamivakas. Nano-optomechanics with optically levitated nanoparticles. *Contemporary Physics*, 56(1):48, 2015.

[99] L. Childress, M. P. Schmidt, A. D. Kashkanova, C. D. Brown, G. I. Harris, A. Aiello, F. Marquardt, and J. G. E. Harris. Cavity optomechanics in a levitated helium drop. *Phys. Rev. A*, 96(6):063842, 2017.

[100] Levi P. Neukirch and A. Nick Vamivakas. Nano-optomechanics with optically levitated nanoparticles. *Contemporary Physics*, 56(1):48, 2015.

[101] E. Verhagen, S. Deléglise, S. Weis, A. Schliesser, and T. J. Kippenberg. Quantum-coherent coupling of a mechanical oscillator to an optical cavity mode. *Nature*, 482:63, 2012.

[102] R. W. Peterson, T. P. Purdy, N. S. Kampel, R. W. Andrews, P.L. Yu, K. W. Lehnert, and C. A. Regal. Laser cooling of a micromechanical membrane to the quantum backaction limit. *Phys. Rev. Lett.*, 116(6):063601, 2016.

[103] Joerg Bochmann, Amit Vainsencher, David D. Awschalom, and Andrew N. Cleland. Nanomechanical coupling between microwave and optical photons. *Nature Physics*, 9:712, 2013.

[104] R. W. Andrews, R. W. Peterson, T. P. Purdy, K. Cicak, R. W. Simmonds, C. A. Regal, and K. W. Lehnert. Bidirectional and efficient conversion between microwave and optical light. *Nature Physics*, 10:321, 2014.

[105] Farid Ya. Khalili, Haixing Miao, Huan Yang, Amir H. Safavi-Naeini, Oskar Painter, and Yanbei Chen. Quantum back-action in measurements of zero-point mechanical oscillations. *Phys. Rev. A*, 86(3):033840, 2012.

[106] J. D. Thompson, B. M. Zwickl, A. M. Jayich, Florian Marquardt, S. M. Girvin, and J. G. E. Harris. Strong dispersive coupling of a high-finesse cavity to a micromechanical membrane. *Nature*, 452:72, 2008.

[107] K. Børkje, A. Nunnenkamp, J. D. Teufel, and S. M. Girvin. Signatures of nonlinear cavity optomechanics in the weak coupling regime. *Phys. Rev. Lett.*, 111(5):053603, 2013.

[108] Andreas Kronwald and Florian Marquardt. Optomechanically induced transparency in the nonlinear quantum regime. *Phys. Rev. Lett.*, 111(13):133601, 2013.

[109] D. Lee, M. Underwood, D. Mason, A. B. Shkarin, S. W. Hoch, and J. G. E. Harris. Multimode optomechanical dynamics in a cavity with avoided crossings. *Nature Communications*, 6:6232, 2015.

[110] T S Monteiro, J Millen, G A T Pender, Florian Marquardt, D Chang, and P F Barker. Dynamics of levitated nanospheres: towards the strong coupling regime. *New Journal of Physics*, 15(1):015001, 2013.

[111] Brandon V. Rodenburg, Levi Neukirch, Monica Rizzo, Nick Vamivakas, and Mishkat Bhattacharya. Theory of feedback cooling of an optically trapped nanoparticle into the quantum ground state. In *Frontiers in Optics 2015*, page FTu5A.7. Optical Society of America, 2015.

[112] O. Romero-Isart, A. C. Pflanzer, F. Blaser, R. Kaltenbaek, N. Kiesel, M. Aspelmeyer, and J. I. Cirac. Large quantum superpositions and interference of massive nanometer-sized objects. *Phys. Rev. Lett.*, 107(2):020405, 2011.

[113] James Bateman, Stefan Nimmrichter, Klaus Hornberger, and Hendrik Ulbricht. Near-field interferometry of a free-falling nanoparticle from a point-like source. *Nature Communications*, 5:4788, 2014.

[114] Daniel Goldwater, Mauro Paternostro, and P. F. Barker. Testing wave-function-collapse models using parametric heating of a trapped nanosphere. *Phys. Rev. A*, 94(1):010104, 2016.

[115] M. Bahrami, M. Paternostro, A. Bassi, and H. Ulbricht. Proposal for a noninterferometric test of collapse models in optomechanical systems. *Phys. Rev. Lett.*, 112(21):210404, 2014.

[116] Gambhir Ranjit, Mark Cunningham, Kirsten Casey, and Andrew A. Geraci. Zeptonewton force sensing with nanospheres in an optical lattice. *Phys. Rev. A*, 93(5):053801, 2016.

[117] Gambhir Ranjit, Cris Montoya, and Andrew A. Geraci. Cold atoms as a coolant for levitated optomechanical systems. *Phys. Rev. A*, 91(1):013416, 2015.

[118] J. M. Dobrindt, I. Wilson-Rae, and T. J. Kippenberg. Parametric normal-mode splitting in cavity optomechanics. *Phys. Rev. Lett.*, 101(26):263602, 2008.

[119] T. P. Purdy, K. E. Grutter, K. Srinivasan, and J. M. Taylor. Quantum correlations from a room-temperature optomechanical cavity. *Science*, 356(6344):1265, 2017.

[120] Arthur Ashkin. Optical trapping and manipulation of neutral particles using lasers. *Proceedings of the National Academy of Sciences*, 94(10):4853, 1997.

[121] S. A. Beresnev, V. G. Chernyak, and G. A. Fomyagin. Motion of a spherical particle in a rarefied gas. part 2. drag and thermal polarization. *Journal of Fluid Mechanics*, 219:405, 1990.